Astronomy Reports, Vol. 45, No. 9, 2001, pp. 667–675. Translated from Astronomicheskiĭ Zhurnal, Vol. 78, No. 9, 2001, pp. 771–779.

Measurement of the Integrated Faraday Rotations of BL Lac Objects

A. B. Pushkarev

Astro-Space Center, Lebedev Physical Institute, Leninskiĭ pr. 53, 117924 Russia

Received November 10, 2000

Abstract—We present the results of multi-frequency polarization VLA observations of radio sources from the complete sample of northern, radio-bright BL Lac objects compiled by H. Kühr and G. Schmidt. These were used to determine the integrated rotation measures of 18 sources, 15 of which had never been measured previously, which hindered analysis of the intrinsic polarization properties of objects in the complete sample. These measurements make it possible to correct the observed orientations of the linear polarizations of these sources for the effect of Faraday rotation. The most probable origin for Faraday rotation in these objects is the Galactic interstellar medium. The results presented complete measurements of the integrated rotation measures for all 34 sources in the complete sample of BL Lac objects. *© 2001 MAIK "Nauka/Interperiodica".*

1. INTRODUCTION

BL Lac objects are an extreme class of active galactic nuclei characterized by a number of peculiar properties: weak or absent optical line emission, rapid and strong variability in all parts of the electromagnetic spectrum, a high degree of linear polarization, and compact radio and pointlike optical structure.

In 1990, Kühr and Schmidt [1] compiled a complete sample of radio-bright BL Lac objects in the Northern sky, consisting of 34 sources satisfying the following selection criteria: (1) total flux at 5 GHz $I \geq 1$ Jy at the epoch at which the sample was compiled, (2) two-point spectral index between 11 and 6 cm $\alpha_{11\text{–}6} \geq -0.5$ ($S \sim \nu^{+\alpha}$), and (3) equivalent width of emission lines $W \leq 5$ Å. The sample included sources brighter than 20^m in the optical with declinations $\delta > 20°$ located outside the Galactic plane ($|b| > 10°$). We are currently analyzing multi-frequency, polarization-sensitive Very Long Baseline Interferometry (VLBI) data for all sources in the sample.

VLBI polarization observations can yield radio images of compact sources such as BL Lac objects with angular resolution of the order of a millisecond of arc. Such observations contain information about all four Stokes parameters, i.e., both the total intensity and the linear and circular polarization of the radiation. The emission of BL Lac objects is characteristically linearly polarized, since it is synchrotron radiation. Thus, polarization-sensitive observations carry information not only about the energetics and kinematics of the sources observed, but also about the degree of order and orientation of the magnetic fields in their jets, which are very important when analyzing the physical conditions in these objects.

There are a number of factors that can complicate deduction of the direction of the magnetic field in a particular region in a source. Three properties of the region must be known: first, the orientation of the electric vector of its linear polarization, second its optical depth, and finally, its rotation measure.

The first two properties flow directly from any multi-frequency polarization observations, and yield the orientation of the magnetic field in the radiating region relative to the observed polarization electric vector. When a sufficiently high degree of polarization is detected at even one frequency, this indicates that the radiating plasma must be optically thin, since optically thick radiation cannot be more than ≈10–15% polarized [2]. If the plasma is optically thin, the magnetic and electric fields are mutually perpendicular, whereas the two fields are parallel if the plasma is optically thick. The core of the source is usually considered to be optically thick, while the jet becomes increasingly transparent—optically thin—with distance from the core. This is demonstrated by the presence of highly polarized jet components [3] (isolated regions of brightening of the total intensity), whose degree of polarization can reach 60–70%—the limit for optically thin synchrotron radiation [2]. The high degrees of polarization that are sometimes observed in the VLBI jets of BL Lac objects testify that the magnetic fields are well ordered in these regions. As a rule, the jet emission has a steep spectrum, confirming that we are dealing here with an optically thin plasma.

Faraday rotation of the plane of linear polarization occurs when polarized radiation passes through a region containing thermal plasma and a magnetic field with a non-zero component along the line of sight. The rotation measure can only be derived from multi-frequency polarization observations. However, wide-band polarimetry (1.4, 5, 8, 15, 22 GHz, for example) is not suited to this purpose. As is discussed in [5], the best suited observations are those made with the NRAO VLA at 1.3–1.7 GHz. When planning observations designed to

1063-7729/01/4509-0667$21.00

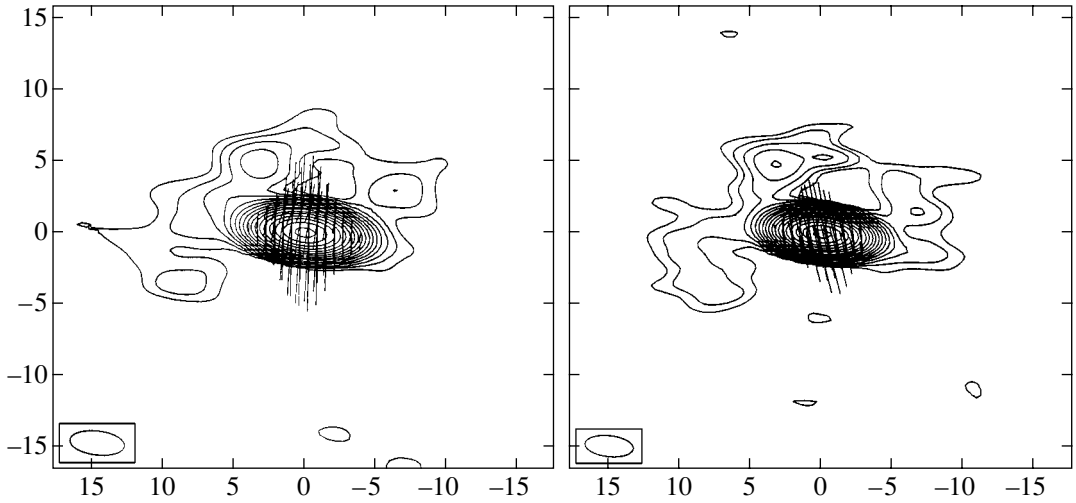

Fig. 1. Total-intensity maps of 0119 + 115 at 1.41 GHz (left) and 1.63 GHz (right) with linear polarization vectors superposed. The peak flux densities are 892 and 891 mJy, respectively, and the lowest contours are 0.35% left and 0.25% right of the peaks, respectively. The horizontal and vertical scales are in arcseconds.

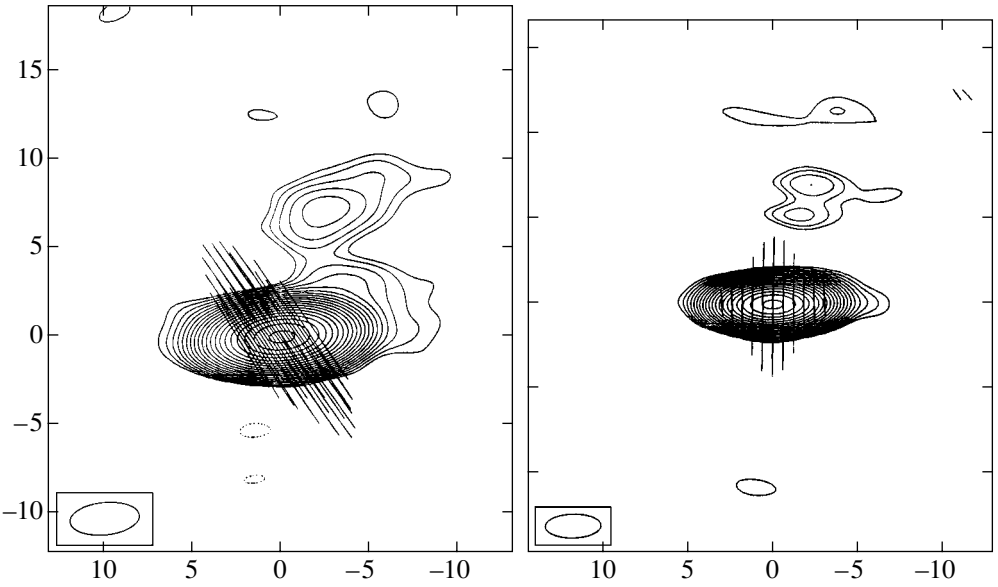

Fig. 2. Total-intensity maps of 0235 + 164 at 1.41 GHz (left) and 1.66 GHz (right) with linear polarization vectors superposed. The peak flux densities are 833 and 1032 mJy, respectively, and the lowest contours are 0.125% of the peaks. The horizontal and vertical scales are in arcseconds.

derive the rotation measures of compact extragalactic sources, several requirements on the frequency interval to be used should be taken into consideration. First, there should be a large enough spacing between the corresponding wavelengths (more precisely, the squares of the wavelengths) to detect the rotation of the plane of linear polarization. Second, these wavelengths should be long enough not to give rise to large ambiguities when calculating the rotation measures. Finally, the wavelengths should not be very different from each other, since otherwise, there is the possibility of detecting radiation from electrons with qualitatively different energies—i.e., from physical different regions in the source—at the different wavelengths.

2. OBSERVATIONS

We obtained VLA observations (C or D configuration) during four sessions: January 19, 1996 (Session 1), January 29, 1996 (Session 2), February 7, 1996 (Session 3), and June 26, 1998 (Session 4). The 1998 observations were conducted in order to refine our initial

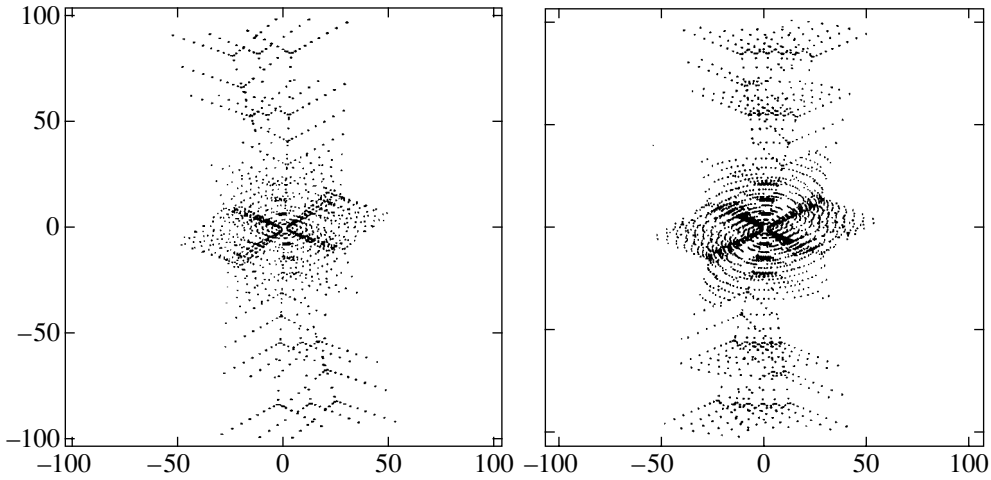

Fig. 3. Coverage of the u–v plane for the VLA observations of 0119 + 115 (left, three scans) and 0235 + 164 (right, six scans). The horizontal and vertical scales are thousands of wavelengths.

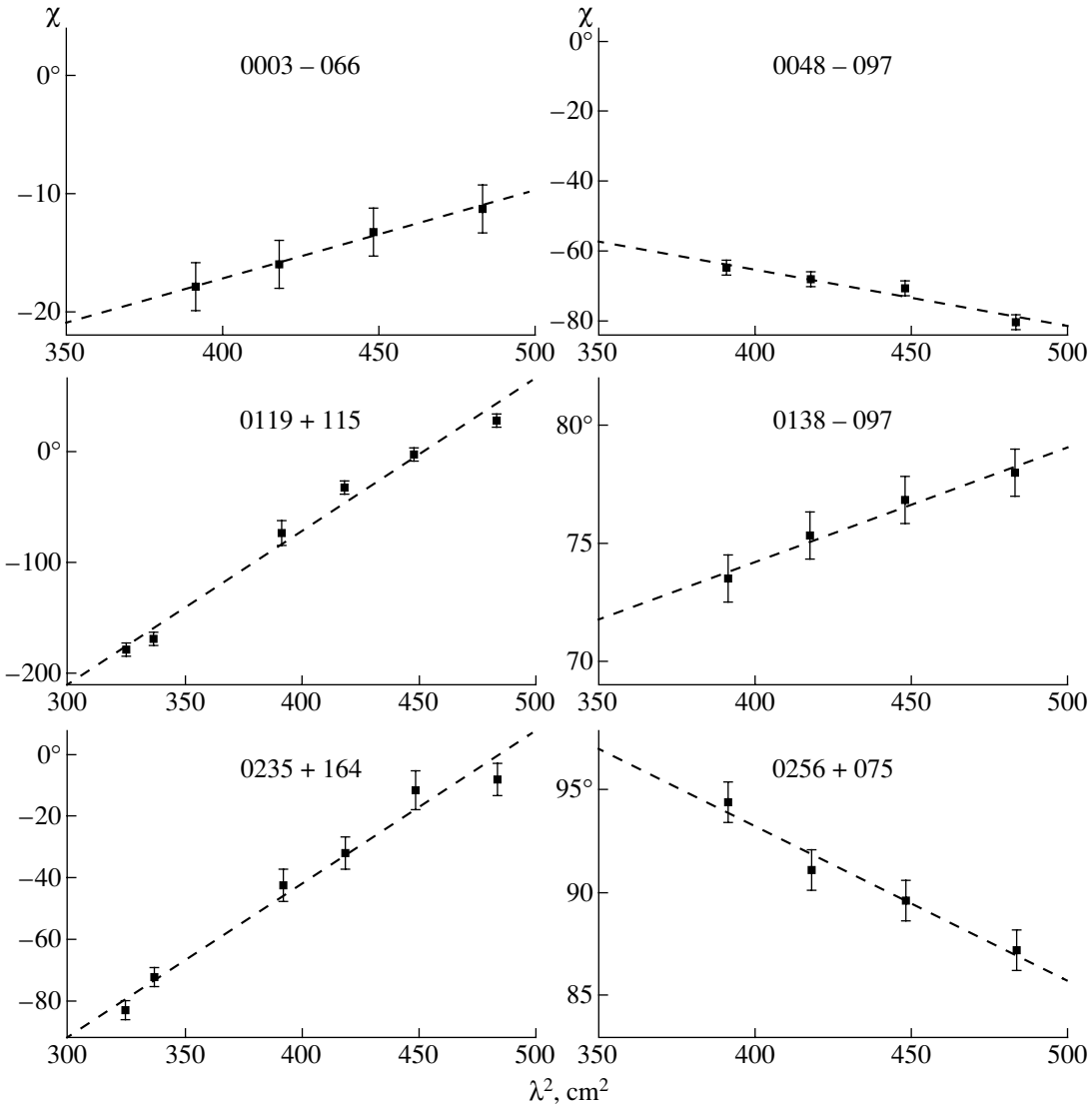

Fig. 4. Dependence of the polarization position angle χ (in degrees) on the square of the wavelength (in cm^2) for the sample sources.

determination of the rotation measure for 0119 + 115, since the 1996 data for this source were of comparatively low quality, leading to a large uncertainty in its rotation measure. All the observations were carried out at six frequencies (1664.9, 1635.1, 1515.9, 1467.7, 1417.5, and 1365.1 MHz), with bandwidths of 50 MHz for the observations at 1664.9 and 1635.1 MHz and 25 MHz for the remaining frequencies. The data were calibrated in the AIPS (Astronomical Image Processing System, NRAO) package. The primary flux calibrators were 3C 286 (Sessions 2 and 3) and 3C 48 (Sessions 1 and 4). The polarization position angles were calibrated using 3C 286 (Sessions 2 and 3) and 3C 138 (Sessions 1 and 4), for which we assumed the polarization position angles $\chi = +33°$ and $\chi = -9°$, respectively, at all frequencies, since these sources do not have significant rotation measures [8]. The instrumental polarizations were determined using sources with observations spanning a large interval (>90°) in parallactic angle—2150 + 173 (Session 1), 0917 + 624 (Session 2), 1147 + 245 (Session 3), and 0235 + 495 (Session 4). The unpolarized sources 2352 + 495 (Session 1, $m_L \le 1\%$), 1323 + 321 (Sessions 2 and 3, $m_L \le 0.6\%$), and 0134 + 329 (Session 4, $m_L \le 0.8\%$) were used to check the results of the solutions for the instrumental polarizations.

3. RESULTS

Structure on VLA (kiloparsec) scales was detected in the two sources 0119 + 115 and 0235 + 164. Figures 1 and 2 show images of the distributions of total intensity for these sources, with linear-polarization vectors superposed. The remaining sources were unresolved at the sensitivity level reached in our observations, and so

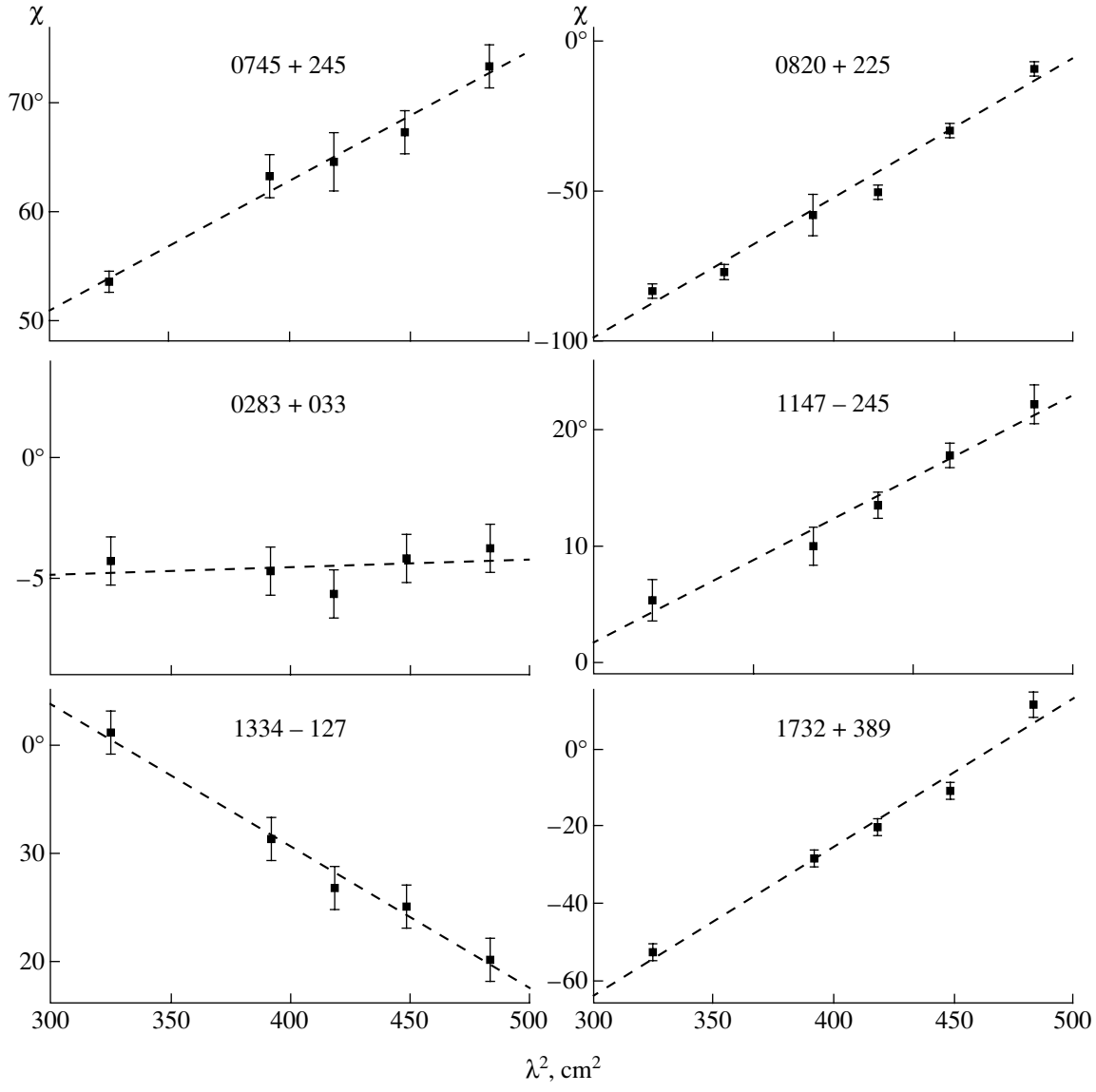

Fig. 4. (Contd.)

their images are not shown. The images in Figs. 1 and 2 were made at different frequencies, and variations in the polarization angles are clearly visible. The orientation of these vectors corresponds to that of the polarization electric vectors, and their length is proportional to the degree of polarization. The sizes and shapes of the antenna beams are indicated in the lower left corner of each image. Figure 3 shows the u–v coverages for 0119 + 115 and 0235 + 164 for our observations, which are typical for VLA "snap-shot" observations of sources at these declinations.

Figure 4 presents the dependence of the polarization position angle χ on the square of the wavelength for the 18 sources. In all cases, these plots show a linear dependence on λ^2. The desired rotation measure is the slope of the line

$$\chi(\lambda^2) = \chi_0 + \mathrm{RM}\lambda^2, \quad \mathrm{RM} = 0.81\int N_e B\cos\theta\, dl, \quad (1)$$

where N_e is the density of thermal electrons (cm^{-3}), B the magnetic field (μG), θ the angle between the direction of propagation of the radiation and the magnetic-field direction, and dl an element of path length from the source to the observer (pc). This expression for the rotation measure is valid for quasi-longitudinal propagation (so that the angle θ is small) and a weak magnetic field [4].

As a rule, errors in χ are several degrees, and are presented at the 2σ level; we had several observations for each source at each frequency, enabling us to estimate

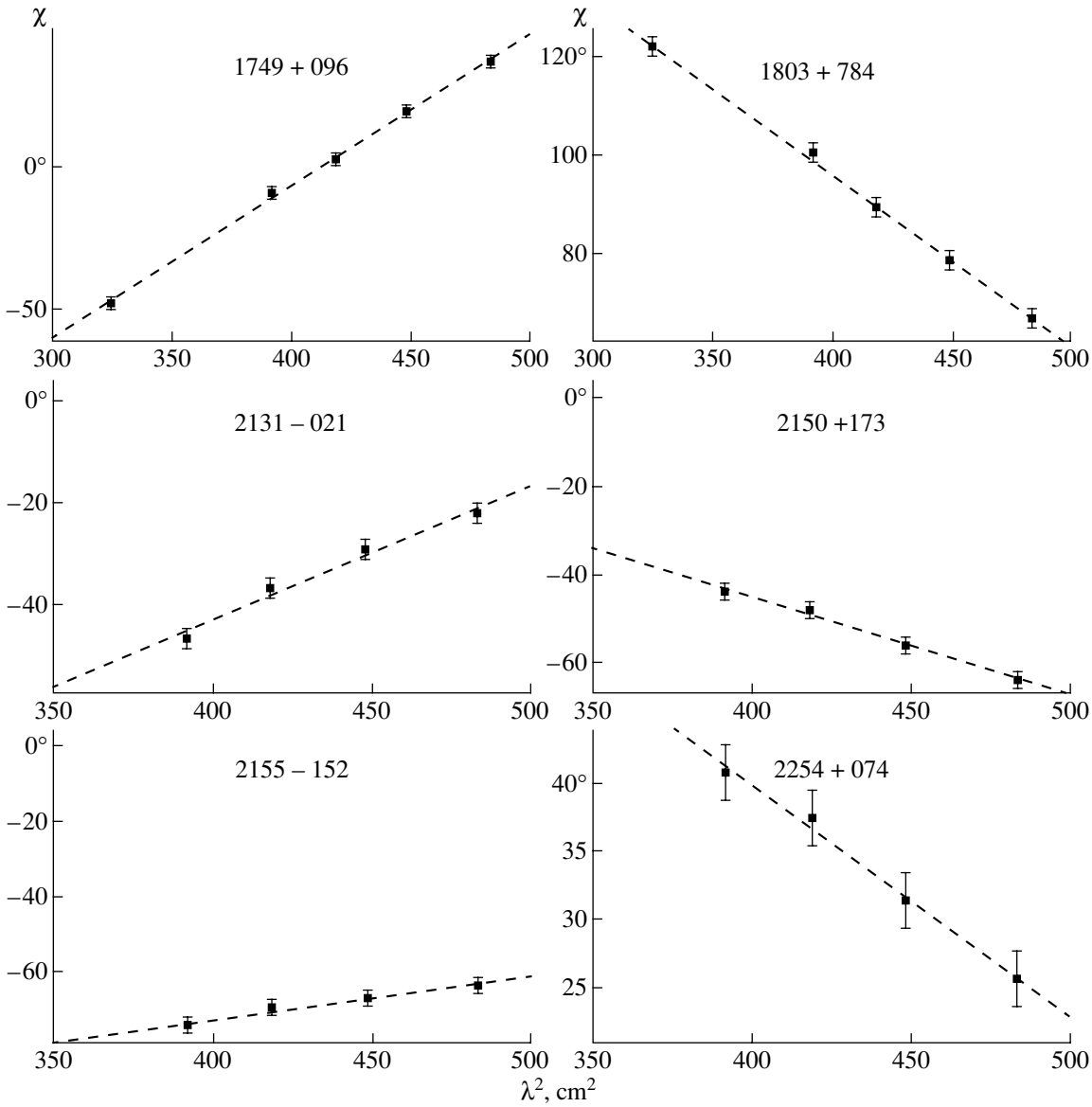

Fig. 4. (Contd.)

Integrated rotation measures for all sources in the complete sample of BL Lac objects

Source	Rudnick and Jones [5]	Rusk [6]	Wrobel [7]	Our observations	z	Scale, Kpc/arcsec[1]
0003 – 066				13 ± 2	0.347	2.9
0048 – 097				−28 ± 7	–	–
0119 + 115				240 ± 18	0.570	3.7
0138 – 097				9 ± 2	0.440	3.3
0235 + 164	57 ± 20	57 ± 21		85 ± 9	0.940	4.2
0256 + 075				−13 ± 2	0.893	4.2
0454 + 844		5 ± 6			0.112	1.3
0716 + 714		−30 ± 3			–	–
0735 + 178	9 ± 13	9 ± 12			0.424	3.3
0745 + 241				21 ± 2	0.410	3.2
0814 + 425		19 ± 9			0.245	2.4
0820 + 225				81 ± 10	0.951	4.2
0823 + 033				1 ± 2	0.506	3.6
0828 + 493		−6 ± 5			0.548	3.7
0851 + 202	31 ± 2	31 ± 3			0.306	2.8
0954 + 658		−15 ± 4			0.368	3.1
1147 + 245				19 ± 2	–	–
1308 + 326	−4 ± 4	−4 ± 4			0.996	4.3
1334 – 127				−23 ± 3	0.539	3.7
1418 + 546	17 ± 7				0.151	1.7
1538 + 149		17 ± 2			0.605	3.8
1652 + 398		42[2]			0.033	0.5
1732 + 389				67 ± 8	0.970	4.2
1749 + 096	105 ± 22			94 ± 6	0.322	3.0
1749 + 701	33 ± 22	16 ± 5	8 ± 13		0.770	4.0
1803 + 784		−70 ± 5	−61 ± 4	−61 ± 2	0.680	3.9
1807 + 698	20 ± 46	5 ± 5	14 ± 4		0.051	0.7
1823 + 568		34 ± 5	36 ± 4		0.664	3.9
2007 + 777		−20 ± 3			0.342	3.1
2131 – 021				46 ± 7	1.285	4.3
2150 + 173				−39 ± 4	–	–
2155 – 152				19 ± 4	0.672	3.9
2200 + 420	−205 ± 6				0.068	0.8
2254 + 074				−30 ± 3	0.190	2.0

[1] For a uniformly expanding Universe ($q_0 = 0.5$) with $H_0 = 100$ km s^{-1} Mpc^{-1}.
[2] Author does not present errors for this measurement.

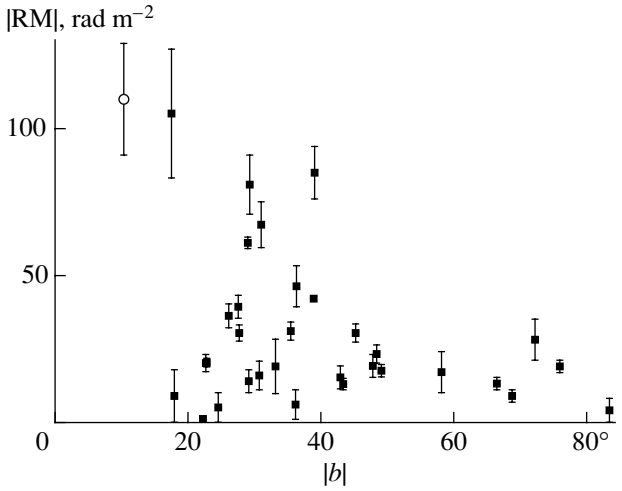

Fig. 5. Dependence of the absolute value of the rotation measure on the absolute value of the Galactic latitude. For sources with several RM measurements, we chose the RM value obtained at the latest epoch. The new value for the Galactic contribution to the rotation measure of BL Lac found by Reynolds *et al.* [9] is shown by the hollow circle.

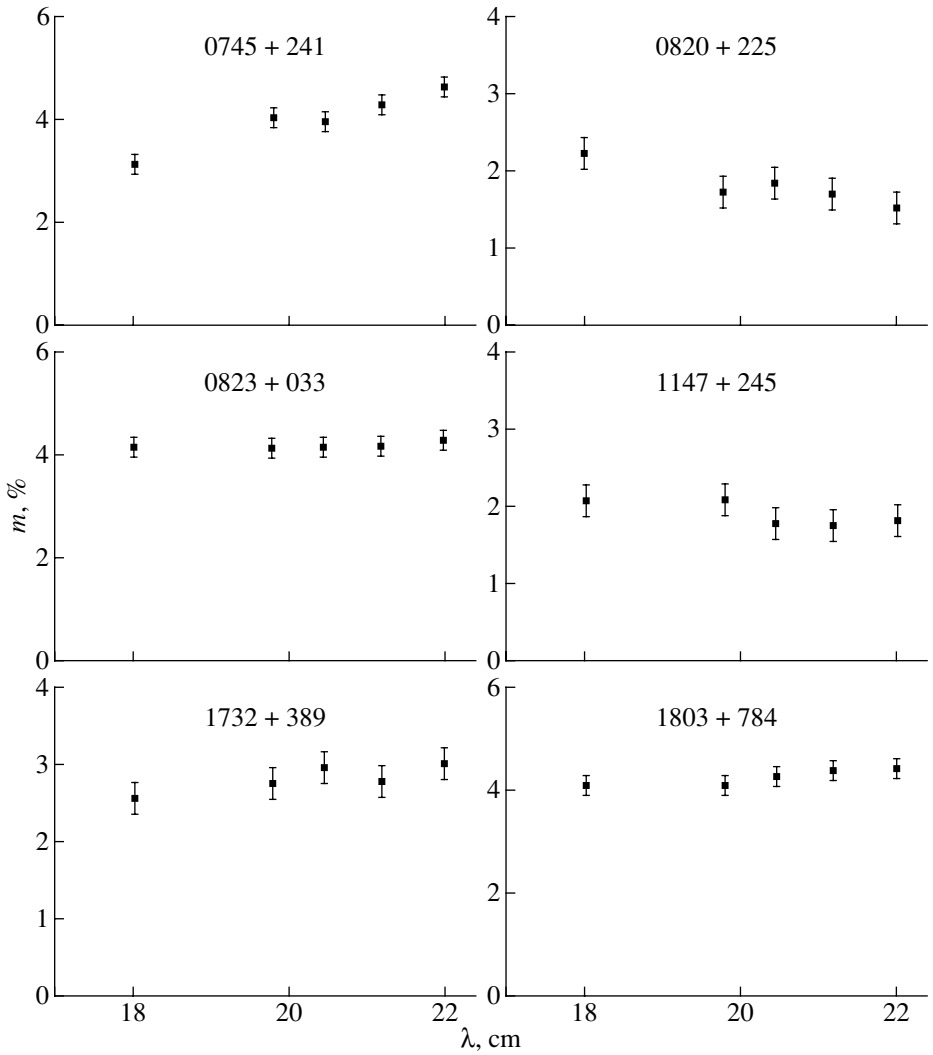

Fig. 6. Dependence of the degree of polarization on wavelength using six sources as examples. There is no evidence for depolarization.

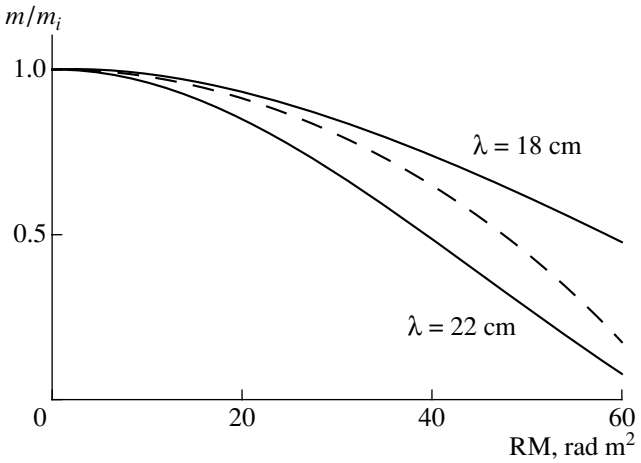

Fig. 7. Dependence of the relative degree of polarization m/m_i at various wavelengths on the rotation measure, where m_i is the intrinsic degree of polarization in the absence of internal Faraday rotation and m is the degree of polarization expected for a plane-layer model [9] in which a substantial fraction of the rotation measure is internal to the source. The dashed curve shows the theoretical dependence of the ratio of the degrees of polarization $m_{\lambda_1}/m_{\lambda_2}$ for wavelengths λλ 18 and 22 cm predicted by this model.

the errors in χ by comparing these independent measurements. We determined linear least-squares fits to the observed χ dependences. Note that the polarization angle is determined with accuracy to within $\pm n\pi$ (n = 0, 1, 2, …), which can lead to ambiguity in the rotation measure RM, since we are dealing with observations at a discrete set of frequencies. The square of the minimum difference between neighboring wavelengths will determine this ambiguity, which in our case is ±1190 rad/m^2. Nevertheless, the presence of six observing frequencies and their proximity to one another enables us to determine the rotation measures with certainty.

The integrated rotation measures for the 18 sources from the complete sample of Kühr and Schmidt [1] are presented in the table, together with results for the remaining 16 sample sources obtained in earlier observations [5–7]. These values are primarily in the interval |RM| = 0–100 rad/m^2, which coincide with the Galactic rotation measures derived from observations of 555 radio sources [8]. Only two objects have |RM| > 200 rad/m^2. It is probable that the Faraday rotation we have detected occurs primarily when the radiation passes through the interstellar medium of the Galaxy. Further evidence for this is provided by the distribution of the |RM| values for all the sample sources relative to the absolute value of the Galactic latitude, where we can see a tendency for |RM| to decrease with increase $|b|$ (Fig. 5).

Figure 5 does not show the two highest values of |RM|, for the sources 0119 + 115 and 2200 + 420 (BL Lac). Results obtained by Reynolds *et al.* [9] (personal communication) based on multi-frequency VLBI observations show that the Galactic contribution to the observed integrated rotation measure of BL Lac is –110 ± 19 rad/m^2, indicated in Fig. 5 by the hollow circle. We can see that this new value agrees well with the general tendency shown by the remaining rotation measures of the sample sources. It is not ruled out that the rotation measure for 0119 + 115 also includes an appreciable contribution from regions near the source.

In addition, we do not detect evidence for depolarization (Fig. 6); the degree of polarization remains essentially constant with frequency. Depolarization arises when the thermal plasma associated with the RM is mixed in with the source [10]. In this case, the polarizations from the far and near regions of the source add incoherently, and the resulting observed polarized decreases as the Faraday depth increases. This is shown for a plane-layer model [10] in Fig. 7, which presents theoretical depolarization curves for various wavelengths when an appreciable fraction of the rotation measure is internal to the source.

Moreover, another piece of evidence supporting a Galactic origin for most of the observed rotation measures is that the RM values apparently do not vary with time, as indicated by the values in the table for sources for which there are observations at more than one epoch; note that all the results in the table were obtained using the same observing and reduction techniques. In addition, as was shown in [11], the rotation measures remain constant over periods of decades, in spite of the presence of appreciable variations of the source polarizations.

4. CONCLUSIONS

We have derived integrated rotation measures for 18 sources, completing such RM measurements for all 34 BL Lac objects in the complete sample, using simultaneous VLA polarization observations at six frequencies below 2 GHz. The mean value of |RM| for the entire sample is ~40 rad/m^2. The observed RM values are associated with thermal plasma external to the source, and probably arise when the radiation passes through the interstellar medium of the Galaxy.

However, such overall modest values for the integrated rotation measures do not rule out the presence of substantially higher RMs and sharp RM gradients in the inner regions of the compact VLBI jets of a few of these sources. Our multi-frequency VLBI polarization observations, currently being analyzed, will enable us to identify such cases of non-uniform Faraday rotation in the immediate vicinities of the compact radio sources.

ACKNOWLEDGMENTS

The author thanks Denise Gabuzda for assistance with the primary calibration of the data, and also for valuable comments and constructive discussions of this work.

REFERENCES

1. H. Kühr and G. D. Schmidt, Astron. J. **99**, 1 (1990).
2. A. G. Pacholczyk, *Radio Astrophysics* (Freeman, San Francisco, 1970).
3. D. C. Gabuzda, A. B. Pushkarev, and T. V. Cawthorne, Mon. Not. R. Astron. Soc. **307**, 725 (1999).
4. J. D. Kraus, *Radio Astronomy* (McGraw-Hill, New York, 1967; Sov. Radio, Moscow, 1973).
5. L. Rudnick and T. W. Jones, Astron. J. **88**, 518 (1983).
6. R. E. Rusk, Ph.D. Thesis (Univ. of Toronto, 1988).
7. J. M. Wrobel, Astron. J. **106**, 444 (1993).
8. M. Simard-Normandin, P. P. Kronberg, and S. Button, Astrophys. J., Suppl. Ser. **45**, 97 (1981).
9. C. Reynolds, T. V. Cawthorne, and D. C. Gabuzda, Mon. Not. R. Astron. Soc., in press (2001).
10. B. J. Burn, Mon. Not. R. Astron. Soc. **133**, 67 (1966).
11. L. Rudnick, T. W. Jones, B. K. Edgar, and J. A. Pedelty, Astron. J. **89**, 316 (1984).

Translated by D. Gabuzda

Astronomy Reports, Vol. 45, No. 9, 2001, pp. 676–685. Translated from Astronomicheskiĭ Zhurnal, Vol. 78, No. 9, 2001, pp. 780–790.

A Possible Manifestation of Spiral Shock Waves in the Accretion Disks of Cataclysmic Variables

D. V. Bisikalo[1], A. A. Boyarchuk[1], A. A. Kilpio[1], and O. A. Kuznetsov[2]

[1]*Institute of Astronomy, Russian Academy of Sciences, ul. Pyatnitskaya 48, Moscow, 109017 Russia*

[2]*Keldysh Institute of Applied Mathematics, Russian Academy of Sciences, Miusskaya pl. 4, Moscow, 125047 Russia*

Received January 11, 2001

Abstract—We present the results of three-dimensional numerical simulations of flow structures in binary systems with spiral shock waves. Variations of the mass-transfer rate perturb the equilibrium state of the accretion disk; consequently, a condensation (blob) behind the shock breaks away from the shock front and moves through the disk with variable speed. Our computations indicate that the blob is a long-lived formation, whose mean parameters do not vary substantially on timescales of several tens of orbital periods of the system. The presence of the spiral shocks maintains the compact blob in the disk: it prevents the blob from spreading due to the differential motion of matter in the disk, and dissipative spreading on this timescale is negligible. A number of cataclysmic variables display periodic or quasi-periodic photometric variations in their light curves with characteristic periods ~0.1–0.2$P_{\rm orb}$, where $P_{\rm orb}$ is the orbital period. The blobs formed in systems with spiral shock waves are examined as a possible origin for these variations. The qualitative (and, in part, quantitative) agreement between our computations and observations of IP Peg and EX Dra provides evidence for the efficacy of the proposed model. *© 2001 MAIK "Nauka/Interperiodica".*

1. INTRODUCTION

The light curves of cataclysmic variables with large orbital inclinations, particularly eclipsing stars, provide information about the structure of matter flows between the components of the system. The light curves of such cataclysmic variables are extremely complicated; substantial brightness variations are seen even out of eclipse [1, 2]. Some of these fluctuations, so-called flickering, are non-periodic, and have low amplitudes and short timescales. At the same time, along with sporadic short-period fluctuations, the light curves of cataclysmic variables display periodic (or quasi-periodic) photometric modulations with characteristic periods ~0.1–0.2$P_{\rm orb}$, where $P_{\rm orb}$ is the orbital period.

Various mechanisms have been proposed to explain out-of-eclipse brightness variations, from instabilities in the accretion disk and stream–disk system to changes in the rate of mass transfer from the donor star (see, for example, [2]). Based on three-dimensional numerical simulations, it was concluded in [3] that, in the presence of spiral shock waves, perturbations in the disk result in the formation of a condensation (blob) that moves through the disk with variable speed. The substantial (factor of 1.5) difference between the densities of the blob and disk, as well as the variable speed of rotation of the blob in the disk (~0.1–0.2$P_{\rm orb}$), while the disk rotates with a roughly constant period, suggest this formation as a possible origin of the quasi-periodic variations observed in the light curves of cataclysmic variables out of eclipse. If the blob is more luminous than the disk—as could be the case, for example, for recombination radiation, for which the intensity is proportional to the square of the density—brightness fluctuations could occur due to the eclipse of the blob by the optically thick disk. If the blob is less luminous than the disk, brightness fluctuations could be associated with eclipses of parts of the disk by the optically thick blob.

The aim of the current paper is a more detailed (compared to [3]) study of the formation of the blob, and of the range of variations of its properties as a function of the model parameters. We also analyze observations of two eclipsing binaries with spiral shock waves (IP Peg and EX Dra), to test the ability of the proposed mechanism to explain the observed fluctuations of their light curves.

2. NUMERICAL SIMULATIONS OF CATACLYSMIC VARIABLES WITH VARIABLE MASS-TRANSFER RATES

In [3], we presented results for three-dimensional gas dynamical simulations of matter flows in a semi-detached binary after termination of the mass transfer between the system's components. Investigation of the structure of the residual accretion disk indicated that the flow pattern is substantially altered, even about $0.2P_{\rm orb}$ after the time of mass-transfer termination. The stream from the Lagrange point L_1 disappears, and its effect on the flow structure stops. The shape of the accretion disk changes from initially quasi-elliptical to essentially circular. The gravitation of the donor star leads to the formation of a second spiral shock wave in

1063-7729/01/4509-0676$21.00 © 2001 MAIK "Nauka/Interperiodica"

the disk. In systems with a constant mass-transfer rate, however, this spiral arm is suppressed by the stream from L_1. The results of the simulations presented in [3] indicate that a blob moving through the disk with variable speed forms in the residual accretion disk. The blob is a condensation located behind the spiral shock wave in the steady-state solution. When the stream ceases to feed the disk with matter—i.e., when the equilibrium state of the disk is disrupted—the blob breaks away from the wave front and begins to move in the disk. It is obvious that, in the course of its motion, the blob should spread due to both differential rotation of the disk and to dissipation. Dissipative spreading of the blob occurs on the viscosity timescale, which is from tens to hundreds of orbital periods of the system, for values of the parameter $\alpha \sim 0.01$–0.1 that are typical for cataclysmic variables (where α is the dimensionless Shakura–Sunyaev parameter):

$$\tau_{\text{visc}} = \frac{R_{\text{disk}}^2}{\nu} = \frac{R_{\text{disk}}^2}{\alpha c H} = \frac{R_{\text{disk}} V_K}{\alpha c^2} \approx \frac{1}{\alpha \beta^2 \Omega_K},$$

where R_{disk} is the characteristic radius of the disk, ν is the kinematic viscosity, c is the sound speed, H is the height of the disk, $\beta = H/R_{\text{disk}} = c/V_K$, and Ω_K and V_K are the angular and linear rotational velocities of the Keplerian disk, respectively. This expression can be rewritten in the more convenient form

$$\frac{\tau_{\text{visc}}}{P_{\text{orb}}} = \frac{\Omega_{\text{orb}}}{2\pi\alpha\beta^2\Omega_K} = \frac{\sqrt{1+q}}{2\pi\alpha\beta^2}\left(\frac{R_{\text{disk}}}{A}\right)^{3/2},$$

where P_{orb} is the orbital period, q the ratio of the masses of the donor star and accretor, and A the distance between the system components. In our computations, the characteristic values of these parameters are $\beta \sim 0.1$–0.15 and $R_{\text{disk}}/A \sim 0.3$–$0.4$, which for $\alpha \sim 0.1$ yields $\tau_{\text{visc}} \sim 25P_{\text{orb}}$ and for $\alpha \sim 0.01$ yields $\tau_{\text{visc}} \sim 250P_{\text{orb}}$. In [3], we computed disk lifetimes for various values of α, which yielded slightly smaller, but comparable, values for τ_{visc}. Note that these viscosity timescales for spreading of the blob only set a lower limit for its lifetime, since the probability of recurrent disruption of the disk equilibrium due to variations of the mass-transfer rate is fairly high over such appreciable time intervals.

Spreading due to the differential motion of matter in the disk should influence the fate of the blob more strongly. This process occurs on dynamical timescales, and can lead to the disappearance of the blob over several disk rotations, i.e., over less than one orbital period of the system. However, our three-dimensional computations of the flow pattern in [3] indicated that dynamical spreading of the blob is hindered by the spiral shock wave in the disk. The blob condenses and becomes more compact each time it passes through the spiral wave front, and this effect remains up to the time of disappearance of the wave. Note also that the density contrast in the blob does not begin to decrease until the spiral shocks disappear.

Since the total termination of mass transfer in a system is rare, the question arises of whether a blob can originate in the presence of relatively small variations of the mass-transfer rate. Here, we present the results of a study of the flow structure in a semi-detached binary after decrease of the mass-transfer rate by factors of two and ten. Unlike the case of total termination of the mass transfer, when the computations stop after the disappearance of the disk, these computations indicate that, after non-stationary variations of the flow structure due to the decrease of the mass-transfer rate, a recurrent quasi-steady mode is established, characterized by other values for the disk density. In principle, the establishment of a final, recurrent, steady-state mode requires that computations be carried out over a timescale that is comparable to the viscous lifetime of the disk. However, we restricted our consideration to about the first twenty orbital periods, since this is the characteristic timescale for the flare activity in cataclysmic variables that generates the spiral shocks.

Here, we note only the main features of our numerical model, since it is described in detail in [3]. We used a system of three-dimensional Euler equations to describe the flow. The system was constrained by the equation of state of an ideal gas with an adiabatic index close to unity ($\gamma = 1.01$), making it possible to imitate a system with radiation losses. The remaining dimensionless parameters of the problem specifying the gas dynamical solution were the component mass ratio $q = 1$ and ratio of the sound speed at L_1 and the orbital speed $\epsilon = c(L_1)/A\Omega = 0.1$. The flow was simulated within the parallelepiped $[0.5A..1.5A] \times [-0.5A..0.5A] \times [0..0.25A]$ (due to the symmetry of the problem about the equatorial plane, computations were made only in the upper half-space). The accretor was represented by a sphere with radius 0.01 cut out of the computation region. Computations were made on a $61 \times 61 \times 17$ grid, and the numerical viscosity in α-disk terminology corresponded roughly to $\alpha = 0.05$. To solve the system of equations, we used a high-order Roe–Osher TVD scheme [4, 5] as modified by Einfeldt [6]. We used the previously obtained solution for steady-state mass transfer rate for the initial conditions. Further, we assumed that, at time $t = t_0$, corresponding to the steady-state flow regime, the mass-transfer rate decreases by a factor of two for case A and ten for case B.

Figure 1 presents the time dependence of the average density of matter passing through the half plane perpendicular to the plane of the system and intersecting the disk along the line connecting the components in the direction from the accretor to the outer Lagrange point for cases A (upper curve) and B (lower curve). We can see quasi-periodic density fluctuations due to the blob's passage, along with the general density variations. These curves indicate that, after varying (decreasing) the mass-transfer rate, a condensation forms in the disk and moves with period $\sim 0.15P_{\text{orb}}$ for case A and $\sim 0.18P_{\text{orb}}$ for case B. After the establishment of a recurrent quasi-

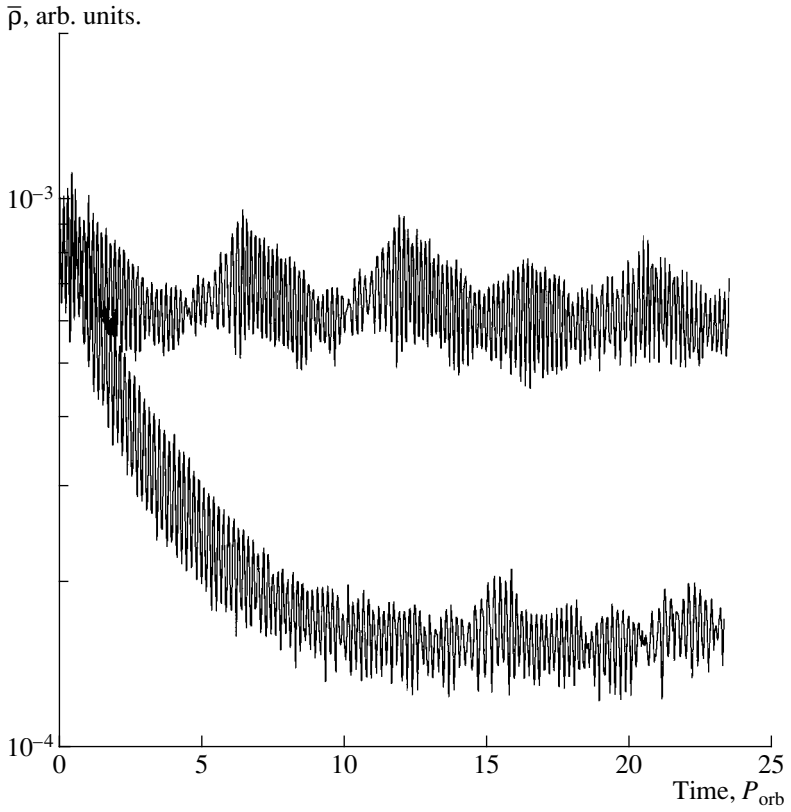

Fig. 1. Time variation of the average density of matter passing through the half plane perpendicular to the plane of the system and intersecting the disk along the line connecting the system components in the direction from the accretor to the outer Lagrange point, for computations A (upper curve) and B (lower curve).

steady regime—i.e., on a timescale $t > t_0 + 3P_{orb}$ for case A and $t > t_0 + 13P_{orb}$ for case B—the orbital period of the blob increases slightly to $\sim 0.16P_{orb}$ for case A and $\sim 0.2P_{orb}$ for case B. Note also that Fig. 1 shows long-period oscillations of the density after the establishment of the recurrent steady regime; the modulation periods for case A and B are $\sim 5.1P_{orb}$ and $\sim 2.5P_{orb}$, respectively.

Let us now consider a Fourier analysis of the curves in Fig. 1. Figure 2 presents the relation between the amplitudes of the Fourier harmonics and the oscillation period for cases A and B. Figure 2a clearly displays two dominant harmonics with periods $0.155P_{orb}$ and $0.165P_{orb}$. The beating between these harmonics yields a supplementary frequency corresponding to the period $\sim 5.1P_{orb}$ of the long-period oscillations in case A. For case B (Fig. 2b), we can see two peaks with periods $0.18P_{orb}$ and $0.21P_{orb}$; the beating between these results in long-period oscillations with period $\sim 2.5P_{orb}$.

Let us consider the variations in the flow structure that occur after the decrease in the mass-transfer rate. Figure 3 presents for density contours case A in the equatorial plane of the system for the six times $t = t_0 + 0.44P_{orb}$, $0.47P_{orb}$, $0.49P_{orb}$, $0.52P_{orb}$, $0.54P_{orb}$, and $0.57P_{orb}$, which cover the orbital period of the blob. The maximum density in Fig. 3 is $\rho \simeq 0.035\rho(L_1)$. The data in this figure correspond to the transition period, when the stream of dense matter from L_1 present in the steady-state solution at $t = t_0$ decreases. At this time, the relatively dense disk determines the entire flow pattern, while the gas of the rarified stream, whose density has been halved, does not affect the solution appreciably. This time interval begins when remnants of the former stream join the disk, i.e. after $\sim 0.2P_{orb}$, and finishes when a new steady-state solution and a single morphology for the stream–disk system have been established. In this time interval, the denser disk matter determines the solution. The shape of the residual accretion disk changes from initially quasi-elliptical to essentially circular. In the computed structure of the accretion disk, a second spiral shock arm is formed in the third and fourth quadrants of the coordinate plane, apart from that already existing in the first and second quadrants.

Also for case A, Fig. 4 presents density contours in the equatorial plane of the system for the additional six times $t = t_0 + 17.64P_{orb}$, $17.67P_{orb}$, $17.70P_{orb}$, $17.73P_{orb}$, $17.76P_{orb}$, and $17.79P_{orb}$. This set of times again covers the orbital period of the blob, in the time interval after the establishment of the recurrent quasi-steady regime. The maximum density in Fig. 4 is $\rho \simeq 0.02\rho(L_1)$. The

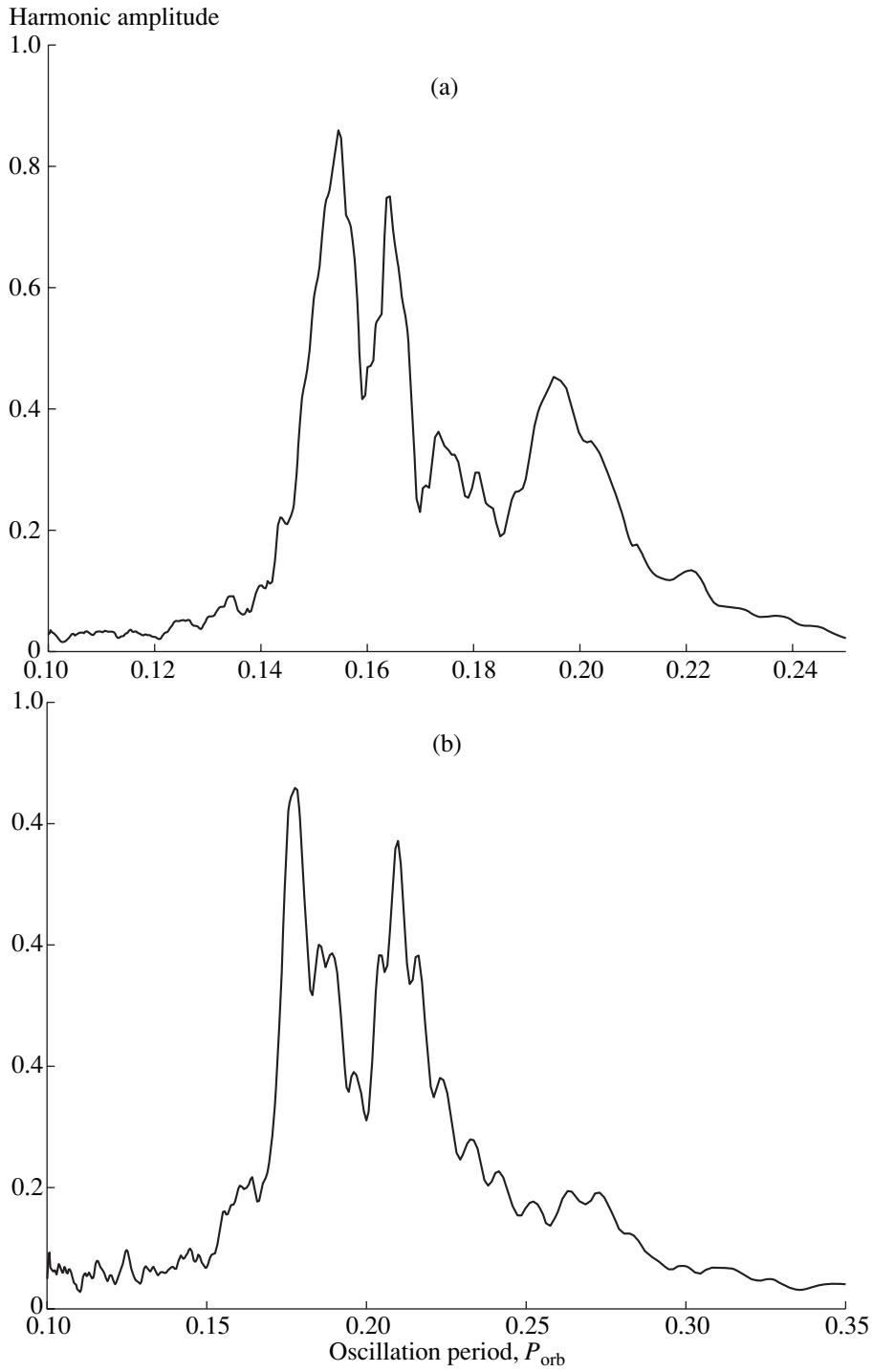

Fig. 2. Amplitudes of the Fourier harmonics as a function of oscillation period for cases (a) A and (b) B.

computed flow structure does not differ dramatically from the solution for the steady-state case (see, for example, [3, 7, 8]). In the flow pattern obtained, the stream flowing from the inner Lagrange point dominates. A single morphology can clearly be seen for the stream–disk system, manifest, in particular, in the quasi-elliptical shape of the disk and the absence of a "hot spot" at the point of contact of the stream and disk ($X \simeq 0.8A$, $Y \simeq -0.1A$). At the same time, it is clear that the interaction between the binary envelope and the flow results in the formation of an extended shock wave (hot line) along the boundary of the stream facing the orbital rotation. Figure 4 also shows that only one arm of the spiral shock located in the first and second quadrants of the coordinate plane

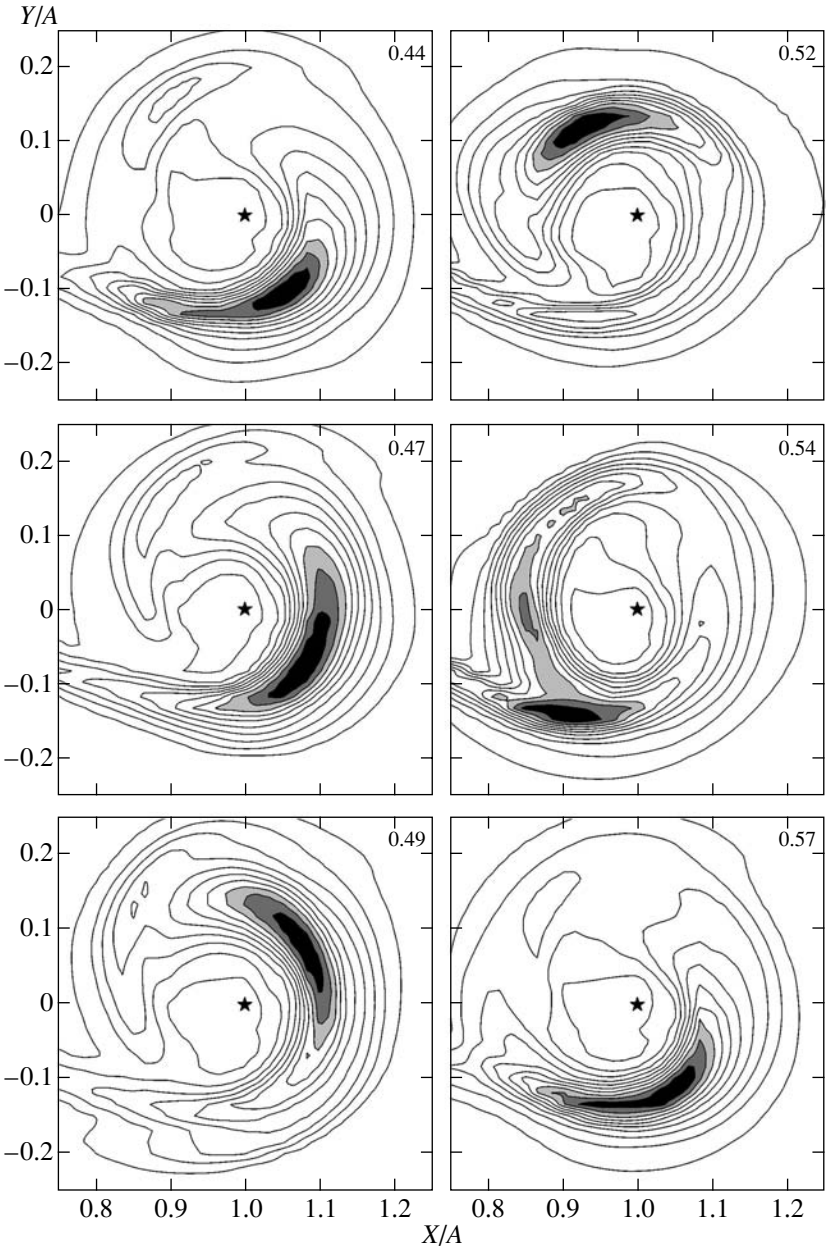

Fig. 3. Density distributions in the equatorial plane of the system (case A). Results are presented for the six times $t = t_0 + 0.44P_{orb}$, $0.47P_{orb}$, $0.49P_{orb}$, $0.52P_{orb}$, $0.54P_{orb}$, and $0.57P_{orb}$, which cover the orbital period of the blob (the values for $(t - t_0)/P_{orb}$ are indicated on the plots). In all plots, the maximum density is $\rho \simeq 0.035\rho(L_1)$. The asterisk denotes the accretor.

remains in the system. In the place where the other arm was formerly located, the flow is now determined by the stream from L_1, which hinders the formation of the second arm of the spiral shock. The distinction of this case from the steady-state solution [3, 7, 8] is that the blob continues to exist, resulting in periodic variations of the disk structure. We can see from Fig. 4 that, as the blob moves in the disk, there is a tendency for it to be redistributed uniformly, due to the differential motion of the disk matter. However, when the condensation passes through the remaining spiral arm, the matter behind the wave decelerates, reforming or maintaining the compact condensation. Consequently, we can see periodic variations of the disk structure in the resulting solution, even after the establishment of the recurrent quasi-steady regime.

Recall that the Fourier analysis (Fig. 2a) revealed two harmonics with periods $0.155P_{orb}$ and $0.165P_{orb}$, which dominate the solution for case A and result in long-term oscillations with period $\sim 5.1P_{orb}$. The computations indicate that the first harmonic, with the shorter period, is due to the interaction between the blob's central region (core) and the spiral shock in the

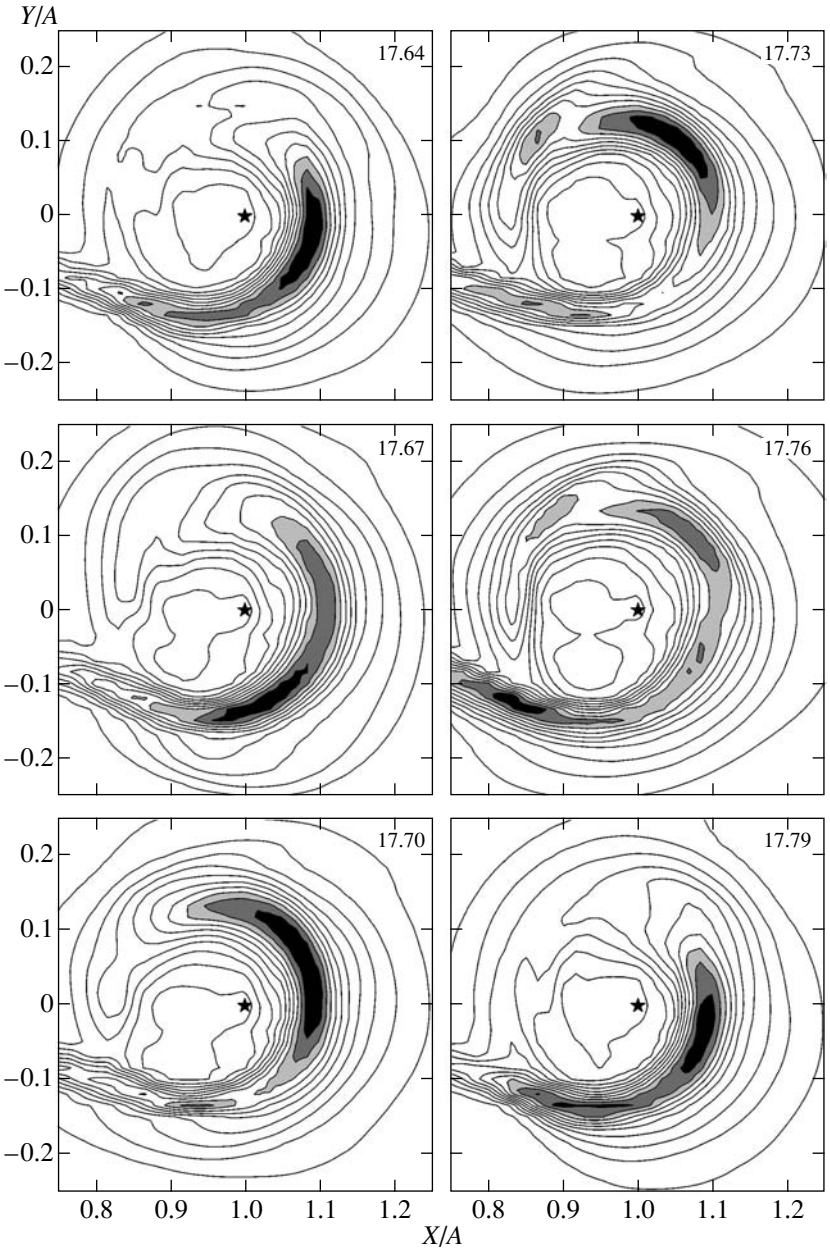

Fig. 4. Same as Fig. 3 for the six times $t = t_0 + 17.64P_{orb}$, $17.67P_{orb}$, $17.70P_{orb}$, $17.73P_{orb}$, $17.76P_{orb}$, and $17.79P_{orb}$. In all plots, the maximum density is $\rho \simeq 0.02\rho(L_1)$.

first and second quadrants of the coordinate plane. The second harmonic is associated with the interaction between peripheral areas of the blob and the stream from L_1, and its period is somewhat longer than that of the first harmonic. This increase of the period of the second harmonic is due to the fact that, after the blob breaks away from the spiral shock, its various parts begin to move in accordance with the differential motion of the disk matter. Accordingly, when they pass from the wave to the stream, the edges of the blob lag behind its core, and the period corresponding to the interaction between these peripheral regions and the stream becomes larger than the period of the first harmonic. Further, as the blob reaches the spiral wave, the lag between the edges and core of the blob decreases and the blob becomes compact again.

Comparison of the data in Figs. 1–4 shows that, in spite of the decrease in the number of spiral waves maintaining the blob, the blob's average period remains essentially the same during the change from the transitional (two waves) to the new steady-state (one wave) solution. At the same time, the long-period modulations lead to appreciable variations of the density contrast in the blob–disk system. Figure 5 presents the density

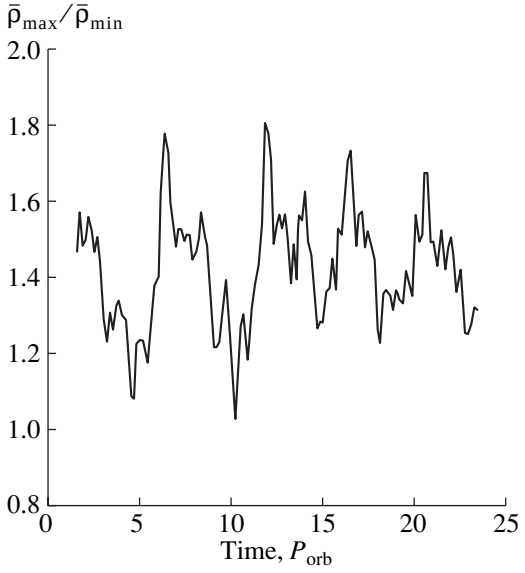

Fig. 5. Time dependence of the blob–disk density contrast for case A.

contrast in the blob–disk system for the case A computations. At the time of restructuring of the solution, when the flow structure is determined by the denser disk, the contrast is ~1.5. Further, after the establishment of the recurrent quasi-steady regime, when the second harmonic appears due to the blob–stream interaction, resulting in long-period oscillations, the density contrast varies from ~1.1 to ~1.8.

As noted above, after the establishment of the new quasi-steady regime, solution A is determined by the stream from L_1, and variations in the flow pattern due to the blob essentially reduce to periodic variations of the disk structure. In case B, however, the mass-transfer rate has decreased by a factor of ten, and the gas in the stream has a substantially lower density. Therefore, even after the establishment of the new quasi-steady regime, the blob alters the entire flow pattern rather than simply affecting the disk structure. One manifestation of this is that the dense gas of the blob sweeps away the stream matter when it reaches the stream. This is illustrated in Fig. 6, which presents density contours in the equatorial plane of the system for six times $t = t_0 + 22.45P_{orb}$, $22.48P_{orb}$, $22.51P_{orb}$, $22.54P_{orb}$, $22.57P_{orb}$, and $22.61P_{orb}$, which cover the orbital period of the blob after the establishment of the new steady-state regime for case B. The maximum density in Fig. 6 is $\rho \simeq 0.0035\rho(L_1)$. This testifies that, in the case of a substantial decrease of the mass-transfer rate in the system, the forming blob affects the flow pattern appreciably at all stages of the computations. The dominant harmonics in solution B have periods $0.18P_{orb}$ and $0.21P_{orb}$, and yield the period for long-term oscillations $\sim 2.5P_{orb}$. As in case A, these harmonics appear to originate due to the interaction of the blob with the spiral shock and with the stream from L_1.

The computation results presented here and in [3] indicate that, in a semi-detached binary with spiral shocks in its disk, even a small perturbation of the steady flow regime due to a decrease in the mass-transfer rate results in the formation of a blob. Moreover, since the mechanism for maintaining the blob on dynamical timescales—the presence of spiral waves—is not associated with variations in the mass-transfer rate, it is natural to suppose that not only variations of the mass-transfer rate, but also other perturbations of the equilibrium structure of the disk will lead to the formation of a moving blob in the disk. The lifetime of the blob is determined by the presence of spiral waves in the disk, which hinder its dynamical spreading, and also by dissipation in the disk.

3. PARAMETERS OF THE BLOB AND VARIABILITY OF THE LIGHT CURVES FOR CATACLYSMIC VARIABLES WITH SPIRAL SHOCK WAVES

Spiral waves in the disk or, more precisely, condensations located behind the arms of the spiral wave fronts, have been considered as a possible origin of variability in astrophysical objects in a number of studies (see, for example, [9]). In [3], we first showed that a condensation behind a spiral wave in the disk could break away from the wave front, and then move through the disk without spreading over tens of orbital periods. In the computations of [3] and the present study, the disruption of the disk equilibrium that results in the breakaway of the blob was induced by variations in the mass-transfer rate in the system. Once it has appeared, this condensation experiences a tendency to spread over the disk uniformly, due to the differential motion of matter in the disk; however, when the condensation passes through the spiral shock, the matter behind the wave decelerates, reforming or maintaining the compact condensation. Further, as the density contrast between the blob and disk increases, and with it the pressure gradient between the condensation and disk, there comes a time when the blob again begins its movement through the disk. However, with the next passage of the spiral wave front, the matter behind the wave again decelerates, and the process of reforming or maintaining the condensation recurs.

Our computations indicate that the blob moves through the disk over tens of orbital periods, keeping its basic parameters essentially unchanged. Note that the parameters of the blob should vary under the action of dissipation processes; however, the characteristic timescales for the disk viscosity are much longer than those over which the computations were carried out, so that these variations of the blob parameters are negligible. Note also that the limited time for the computations (restricted to $\sim 25P_{orb}$) was not chosen arbitrarily, and was determined by the characteristic time from an outburst maximum to the egress from outburst (of the order of tens of P_{orb}). It is at the stage of egress from an outburst that a decrease of the mass-transfer rate is possible in cataclysmic variables; in

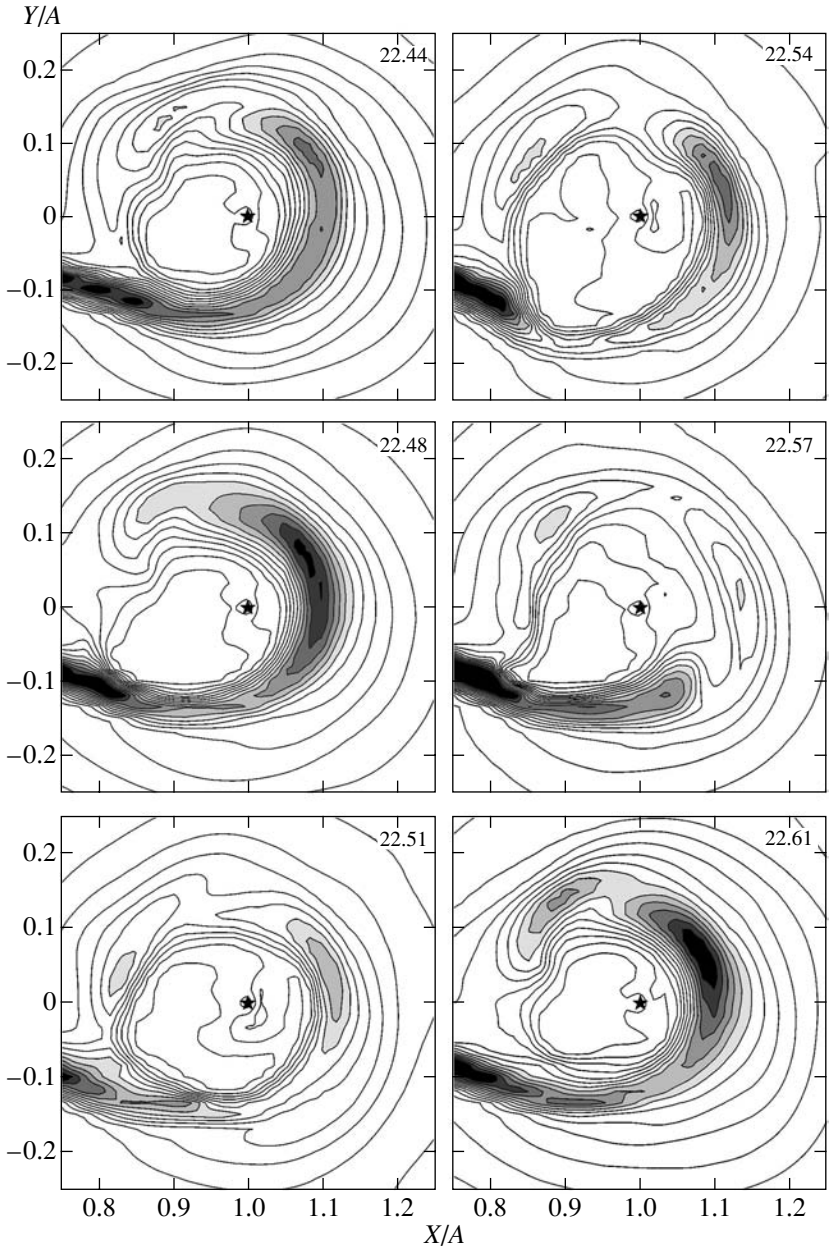

Fig. 6. Same as Fig. 3 for case B. Results are presented for the six times $t = t_0 + 22.45P_{orb}$, $22.48P_{orb}$, $22.51P_{orb}$, $22.54P_{orb}$, $22.57P_{orb}$, and $22.61P_{orb}$, which cover the orbital period of the blob. In all plots, the maximum density is $\rho \simeq 0.0035\rho(L_1)$.

addition, spiral waves are observed in cataclysmic variables (or, more exactly, there is the strongest evidence for their possible existence) at these times.

Determining the blob characteristics typical for cataclysmic variables requires a broad range of computations. Nevertheless, the results of [3] and the current study enable us to conclude even at this stage that the main orbital period of the blob depends on the viscosity: for the solution with $\alpha \sim 0.05$, it is roughly equal to 0.15–$0.2P_{orb}$, while it is about 0.1–$0.15P_{orb}$ for $\alpha \sim 0.01$. This means that, for the characteristic viscosities in accretion disks $\alpha \sim 0.01$–0.1, the orbital period of the blob will be 0.1–$0.25P_{orb}$. An important parameter of the blob determining its observational manifestations is the contrast of its density relative to that of the disk. As shown above, the density contrast in the blob–disk system depends on the changes in the mass-transfer rate, and varies periodically with time; the density contrast ~1.5 can be adopted as an average value for the various computations. The unified mechanism for the formation and maintenance of the blob suggests that the average density contrasts for the blob–disk systems in different cataclysmic variables may not differ too substantially from this value.

Let us consider possible observational manifestations of a blob in the accretion disk of a binary system and compare these with observations. Since the existence of the blob is maintained by spiral shocks, we will use observations of the systems IP Peg, for which the presence of spiral shocks was first suggested [10, 11], and EX Dra, in which spiral shocks very likely exist [12–14].

Since spiral shock waves in the disk maintain the blob (prevent it from spreading), we will consider to what extent variations in the light curves are related to the formation and/or disappearance of the spiral shocks in these systems. Interpretations of the available observations for IP Peg and EX Dra propose that, during an outburst, the accretion disk in the system swells, and, at some stage, spiral shock waves originate in it. After the outburst, the radius of the disk decreases and, in the transition to the inactive state, it probably becomes so small that tidal perturbations can no longer maintain spiral waves. Accordingly, the light curves of these systems should display pronounced quasi-periodic variations only during and some time after outburst. Note that the dissipative spreading in a disk with low viscosity is small, so that the blob can exist for a fairly long time even after the disappearance of the spiral shocks; accordingly, light-curve oscillations may be seen after the disappearance of the spiral shocks, though with decreased amplitude. During and immediately following outburst, both systems do display pronounced variations in the out-of-eclipse portions of their light curves, with periods ~ 0.1–$0.2P_{\rm orb}$; for both EX Dra [15] and IP Peg [16, 17], these variations decrease appreciably during the transition to the quiescent state. Thus, the proposed mechanism is justified qualitatively: oscillations in the out-of-eclipse portions of the light curves can occur due to the appearance of spiral shocks and, accordingly, of a blob in the disks. Note that the period of these variations corresponds to the computed orbital period of the blob.

As a second test of the applicability of the proposed mechanism, let us consider some quantitative predictions. Analyses of light curves during outburst indicate that most of the luminosity is from the disk (~5/6 for IP Peg [18]); therefore variations of the light curve and of the density contrast between the blob and disk should be comparable. The computations yielded an average density contrast of ~1.5; taking into account the contribution from the disk to the total luminosity, we should expect luminosity variations of ~40%. Observations show that the characteristic amplitudes for out-of-eclipse variations are ~30% for IP Peg (see, for example, [19, 20]) and ~15% for EX Dra [15]. Unfortunately, analysis of variations in the quiescent state is appreciably complicated by the fact that, in addition to the decrease of the blob–disk density contrast, the contribution from the disk itself to the total luminosity decreases (~1/5 for IP Peg [18]). Therefore, we will restrict our consideration to quantitative estimates made for outburst. A comparison of these estimates indicates that the proposed mechanism is also plausible quantitatively.

Additional support for our mechanism is its ability to qualitatively explain observed variations of emission-line profiles in cataclysmic variables. For example, observations of H_α profiles in the disk of the SS Cyg system [21] revealed appreciable asymmetry, as well as substantial variations of the distance between the two peaks of the profile. The presence of spiral waves in the disk alone can explain the asymmetry in the disk lines [9]; however, it provides no explanation for the variation of the distance between the profile peaks. Our mechanism is able to explain both the profile asymmetry (in the same way as in the case of spiral shocks alone) and the variability of the distance between the peaks (via variability of the projection of the rotational velocity of the blob). Note also that sporadic small-amplitude variations of light curves, so-called flickering, may also be due to the presence of the blob in the disk. Perturbations of the disk structure due to the periodic passes of the blob, as well as the interaction of the blob with the stream, could lead to a variety of small-scale oscillations, observed as sporadic fluctuations of the light curve.

4. CONCLUSION

The light curves of cataclysmic variables with spiral shock waves indicate the presence of periodic or quasi-periodic photometric variations with characteristic periods ~ 0.1–$0.2P_{\rm orb}$. Three-dimensional gas dynamical simulations of the matter flows in binary systems with spiral shocks show that, when their accretion disks are perturbed by variations in the mass-transfer rate, a steady condensation (blob) originates and subsequently moves through the disk with variable speed. The long lifetime of the blob, the computed blob–disk density contrast (on average about 1.5), and the characteristic blob orbital period (~ 0.1–$0.2P_{\rm orb}$) suggest this object as a possible origin of the observed quasi-periodic variations of the light curves of cataclysmic variables out of eclipse. If the proposed mechanism does operate, the presence of this type of variability in the light curves of cataclysmic variables can provide additional evidence for the existence of spiral shock waves in these systems.

ACKNOWLEDGMENTS

This work was supported by the Russian Foundation for Basic Research (project codes 99-02-17619, 00-01-00392, 00-02-17253), and by grants of the President of the Russian Federation (99-15-96022, 00-15-96722). The authors are grateful to A.M. Friedmann and O.V. Khoruzhii for useful comments.

REFERENCES

1. C. la Douse, in *Cataclysmic Variables and Related Objects*, Ed. by M. Hack and C. la Douse (NASA, Washington, 1993), NASA SP-507.

2. B. Warner, *Cataclysmic Variable Stars* (Cambridge Univ. Press, Cambridge, 1995).
3. D. V. Bisikalo, A. A. Boyarchuk, A. A. Kil'pio, and O. A. Kuznetsov, Astron. Zh. **78** (8), 707 (2001) [Astron. Rep. **45**, 611 (2001)].
4. P. L. Roe, Ann. Rev. Fluid Mech. **18**, 337 (1986).
5. S. Osher and S. Chakravarthy, SIAM J. Numer. Anal. **21**, 955 (1984).
6. B. Einfeldt, SIAM J. Numer. Anal. **25**, 294 (1988).
7. D. V. Bisikalo, A. A. Boyarchuk, V. M. Chechetkin, *et al.*, Mon. Not. R. Astron. Soc. **300**, 39 (1998).
8. D. V. Bisikalo, P. Harmanec, A. A. Boyarchuk, *et al.*, Astron. Astrophys. **353**, 1009 (2000).
9. S. K. Chakrabarti and P. J. Wiita, Astron. Astrophys. **271**, 216 (1993).
10. D. Steeghs, E. T. Harlaftis, and K. Horne, Mon. Not. R. Astron. Soc. **290**, 28 (1997).
11. E. T. Harlaftis, D. Steeghs, K. Horne, *et al.*, Mon. Not. R. Astron. Soc. **306**, 348 (1999).
12. R. Baptista and M. S. Catalan, astro-ph/9905096 (1999).
13. V. Joergens, K. H. Mantel, H. Barwig, *et al.*, Astron. Astrophys. **354**, 579 (2000).
14. V. Joergens, H. C. Spruit, and R. G. M. Rutten, Astron. Astrophys. **356**, L33 (2000).
15. R. Baptista, M. S. Catalan, and L. Costa, Mon. Not. R. Astron. Soc. **316**, 529 (2000).
16. T. R. Marsh and K. Horne, Astrophys. J. **349**, 593 (1990).
17. N. A. Webb, T. Naylor, Z. Ioannou, *et al.*, Mon. Not. R. Astron. Soc. **310**, 407 (1999).
18. T. S. Khruzina, A. M. Cherepashchuk, D. V. Bisikalo, *et al.*, Astron. Zh. **78** (7), 625 (2001) [Astron. Rep. **45**, 538 (2001)].
19. L. Morales-Rueda, T. R. Marsh, and I. Billington, Mon. Not. R. Astron. Soc. **313**, 454 (2000).
20. D. Steeghs, K. Horne, T. R. Marsh, *et al.*, Mon. Not. R. Astron. Soc. **281**, 626 (1996).
21. L. G. Martínez-País, F. Giovannelli, C. Rossi, *et al.*, Astron. Astrophys. **291**, 455 (1994).

Translated by K. Maslennikov

Astronomy Reports, Vol. 45, No. 9, 2001, pp. 686–691. Translated from Astronomicheskiĭ Zhurnal, Vol. 78, No. 9, 2001, pp. 791–797.

The Dependence of the Characteristics of the Brightness Variability of Herbig Ae/Be Stars on the Orientation of Their Star–Disk Systems

S. Yu. Mel'nikov

Ulugh Beg Astronomical Institute, Astronomicheskaya ul. 33, Tashkent, 700052 Uzbekistan

Received February 28, 2001

Abstract—We analyze the brightness variability of six Herbig Ae/Be stars: V1331 Cyg, LkHα198 = V633 Cas, AS 442, XY Per, V517 Cyg, and WW Vul. The last two objects are UX Ori stars showing Algol-like brightness dips with amplitudes of $2^m.0$–$2^m.5$. AS 442 and XY Per also exhibit brightness dips but with considerably lower amplitudes, $0^m.3$–$0^m.6$. On the contrary, such dips are not present in the light curves of V1331 Cyg and LkHα198, where stochastic variability with amplitudes of $0^m.1$–$0^m.2$ on timescales of about a day can be seen. AS 442 and XY Per also show stochastic variability, but with lower amplitudes ($\approx 0^m.05$). These different types of variability could be related to the orientations of the star–disk systems. We suggest that the brightness variations in young stars whose disks are viewed edge-on are mainly due to non-uniform absorption, whereas the character of the variability in stars with pole-on disks is determined by non-stationary accretion. © *2001 MAIK "Nauka/Interperiodica".*

Herbig Ae/Be stars are currently thought to be young stars with spectral types earlier than F0 and masses from 2–10$M_\odot$ located in star formation regions. About 90 per cent of Herbig Ae/Be stars exhibit brightness variations, thought to be irregular with amplitudes varying from $0^m.1$ (V) for the least to 3^m– $3^m.5$ for the most active stars. As a rule, for stars with large variability amplitudes, a considerable fraction of the amplitude is contributed by so-called irregular Algol-like brightness dips. These are probably due to occultations of the star by circumstellar formations orbiting in a gas–dust disk [1]. Stars with Algol-like minima have been separated out as a special subgroup, named "UX Ori stars" after one of their most typical representatives.

Algol-like brightness dips make a considerable contribution to the light curves of only some of the most active UX Ori stars. In addition, most UX Ori stars alternate intervals of activity, with maximum variation amplitudes and many Algol-like dips in their light curves, and relatively quiet intervals with variation amplitudes of $0^m.3$–$0^m.6$, which can last for years [2, 3]. During a quiet state, the shape of the light curve of a UX Ori star is fairly similar to those of ordinary Herbig Ae/Be stars.

The second important source of light variations in Herbig Ae/Be stars could be accretion of circumstellar matter onto the star. Accretion is an efficient source of energy; for example, the computations of Hillenbrand *et al.* [4] show that the accretion luminosity of some stars can be as high as 1200–1800$L_\odot$.

Grinin *et al.* [1] assumed that the photometric activity of UX Ori stars was closely related to their spatial orientation, and was highest when the angle i between the symmetry axis of the circumstellar disk and the line of sight was close to 90°. Grinin and Kozlova [5] attempted to relate the photometric activity to $v\sin i$; i.e., to the orientation of the star–disk system.

We decided to analyze the light curves of several Herbig Ae/Be stars, based on the initial assumption that the circumstellar disks (envelopes) of UX Ori stars are viewed edge-on. We use many years of *UBVR* photometry acquired in the course of the ROTOR program at the Mt. Maĭdanak Observatory to analyze the light curves of the Ae/Be stars, and attempt to identify the origins of brightness variations.

From among the many stars observed, we selected six (WW Vul, V517 Cyg, AS 442 = V1977 Cyg, XY Per, V1331 Cyg, and LkHα 198 = V633 Cas), whose light curves, in our opinion, can be subdivided into several subgroups. Below, we present the characteristics of the photometric variability of these stars.

WW Vul (A3ea) is a well known UX Ori star showing brightness dips with amplitudes exceeding 2^m in the V band. Its brightness and color variability have been analyzed in a number of studies (cf., for example, [6, 7] and references therein), and we accordingly use WW Vul only for comparison purposes. Observations of another star, V517 Cyg (A0–5), revealed brightness dips with amplitude $2^m.5$ and photometric features similar to those of WW Vul [8]; combined with the presence of

1063-7729/01/4509-0686$21.00

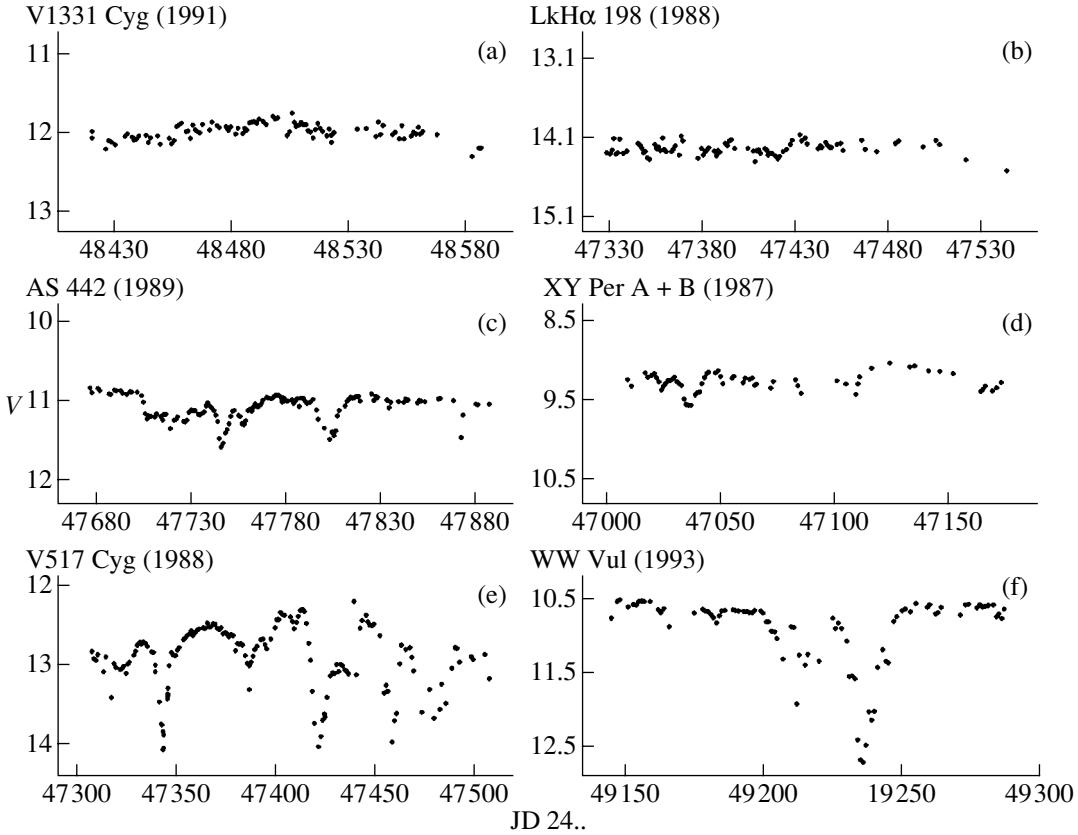

Fig. 1. Light-curve fragments for WW Vul, V517 Cyg, AS 442, XY Per, V1331 Cyg, and LkHα 198, demonstrating different photometric behaviors, depending on the orientations of the star–disk systems.

Hα emission split by a central absorption [9], these facts testify that this star is also a UX Ori variable. Typical light-curve fragments for V517 Cyg (1988) and WW Vul (1993) are presented in Figs. 1e and 1f.

Figures 2e and 2f present changes in *B–V* as a function of *V*, which provide evidence that the variability of the two stars has a similar nature. The solid line is the reddening line. The figure shows that, during brightness dips, the color index first increases approximately in accordance with the interstellar reddening law, then, when the magnitude has dropped below a certain level, begins to decrease (the so-called "blueing effect"). This color-index behavior is characteristic of most UX Ori stars [10].

Algol-like brightness dips are also exhibited by AS 442 (B6–7) and XY Per (A2II+B6) [11, 12], but, in contrast to those in typical UX Ori stars, these dips have much lower amplitudes, $0\overset{m}{.}3$–$0\overset{m}{.}6$. In addition, the dips occur less frequently. For example, 14 years of observations of XY Per, from 1985 until 1998, showed only two dips with amplitude $0\overset{m}{.}6$. Light-curve fragments for AS 442 (1989) and XY Per (1987) are shown in Figs. 1c and 1d. Rapid (apparently stochastic) variability with an amplitude of about $\approx 0\overset{m}{.}05$ also appears in these light curves. The many years of observations have revealed the existence of active periods of AS 442, when the star changes its brightness by $0\overset{m}{.}7$–$0\overset{m}{.}8$, and quiet periods, with brightness changes of $0\overset{m}{.}2$. Similar alternating behavior, though with a wider range of variations, occurs for other UX Ori stars. It is interesting that both AS 442 [13] and XY Per (= ADS 2788) are visual binaries.

Figures 2c and 2d show the dependence of *B–V* on *V* for these stars. We can see that *B–V* becomes redder approximately in accordance with the interstellar reddening law during brightness dips. However, in contrast to classical UX Ori stars, the color tracks do not show any significant turn toward the blue. This is probably due to the small range ($<1^m$ in *V*) of the brightness changes during the Algol-like dips: for UX Ori stars, the tracks turn at dip levels $\Delta m > 1^m$–$1\overset{m}{.}2$ in *V*. However, there is some reason to suspect that the data points for some of the dips for AS 442 (Fig. 2c) are displaced toward the blue, while the data points remain at the reddening line during other, deeper, brightness dips. This effect could be real: similar behavior of color indices during Algol-like dips was observed for another UX Ori star, HR 5999 [14].

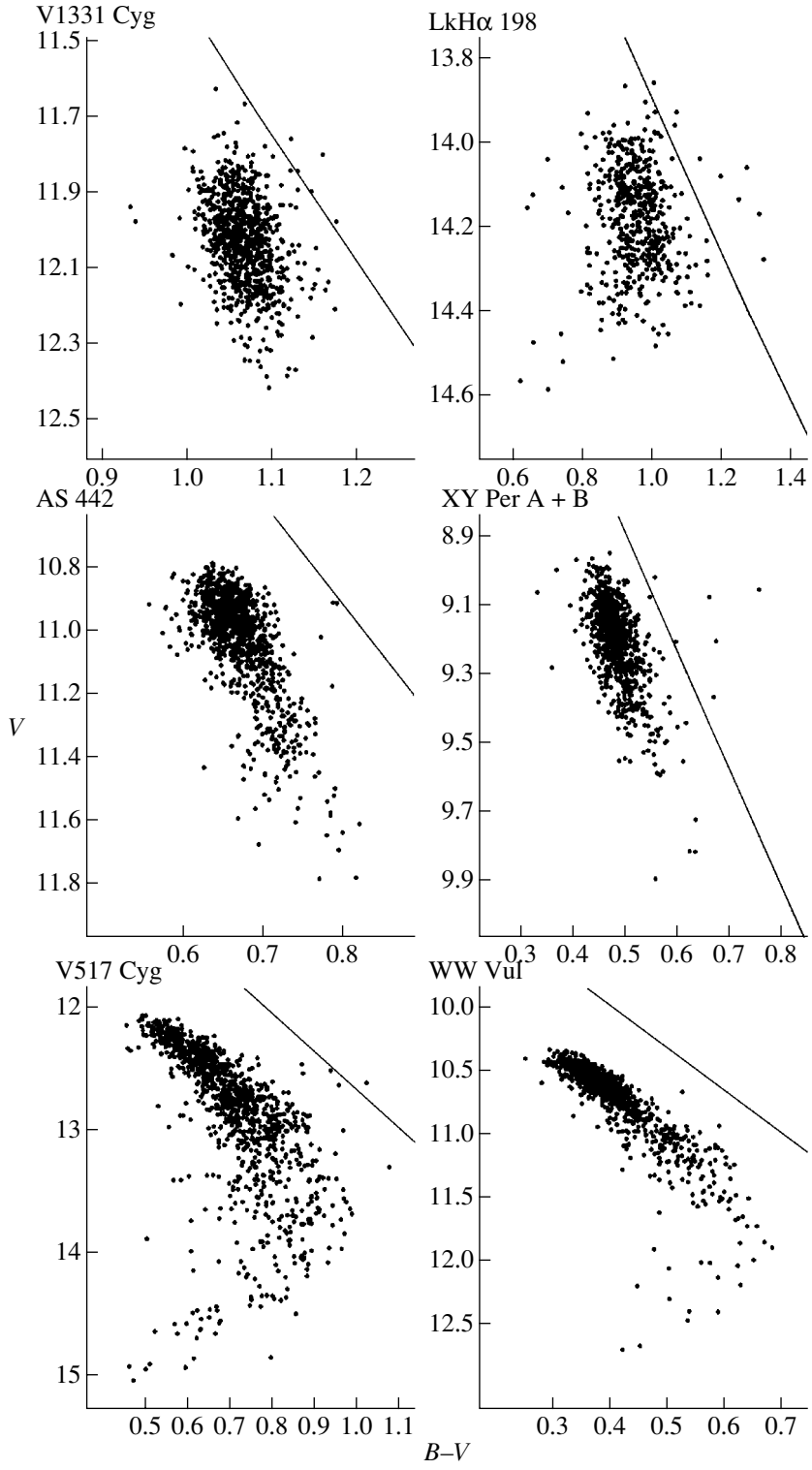

Fig. 2. $V - (B–V)$ diagrams for the six stars showing different spatial orientations.

V1331 Cyg (F0) and LkHα 198 (A5) do not seem to experience Algol-like brightness dips. No light decrease of this kind was recorded in the 12 years of our observations. The light curves of these stars nearly always show stochastic variability with amplitude $0^m.1$–$0^m.2$ (Figs. 1a, 1b). Smooth brightness changes with timescales of 70 to 150 days are visible in the long-term light curves; these could be part of variations with still longer periods that

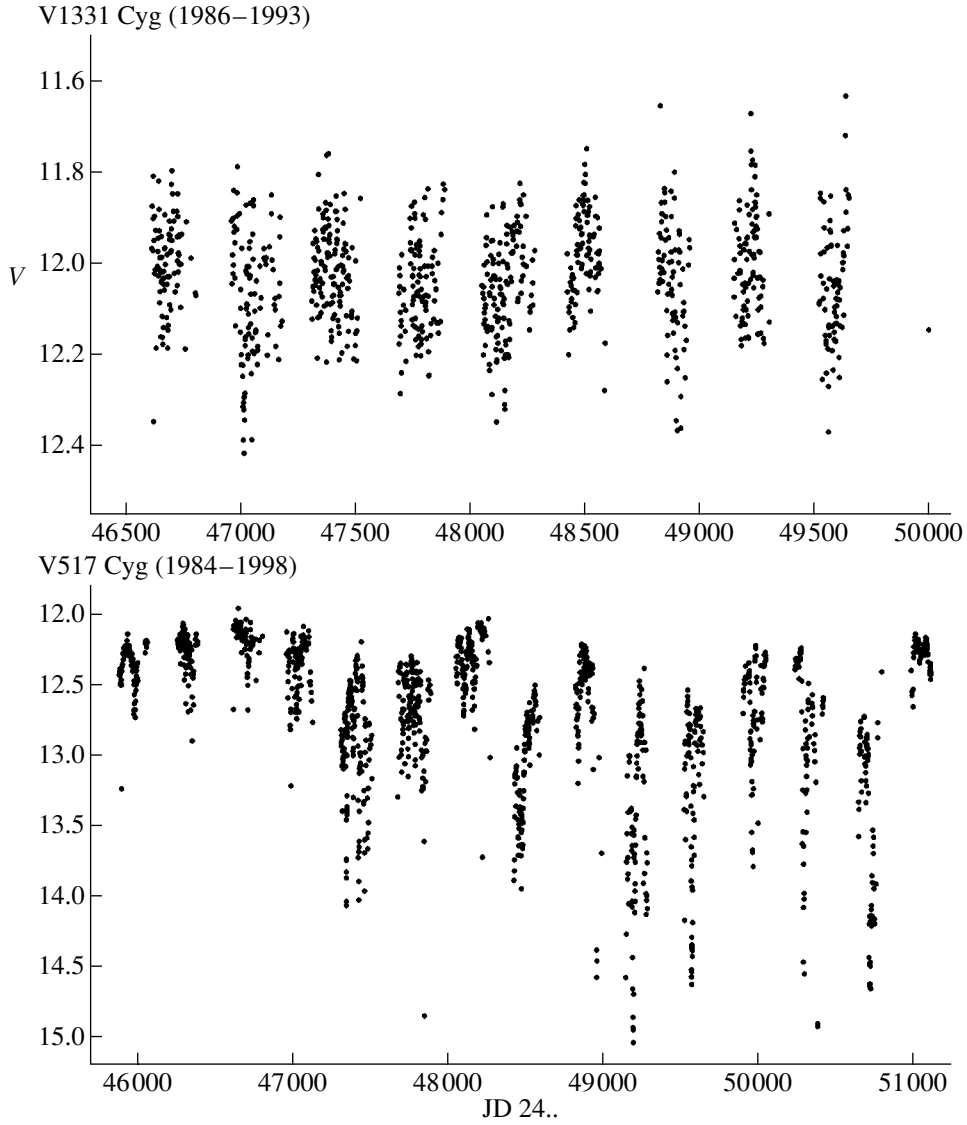

Fig. 3. Long-term light curves of V1331 Cyg and V517 Cyg.

could not be traced completely due to the limited duration of the observing seasons.

It appears from Fig. 2 that the ranges of the *B–V* variations for V1331 Cyg and LkHα 198 are even smaller than for AS 442 and XY Per, since the amplitudes of their *V* changes are smaller, and the tracks show no blueing effect.

Thus, we can tentatively subdivide the program stars into three groups:

Group I (V517 Cyg, WW Vul): Classical UX Ori stars, with the amplitudes of their brightness variations reaching $2^m.5$–3^m (and amplitudes of Algol-like minima 2^m);

Group II (AS 442, XY Per): Low-amplitude UX Ori stars, with the amplitudes of their brightness variations reaching 1^m–$1^m.2$ and amplitudes of Algol-like minima $\approx 0^m.5$–$0^m.7$; the light curves of these stars can display stochastic variability with amplitudes of $0^m.05$;

Group III (V1331 Cyg, LkHα 198): Stars without Algol-like brightness dips, but showing stochastic variability with amplitudes $\approx 0^m.2$.

In this subdivision, the Algol-like brightness dips have their maximum amplitude for V517 Cyg and WW Vul (Group I), a lower amplitude for AS 442 and XY Per (Group II), and completely disappear for V1331 Cyg and LkHα 198 (Group III). The stochastic variability amplitude correspondingly increases from Group I to Group III.

Taken as a whole, the light curves in Fig. 1 demonstrate gradual changes of the variability characteristics

Physical parameters of the six Herbig Ae/Be stars

Star	Spectral type	A_V	P, %	$v \sin i$	EW(H_α), Å	Hα profile
V1331 Cyg	B0.5–F0	2.4		25	–48.4	P Cyg
LkH_α 198	B3e–A5	4.5	1.87R		–66.3	Single
AS 442	B6–7	2.6	3		–18…–23	Double
XY Per	A2II+B6	2.3		95–130	–6	Double
V517 Cyg	A0	2.0	0.88		–15	Double, single
WW Vul	A3e	0.48	1.5	150	–20…–42	Double

from one group of stars to another. In our opinion, these differences in brightness variability can be explained as follows.

The disks of V517 Cyg and WW Vul are probably viewed edge-on (the inclination of the rotation axis to the line of sight is $i \approx 90°$), so that the motion of gas and dust clouds along their Keplerian orbits leads to occultations of the central object, and therefore Algol-like brightness dips with amplitudes $\approx 2^m$.

According to McMuldroch *et al.* [15] and Bastien and Menard [16], the rotation axes of V1331 Cyg and LkHα 198, members of Group III, probably have inclinations to the line of sight $i \approx 60°$. This conclusion was reached in [15, 16] based on an analysis of the orientations of the bipolar molecular flows observed for these stars, whose axes probably coincide with the stellar rotation axes. If these stars are also surrounded by disks, occultations of the central star probably do not occur, and there are different observing conditions for the innermost parts of the accretion disk, where the accretion is actually taking place. It is possible that these zones are no longer screened from terrestrial observers by the outer parts of the optically thick disk. In this case, the stochastic variability in the light curves of V1331 Cyg and LkHα 198 could be the result of non-stationary accretion.

In contrast, the outer parts of the circumstellar disks of UX Ori stars screen the accretion zone, so that the stochastic variability is small or even absent. At some epochs, UX Ori stars also exhibit low-amplitude irregular variability, but we think that it is probably due to variable extinction in the disk rather than non-stationary accretion, though it is impossible to distinguish between these two possibilities without additional spectroscopic studies. Figure 3 presents the long-term light curves of V1331 Cyg and V517 Cyg, which, in our opinion, demonstrate changes in the character of the variability, depending on the orientation of the star–disk system.

AS 442 and XY Per probably have intermediate orientations. On the one hand, they still exhibit Algol-like brightness dips; on the other hand, stochastic variability appears in their light curves (Figs. 1c, 1d). The fact that, in some cases, the scatter of the data points in the light curves decreases during minima (occultations) provides evidence for a connection between the stochastic variability and non-stationary accretion in the stars' immediate surroundings. It is also possible that the disks of these stars are more evolved than those of other UX Ori stars, so that the low amplitude of their Algol-like dips is due to the absence of circumstellar formations with high optical depth in their disks.

The table presents parameters from the literature that can be used to describe the orientations of star–disk systems. Generally speaking, the absorption, A_V, and degree of polarization, $P(\%)$, depend on orientation. On average, these parameters should be largest for stars with disks viewed edge-on. However, it is possible that the relation between these parameters and the orientation is not unique, due to the complex structure and dynamics of circumstellar formations and differences in the interstellar absorption. The value of $v \sin i$ may be a good orientation diagnostic. This quantity is known for three of our objects, and is consistent with our suggestions for the orientations of the three groups. The equivalent width EW(Hα) and profile of the Hα emission line are consistent with gradually changing inclination i of the rotation axis to the line of sight. The flux in Hα emission should increase with decreasing i, since we see an increasing area of Hα emission, and, in addition, the screening of this zone by the optically thick disk decreases. Stars whose disks are viewed at low inclinations i should show single Hα emission profiles, whereas the Hα lines in the spectra of stars whose disks are viewed edge-on should have double profiles divided by a central absorption [9]. The dependence of the intensity of emission lines and the appearance of the UV spectrum on the inclination of star–disk systems was considered by Blondel and Tjin a Djie [17].

We can see in Fig. 2 that, from one group of stars to the next, we observe a gradual increase of the slope of the color index–brightness relation of the star relative to the interstellar reddening line. Since the presence of hot gas influences the color indices, steepening this slope in the color index–brightness diagram, the change of the slope in Fig. 2 could be due to an increasing contribution from a gaseous component.

Another view is that the accretion rates of Herbig Ae/Be stars are not sufficiently high for variations in the accretion rates to give rise to the observed amplitudes of the short-timescale (stochastic) variability (for

example, [18] gives $\dot{M} \approx 10^{-8}$–$10^{-7} M_\odot$/yr). Grinin [1] has suggested that, in this case also, the main source of variability remains variable circumstellar extinction; strong brightness dips are due to large gas–dust formations, while the short-timescale variability is associated with small inhomogeneities in the absorbing medium. As the orientation of the star–disk system changes, the amount of gas along the line of sight will decrease, but its influence on the brightness will remain fairly strong. In this model, the small changes of the color-index slopes relative to the reddening line in Fig. 2 can be explained as the result of differences in the mean sizes of the absorbing dust grains near different stars [19].

Let us now attempt to estimate the accretion rate needed to bring about the observed brightness variability ($\approx 0^m.1$–$0^m.2$ in V). We will consider V1331 Cyg, using the following parameters determined by Chavarria [20]: Sp = F0, $R_* \approx 5R_\odot$, $M_* \approx 3M_\odot$, $L \approx 90L_\odot$, $T \approx 7400K$, $A_V \approx 2^m.4$, and $r \approx 700$ pc. Let us suppose that, during brightness minima, we observe only radiation from the star, and that the excess radiation observed during brightness maxima is completely due to accretion. We adopted the mean values for two subsequent dates, JD 2448427 and JD 2448428, for the low state ($U = 13.70$, $B = 13.19$, $V = 12.10$, $R = 11.04$)), and the values for JD 2448509 for the high state ($U = 13.40$, $B = 12.91$, $V = 11.86$, $R = 10.83$). After converting the *UBVR* magnitudes at the minimum and maximum brightnesses into radiation fluxes, E_V (erg cm^{-2} s^{-1} Å^{-1}), and taking interstellar absorption into account, we obtained optical spectral energy distribution (SED) curves for the star's minimum and maximum states. Both curves grow appreciably towards the UV. Subtracting the first from the second curve, we obtain the curve of the radiation flux change, which also rises toward short wavelengths. The optical flux corresponding to this last curve is $\approx 25\%$ of the flux generated by the star itself (i.e., the flux at minimum brightness), but the slope of the residual SED curve is less steep in the UV than the SED curve for the star. This means that the total flux due to accretion is less than 10 percent of the star's luminosity. Using the known luminosity of the star and the formula $\Delta L = \dot{M}\frac{GM_*}{2R_*}$, we can estimate the accretion rates in units of $M_\odot$/yr. This yields $\dot{M} \simeq 10^{-7}\ M_\odot$/yr, a fairly realistic value.

Confirmation of one or the other of these possibilities requires a more detailed photometric and spectroscopic study of Herbig Ae/Be stars with known orientations relative to the line of sight; in particular, it is necessary to determine whether these stars show correlations between the parameters of spectral lines emitted by hot gas and the character of their short-timescale variability.

ACKNOWLEDGMENTS

The author wishes to thank the members of his department K.N. Grankin, O.V. Ezhkova, and M.A. Ibragimov for taking part in the observations. Thanks are also due to S.A. Lamzin for discussions of this study. The author is deeply grateful to the late V.S. Shevchenko for supervising investigations in this field over many years.

REFERENCES

1. V. P. Grinin, N. N. Kiselev, N. Kh. Minikulov, *et al.*, Astrophys. Space Sci. **186**, 283 (1991).
2. V. S. Shevchenko, *Herbig Ae/Be Stars* [in Russian] (FAN, Tashkent, 1989).
3. V. S. Shevchenko, K. N. Grankin, M. A. Ibragimov, *et al.*, Astrophys. Space Sci. **202**, 137 (1993).
4. L. A. Hillenbrand, S. E. Strom, F. J. Vrba, and J. Keene, Astrophys. J. **397**, 613 (1992).
5. V. P. Grinin and O. V. Kozlova, Astrofizika **43**, 329 (2000).
6. G. V. Zaĭtseva and V. M. Lyutyĭ, Pis'ma Astron. Zh. **23**, 277 (1997) [Astron. Lett. **23**, 242 (1997)].
7. V. P. Grinin, N. N. Kiselev, N. Kh. Minikulov, and G. P. Chernova, Pis'ma Astron. Zh. **14**, 514 (1988) [Sov. Astron. Lett. **14**, 219 (1988)].
8. G. V. Abramyan, S. V. Zaratsyan, N. D. Melikyan, *et al.*, Astrofizika **32**, 39 (1990).
9. V. P. Grinin and A. N. Rostopchina, Astron. Zh. **73**, 194 (1996) [Astron. Rep. **40**, 171 (1996)].
10. W. Herbst and V. S. Shevchenko, Astron. J. **118**, 1043 (1999).
11. S. Yu. Mel'nikov, Perem. Zvezdy **23**, 117 (1993).
12. S. Yu. Mel'nikov and O. V. Ezhkova, Pis'ma Astron. Zh. **26**, 282 (2000) [Astron. Lett. **26**, 233 (2000)].
13. M. Cohen and L. V. Kuhi, Astrophys. J., Suppl. Ser. **41**, 743 (1979).
14. P. S. Thé, in *The Nature and Evolutionary Status of Herbig Ae/Be Stars*, Eds. P. S. Thé, M. R. Perez, and E. P. J. van den Heuvel, Astron. Soc. Pac. Conf. Ser. **62**, 23 (1994).
15. S. McMuldroch, A. I. Sargent, and A. B. Geoffrey, Astron. J. **106**, 2477 (1993).
16. P. Bastien and F. Menard, *The Nature and Evolutionary Status of Herbig Ae/Be Stars*, Ed. by P. S. Thé, M. R. Perez, and E. P. J. van den Heuvel, Astron. Soc. Pac. Conf. Ser. **62**, 71 (1994).
17. P. F. C. Blondel and H. R. E. Tjin a Djie, in *The Nature and Evolutionary Status of Herbig Ae/Be Stars*, Ed. by P. S. Thé, M. R. Perez, and E. P. J. van den Heuvel, Astron. Soc. Pac. Conf. Ser. **62**, 211 (1994).
18. L. V. Tambovtseva, V. P. Grinin, and O. V. Kozlova, Astrofizika **42**, 75 (1999).
19. A. N. Rostopchina, V. P. Grinin, A. Okazaki, *et al.*, Astron. Astrophys. **327**, 145 (1997).
20. C. Chavarria, Astron. Astrophys. **105**, 105 (1981).

Translated by N. Samus'

Astronomy Reports, Vol. 45, No. 9, 2001, pp. 692–699. Translated from Astronomicheskiĭ Zhurnal, Vol. 78, No. 9, 2001, pp. 798–806.

Models for Highly Flattened, Rapidly Rotating Cool Stars in a Newtonian Approximation

D. P. Savokhin[1], E. I. Saritsin[1], and S. I. Blinnikov[2]

[1]*Urals State University, Astronomical Observatory, pr. Lenina 51, Yekaterinburg, 620083 Russia*

[2]*Institute of Theoretical and Experimental Physics, Bol'shaya Cheremushkinskaya ul. 25, Moscow, 117259 Russia*

Received December 17, 2000

Abstract—We investigate the physical characteristics of single, rapidly rotating white dwarfs, which could form as a result of a merger of two white dwarfs with different masses and filled Roche lobes, due to the radiation of gravitational waves. When the merging of the binary components occurs without loss of mass and angular momentum, the merger products are subject to secular instability, and the density in their cores does not exceed ~10^8 g/cm^3. Models are constructed for rapidly rotating neutron stars, which could form after the collapse of rotating iron cores of evolved massive stars. Dynamically unstable neutron-star models are characterized by a shift of the maximum density from the rotational axis. The total momentum of such neutron stars is about half the maximum possible momentum for the evolved cores of massive stars. © *2001 MAIK "Nauka/Interperiodica".*

1. INTRODUCTION

Modern theories for supernova explosions of all types and for gamma-ray bursts compel studies of very rapidly rotating degenerate stars. For example, one of the most probable mechanisms for the formation of the precursors of type I supernovae is the approach of two white dwarfs in a close binary system as a consequence of gravitational radiation, with the subsequent disruption of the less massive component due to the filling of its Roche lobe and the associated mass loss [1–3]. This could lead to the formation of a massive disk around the more massive component, or of a single rapidly rotating white dwarf.

Explosions of type II supernovae cannot be accounted for in a spherically symmetrical treatment, and this problem requires inclusion of a natural property of stars—their rotation [4]. The idea of relating supernovae to the instability of rapidly rotating collapsing stars against fragmentation was expressed very early by Weizsacker [5]. Skhlovsky [6] also suggested the possible importance of rotational instability for type II supernovae. These ideas were initially expressed only in a very general form, and it was much later that Imshennik [7] developed a detailed scenario in which such instability played a very important role. The collapse of the rapidly rotating, central part of a massive star can be accompanied by the formation of a system of two neutron stars. The approach of the components of this binary system as a consequence of gravitational radiation can rapidly lead to a flow of matter from and explosion of the less massive neutron star, for example, via the mechanism described in [8]. This explosion can result in overall asymmetry of the supernova explosion and bring about strong mixing.

The merging of neutron stars is one of the most plausible models for gamma-ray bursts [8]. The magnetorotational mechanism for supernova explosions [9, 10] also requires rapidly rotating configurations. Dynamical computations of such explosions must begin with the construction of stationary, rapidly rotating configurations, which is already a non-trivial task [11, 12]. The current paper represents one step along this path. We have constructed models for stationary, rapidly rotating configurations for a single-parameter family of rotation laws, such that, for one extreme value of this parameter, the rotation of the star is close to rigid with Ω = const, while, for its other extreme value, the star rotates with nearly constant linear speed v = const, where Ω and v are the angular and linear speeds of the rotation, respectively. This family of rotation laws enables us to trace the relation between the star's internal distribution of angular momentum and its integrated characteristics. The analysis assumes Newtonian gravitation, which is a good approximation for white dwarfs. Treatment of neutron stars requires general relativistic corrections, and our analysis is only a zeroth-order approximation to the series of post-Newtonian corrections, representing a necessary step toward exact account of relativistic gravitation [13, 14]. However, for very rapidly rotating neutron stars, even this zeroth-order approximation is not poor, if the mass is concentrated at large distances from the center; i.e., if the star's equatorial radius is much larger than the Schwartzschild radius.

Thus, the aim of the current study is to construct stationary models for very rapidly differentially rotating degenerate stars, including models in the domain of dynamical-instability losses, for further application in dynamical computations associated with supernova explosions.

1063-7729/01/4509-0692$21.00 © 2001 MAIK "Nauka/Interperiodica"

2. FORMULATION OF THE PROBLEM

Let us consider an axially symmetric stellar configuration in a state of stationary rotation. The equation of motion of a volume element has the form

$$\rho(\mathbf{v}\nabla)\mathbf{v} + \nabla P + \rho\nabla\Phi = 0,$$

where ρ is the density of the matter, Φ is the gravitational potential, which satisfies the Poisson equation

$$\nabla^2\Phi = 4\pi G\rho, \quad (1)$$

and P is the pressure of the matter, which is related to the density by the barotropic equation of state

$$P = P(\rho).$$

In the case of a barotropic equation of state, the surfaces of constant pressure and of constant density coincide, and the angular velocity of rotation $\Omega(\bar{\omega})$ depends solely on the distance $\bar{\omega}$ from the rotational axis; i.e., it is constant along cylinders coaxial with the rotational axis [15]. Thus, the linear speed of an element is related to its angular speed by the expression

$$\mathbf{v} = \bar{\omega}\Omega(\bar{\omega})\mathbf{e}_\varphi,$$

where $\mathbf{e}_\varphi$ is a unit vector in the direction of the azimuthal angle φ.

Integrating the equation of motion, we can obtain the Bernoulli integral

$$H(\rho) + \Phi + \Psi(\bar{\omega}) = C, \quad (2)$$

where C is the constant of integration; $H(\rho)$ is the enthalphy, which is defined by the expression

$$H(\rho) = \int dP(\rho)/\rho;$$

and $\Psi(\bar{\omega})$ is the centrifugal potential, which is related to the angular speed by the expression

$$\Psi(\bar{\omega}) = -\int \Omega^2(\bar{\omega})\bar{\omega}d\bar{\omega}.$$

We adopted the rotation law

$$\Psi(\bar{\omega}) = -C_\psi \ln(\bar{\omega}^2 + d^2)/2, \quad (3)$$

where d is a parameter. In the limit $d \longrightarrow 0$, the linear speed of rotation is constant inside the star, and the rotation approaches that of a solid body as d increases. We constructed a series of models for the case of rigid rotation,

$$\Psi(\bar{\omega}) = -C_\psi\bar{\omega}^2/2.$$

If we use the Bernoulli integral (2) to express the density as a function inverse to the enthalpy and substitute this into the Poisson equation (1), we obtain an equation containing the gravitational potential Φ and the constants C and C_ψ. This equation is then written in finite differences on a two-dimensional grid (r, θ), with the radial coordinate of the grid outside the star being a quantity inversely proportional to the distance [16]; r is the distance from the center of the configuration and θ is the polar angle measured from the rotational axis. The boundary conditions are symmetry at the center and the condition $\Phi = 0$ as $r \longrightarrow \infty$. Specifying in addition the ratio of the polar and equatorial radii $\varepsilon = R_p/R_e$ and the maximum density enables determination of C and C_ψ simultaneously with the field Φ [11]. The density at each grid node can be found using (2). The position of the node at which the maximum density is reached is found during the computation process.

Due to our use of the differential relation (1) between the gravitational potential and the density, the matrix of coefficients for the system of difference equations is sparse; i.e., it has many zero elements. We solved the system of difference equations using the method for solving systems of equations with sparse matrices described in [17], realized in the applied package SPARSE [18].

The accuracy of the computations is monitored with the virial test [19]

$$VT = |2T + W + 3\Pi|/|W|,$$

where T is the kinetic rotational energy of the star, W is the star's gravitational energy, and the quantity Π is defined by the expression

$$\Pi = \int P d\mathbf{r},$$

where $d\mathbf{r}$ is a volume element. For all the computed models, $VT < 10^{-3}$.

3. WHITE DWARF MODELS

We constructed white-dwarf models for the case of an ideal electron gas, for which the equation of state is given by the parametric relation between the pressure and density [20]

$$\begin{cases} P(x) = a\{x(1+x^2)^{1/2}(2x^2/3 - 1) \\ \quad + \ln(x + (1+x^2)^{1/2})\}/8\pi^2 \\ \rho(x) = bx^3, \end{cases}$$

$$a = m_e c^2/\lambda_e^3, \quad b = m_{\mathrm{H}}/(3\pi^2\lambda_e^3 Y_e), \quad x = p_{\mathrm{F}}/(m_e c),$$

where m_e and m_{H} are the electron mass and unit atomic mass, respectively, λ_e the Compton wavelength of the electron, c the velocity of light, p_{F} the Fermi momentum of the degenerate electron gas, and Y_e the molecular weight of the gas.

Figure 1 shows the mass of the white dwarf as a function of the ratio ε for several fixed values of the maximum density $\rho_{\max}$. When rotation is taken into account, the mass of the white dwarf becomes larger than in a non-rotating model with the same maximum density. In the case of rigid rotation, the white-dwarf mass can grow by no more than 5%. When the ratio ε is decreased below 0.67, the effective acceleration (sum of the gravitational and centrifugal accelerations) at the equator vanishes. This behavior is in full agreement with previous computations [21], and is due to the fact

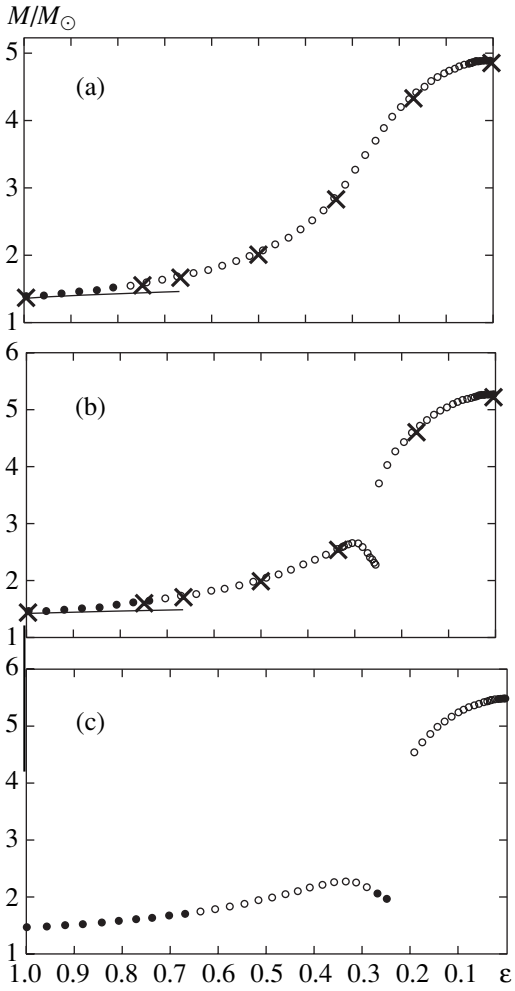

Fig. 1. Mass of the white dwarf as a function of the ratio ε of the polar to the equatorial radii for maximum densities (a) 10^9, (b) 10^{10}, and (c) 10^{11} g/cm^3. The solid curve shows the case of rigid rotation and the circles the case of rotation in accordance with the law (3) for $d = 0.1$. The maximum density is reached either on the rotational axis (filled circles) or displaced from it (hollow circles). The crosses show the results of [21] for the rotation law (3) with $d = 0.1$.

that, in the case of rigid rotation, a substantial fraction of the momentum is concentrated in surface, near-equatorial layers of the star [15]. In the case of differential rotation (3), in contrast, an appreciable fraction of the momentum is contained in inner layers of the star. For this reason, the mass of a differentially rotating white dwarf can significantly exceed the mass for the corresponding non-rotating model, and there is no flow of matter from the equator, even for very flattened models. For example, when $d = 0.1$ and $\log\rho_{max} = 9$, the mass for the model white dwarfs grows monotonically to $4.87M_\odot$ as ε is decreased to zero (Fig. 1). However, at large maximum densities, the elastic properties of the matter change, and this is reflected in the integrated characteristics of model white dwarfs rotating in accordance with (3). When $\log\rho_{max} = 10$, the changes in the mass become nonmonotonic, and there is a break near $\varepsilon = 0.23$. When $\log\rho_{max} = 11$, it is possible to construct models of stationary rotating white dwarfs only in the intervals $0 \le \varepsilon \le 0.194$ and $0.250 \le \varepsilon \le 1$, and, when $\varepsilon = 0.250$ and $\varepsilon = 0.194$, the effective acceleration at the equator vanishes.

The decrease in the elasticity of the matter with growth in the density that occurs for the equation of state of an ideal electron gas can be considered analogous to an increase in the polytropic index *n*. It was shown in [21] that models of polytropes rotating in accordance with (3) and with $d = 0.1$ can exist over the whole range of variation of ε for $n = 0$ and $n = 3/2$. When $n = 3$, there appears an interval of ε in which there are no stationary models, with models with zero effective equatorial acceleration at the boundaries of this interval. The integral equation

$$\Phi(\mathbf{r}) = \int \frac{\rho(\mathbf{r}')d\mathbf{r}'}{|\mathbf{r} - \mathbf{r}'|}$$

was used in [21] to determine the gravitational potentials for rapidly rotating model white dwarfs. The white-dwarf models obtained in [21] for the rotation law (3) with $d = 0.1$ are also shown in Fig. 1. The intervals for which stationary white-dwarf models can be constructed appear for $\log\rho_{max} = 10.5$ and $\log\rho_{max} = 11$. Thus, when $d = 0.1$ and $\log\rho_{max} \le 9$, it is possible to construct models with differential rotation in accordance with (3) of white dwarfs with any degree of flattening.

The precursors of type I supernovae in elliptical galaxies form as a result of the evolution of close binary systems with moderate masses [1, 2]. In the last stages of the evolution of such close binaries, the two white dwarfs approach due to the radiation of gravitational waves, and the less massive of the two fills its Roche lobe. Further, the evolution of this component proceeds on the dynamical time scale. This evolution can lead to the formation of a single object whose mass exceeds the Chandrasekhar limit, or of a single star surrounded by a massive torus. If the masses of the two components are the same, the total momentum of the binary system is less than that required to support a torus in equilibrium [22]. Thus, if the component masses are equal, we can rule out the formation of a torus, and we expect the formation of a single massive object.

Assuming that the disruption of the binary system is conservative (i.e., the total mass and momentum of the system are conserved) and results in the formation of a rapidly rotating white dwarf, we can estimate its characteristics. The total energy of a white dwarf whose mass and momentum are similar to those of a binary at the stage of Roche-lobe filling is only slightly lower than the total energy of the binary if the white-dwarf rotation law is given by (3) and $d = 0.1$. In the case of rigid rotation, the maximum momentum of the white

dwarf is much lower than that of a binary system with the same mass. Consequently, the formation of rigidly rotating white dwarfs during the conservative disruption of a binary is not possible. The formation of a differentially rotating white dwarf with the same integrated characteristics as the corresponding binary system at the stage of Roche-lobe filling and lower total energy is possible, even if two components with the Chandrasekhar mass merge.

Since the momentum of the merger products is the same as that of the binary system, the model white dwarfs are highly flattened. The semi-axis ratio grows from $\varepsilon = 0.23$ for a model with a mass of $1M_\odot$ to $\varepsilon = 0.33$ for a model with a mass of $2.8M_\odot$. The ratio of the rotational kinetic energy to the absolute value of the gravitational energy in these cases is $\beta \approx 0.18$–0.20. Thus, axially symmetric models for the merger products are subject to secular instability [15]. In this case, the maximum density in the models changes from 7.6×10^5 to 1.9×10^8 g/cm^3 for the same mass range. The densities in the products of binary white-dwarf mergers are insufficient to support carbon-burning piconuclear reactions. This is a direct consequence of our assumption that momentum is conserved during the disruption of the binary system. The characteristics of the products of a binary white-dwarf merger when the disruption of the binary is not conservative, with loss of mass and momentum during the common-envelope stage, are considered in [22]. However, in this case, the remaining momentum is sufficiently high that the densities in most of the merger products with masses higher than the Chandrasekhar mass remain insufficient to sustain piconuclear reactions. Only in systems with total masses exceeding $2.4M_\odot$ can a white dwarf form with a mass of $\sim 1.7M_\odot$ and a density sufficiently high to sustain explosive nuclear burning in the degenerate matter.

Thus, in most cases, the merger of binary degenerate dwarfs with equal masses probably result in single, highly flattened, differentially rotating white dwarfs with masses exceeding the Chandrasekhar limit and densities below $\sim 10^8$ g/cm^3. The density may increase during the subsequent evolution of the star, in connection with the transport of momentum from the inner regions of the star, possibly accompanied by a loss of excess momentum and matter from the equatorial region.

4. NEUTRON STAR MODELS

When computing the neutron-star models, we adopted an equation of state that was an optimal "joining" of the equations of Feynman, Metropolis, and Teller [23] for $\rho < 10^4$ g/cm^3, Baym, Pethick, and Sutherland [24] for $10^4 < \rho < 4.3 \times 10^{11}$ g/cm^3, and Baym, Bethe, and Pethick [25] for $4.3 \times 10^{11} < \rho < 2.2 \times 10^{14}$ g/cm^3. We used Table 12 from the review [26] for nuclear densities $2.2 \times 10^{14} < \rho < 10^{15}$ g/cm^3. In intervals between pairs of values (P_i, ρ_i), we adopted the polytropic dependence $P = K\rho^\Gamma$, using the parameters K and Γ determined from the values (P_i, ρ_i) at the edges of the intervals [12, 27].

Type II supernovae are associated with the collapse of the evolved cores of massive stars and the formation of neutron stars. When rotation is taken into account, the core collapse may occur in two stages [4, 7, 28]. In the first stage, the iron core of an evolved massive star collapses, with the formation of a (proto)neutron star. The kinetic energy of the rigidly rotating iron core comprises only a few percent of the absolute value of the gravitational energy. If the core momentum is conserved during the collapse, the fraction of the rotational kinetic energy relative to the gravitational energy grows. As a result, the highly flattened, differentially rotating, dynamically unstable (proto)neutron star that forms at this stage is characterized by a maximum density of $\sim 3 \times 10^{14}$ g/cm^3, and rotation plays the leading role in supporting its equilibrium [28]. In the second stage, after the stage of neutrino cooling, dynamical instability can lead to fragmentation of the cool, rapidly rotating (proto)neutron star, with the formation of a close neutron-star binary system [7].

Let us consider the construction of dynamically unstable models for cool neutron stars rotating in accordance with (3). In dynamically unstable models, the rotational kinetic energy exceeds 27% of the absolute value of the gravitational energy [15]. The kinetic energy and other integrated characteristics of the neutron star are determined by both the absolute value of the momentum and its distribution in the stellar matter. For example, increasing the parameter d in the rotation law (3) leads to a growth in the ratio β of the model kinetic energy to the absolute value of the gravitational energy. However, when d is increased, the rotation of the star approaches that of a solid body. A substantial fraction of the momentum is concentrated in a surface, near-equatorial layer of the star. As a result, as d approaches some critical value, the effective acceleration at the equator tends to zero. The critical value of d is determined by the maximum density for the model and the ratio ε (Fig. 2). For neutron stars with masses typical of the iron cores of evolved massive stars, a range of values for d corresponding to dynamically unstable models ($\beta \geq 0.27$) appears only for rather highly flattened models. For example, model neutron stars with masses of 1.4–$2.0M_\odot$ are dynamically unstable for $0.40 \leq d \leq 0.45$ if $\varepsilon = 0.20$, and for $0.35 \leq d \leq 0.62$ if $\varepsilon = 0$ (Fig. 2). The largest range of semi-axis ratios $0 < \varepsilon < 0.20$ for dynamically unstable models is achieved when $d \approx 0.41$. As d is increased, the upper boundary for this range approaches zero. The maximum value of d for which it is still possible to construct a neutron-star model with a mass not exceeding $2M_\odot$ is close to 0.62. When $d \leq 0.35$, all model neutron stars with masses 1.4–$2.0M_\odot$ are dynamically unstable.

Stationary models for differentially rotating neutron stars with $d = 0.41$ can be constructed for any ratio of

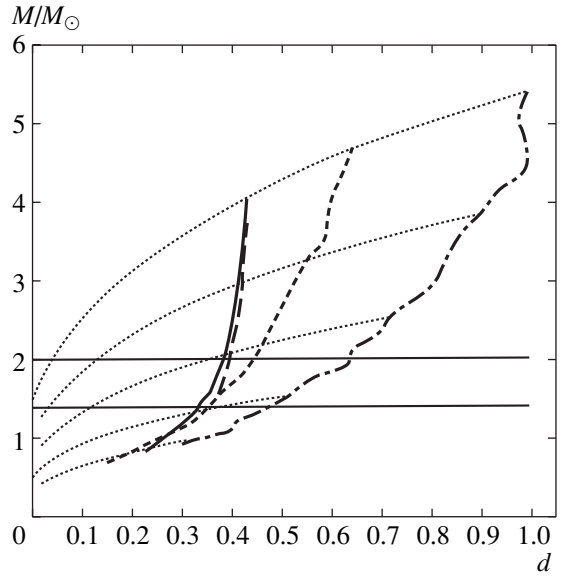

Fig. 2. Mass of the neutron star as a function of the parameter d in the rotation law (3). The dotted curves show models for five maximum densities (from top to bottom): $\rho_{max}/10^{14}$ g/cm^3 = {3, 4, 5, 6, 7}. For all models, the semi-axis ratio is $\varepsilon = 0.0004$. Models for which $\beta = 0.27$ are shown by the solid curve for $\varepsilon = 0.0004$ and the long-dashed curve for $\varepsilon = 0.1936$. Models that are close to a configuration with outflow from the equator are shown by the dot–dash curve for $\varepsilon = 0.0004$ and the short-dashed curve for $\varepsilon = 0.1936$. We also present curves for $M = 2M_\odot$ and $M = 1.4M_\odot$.

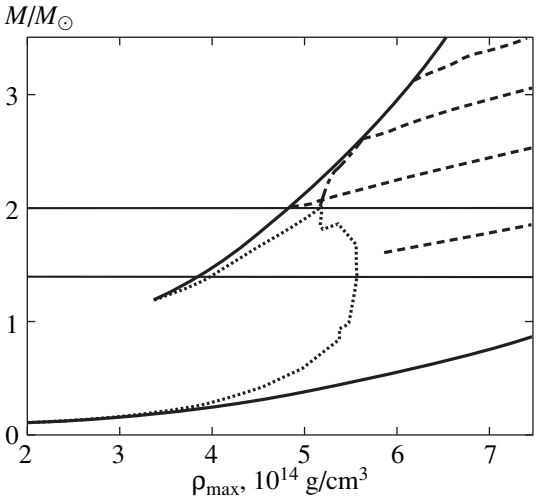

Fig. 3. Mass of the neutron star as a function of the maximum density for $d = 0.41$ and various values of ε. The solid curves show models with $\varepsilon = 1$ (lower) and $\varepsilon = 0.0004$ (upper), the dashed curves show curves of constant angular momentum $J/10^{49}$ g cm^2 s^{-1} = {2, 4, 6, 8} (curves for higher values of J are lower), and the dot–dash curve corresponds to the constant value $\beta = 0.27$. The position of models with zero effective acceleration at the equator is roughly indicated by the dotted curve.

the polar and equatorial radii if the maximum density in the models exceeds 5.57×10^{14} g/cm^3. The mass of the neutron star grows monotonically as ε decreases from one to zero for a fixed value of the maximum density (Fig. 3), as occurs for white dwarfs with relatively modest densities (Fig. 1a). When $\rho_{max} = 5.57 \times 10^{14}$ g/cm^3, the variation of the mass with ε becomes nonmonotonic. If the maximum density is lower than 5.57×10^{14} g/cm^3, stationary neutron-star models can be constructed only for small and large values of ε; there are no stationary models with intermediate values of ε. With the use of our equation of state, a decrease in the density can be considered analogous to a corresponding increase in the polytropic index n. As in the white-dwarf case, an interval of ε for which there are no stationary solutions appears as the polytropic index is increased. Model computations carried out on a specially chosen grid nonuniform in r show a decrease in the absolute value of the effective acceleration at the equator as ε approaches the boundaries of regions in which stationary solutions exist. The sharp decrease in the effective acceleration with increase in ε in the right branches of the dependences in Fig. 4 for $\rho_{max}/10^{14}$ g/cm^3 = {4, 5} requires the introduction of still finer grids in the regions of compression $\varepsilon = 0.18$ and $\varepsilon = 0.23$. Consequently, as in the white-dwarf case, models with zero effective acceleration at the equator are found at boundaries of intervals of ε in which there are no stationary solutions. With a constant maximum density $\rho_{max} < 5.57 \times 10^{14}$ g/cm^3 and $d = 0.41$, the model masses first grow as ε is decreased from unity, then decrease slightly until the effective acceleration at the equator becomes zero. When $\varepsilon < 0.23$, the model masses grow as ε is decreased. Qualitatively, the variation of the masses for model neutron stars as ε is decreased with a fixed maximum density $\rho_{max} < 5.57 \times 10^{14}$ g/cm^3 is the same as that for model white dwarfs with $\rho_{max} = 10^{11}$ g/cm^3 (Fig. 1c). In a diagram plotting mass versus maximum density, the highly flattened, dynamically unstable neutron-star models with $d = 0.41$ are located in the region delineated by the values $\varepsilon = 0.0004$, $\beta = 0.27$ and by the line corresponding to models with zero effective acceleration at the equator (Fig. 3). The densities in these models do not exceed 5.5×10^{14} g/cm^3.

When $d = 0.62$, intervals of ε for which it is not possible to construct stationary models of neutron stars rotating in accordance with (3) appear when the maximum density is lower than 8.4×10^{14} g/cm^3. In this case, the ratio of the polar to the equatorial radii for dynamically unstable neutron-star models is zero for a wide range of maximum densities $4.5 < \rho_{max}/10^{14}$ g/cm$^3 < 6.5$. However, only when $\rho_{max} \approx 4.5 \times 10^{14}$ g/cm^3 is the mass of the neutron star similar to those of the evolved cores of massive stars.

Thus, dynamically unstable neutron-star models are characterized by a high degree of flattening and relatively modest densities (Fig. 3). This latter circumstance is prob-

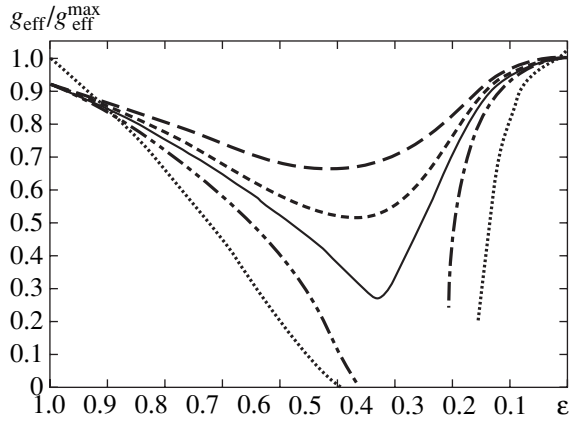

Fig. 4. Ratio of the effective acceleration at the equator to the maximum value in a series of computations with constant maximum density as a function of the semi-axis ratio ε for $d = 0.41$. The maximum densities $\rho_{\rm max}/10^{14}$ g/cm^3 were 7 (long-dashed curve), 6 (short-dashed curve), 5.57 (solid curve), 5 (dot–dash curve), and 4 (dotted curve).

ably associated with a decrease in the elasticity of the matter as the density decreases. In this case, the role of the centrifugal force in counteracting the gravitational force to support the star in an equilibrium state grows compared to that of the pressure. Accordingly, the fraction of the kinetic energy increases relative to the gravitational energy. The characteristics of some dynamically unstable models for neutron stars with a mass of $2M_\odot$ are presented in the table, and the density distribution in these models is shown in Fig. 5. The maximum density in the dynamically unstable neutron-star models we have obtained is reached in the equatorial plane on the side that is furthest from the rotational axis.

The ratio of the gravitational to the centrifugal acceleration in the equatorial plane changes sign as we move from the center toward the surface (Fig. 6), since the minimum in the gravitational potential is shifted from the rotational axis and is located on a circumference G between the center of the configuration C and the circumference O where the density reaches its max-

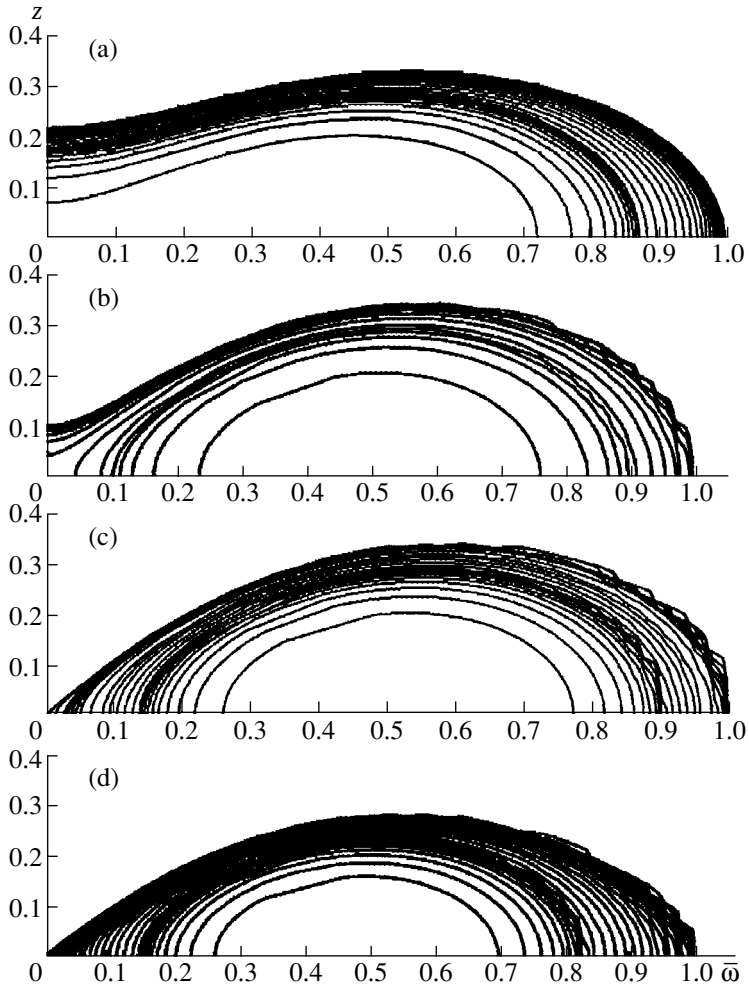

Fig. 5. Density distribution in the meridional plane for models (a) A, (b) B, (c) C, and (d) D. The densities of neighboring equal-density contours differ by a factor of two. The characteristics of the models are presented in the table.

Characteristics of dynamically unstable neutron-star models

Model	d	ε	ρ_{max}, 10^{14} g/cm^3	ϖ_{max}	M, $M_\odot$	R_e, 10^6 cm	J, 10^{49} g cm^2/s	β, %
A	0.41	0.221	5.15	0.42	1.98	2.48	3.70	27.0
B	0.41	0.102	4.90	0.50	1.97	2.49	3.97	27.2
C	0.41	0.0004	4.90	0.52	2.02	2.51	4.21	27.3
D	0.62	0.0004	4.50	0.48	2.01	2.99	4.61	29.0

The columns present the model notation; value of d in the rotation law (3); ε, the ratio of the polar to the equatorial radii; ρ_{max}, the maximum density and ϖ_{max}, the distance in the equatorial plane (in fractions of the equatorial radius) from the rotational axis to the point with the maximum density; M, the model mass; R_e, the equatorial radius; J, the total angular momentum; and β, the ratio of the kinetic energy to the absolute value of the gravitational energy.

imum. Near the equatorial plane between C and G, the joint action of the centrifugal and gravitational forces balances the pressure gradient. In the region between G and O, the centrifugal force balances the gravitational force and the pressure. In the region between O and the surface, the pressure and the centrifugal force balance the gravitational force. Only in this last region does the gravitational acceleration exceed the centrifugal acceleration. In the first two regions, the gravitational acceleration can act in the same direction as the centrifugal force or the pressure gradient, and be weaker than the centrifugal acceleration. The motion of matter in these regions depends appreciably on the pressure gradient. At a fixed value of d, the ratio of the gravitational to the centrifugal acceleration at the equator approaches –1 as ε is increased (models C and A, Fig. 6).

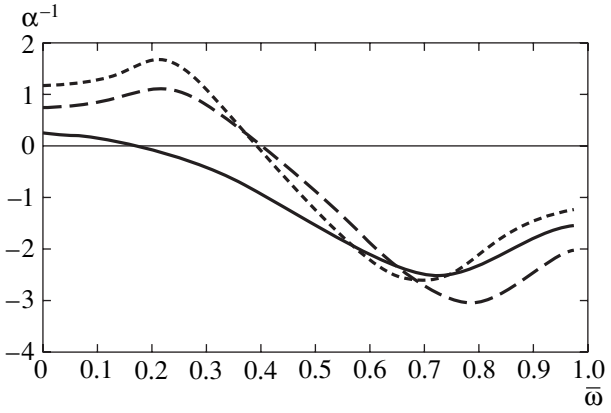

Fig. 6. Ratio of the gravitational to the centrifugal acceleration as a function of relative distance from the rotational axis for models A (solid curve), C (long-dashed curve), and D (short-dashed curve).

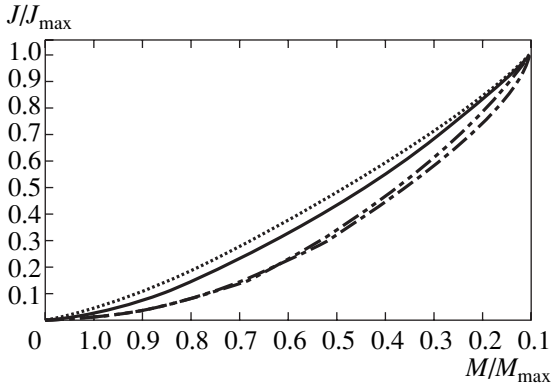

Fig. 7. Fraction of the momentum as a function of the relative mass contained in a cylinder of radius $\bar{\omega}$. The solid curve shows model A, the dotted curve model B, and the dot–dashed curves with single and double dots models 1 and 2 rotating in accordance with the law α = const from [12].

The relative drop of the angular velocity between the center and equator in the dynamically unstable neutron-star models is determined by d. The central region rotates at approximately twice the speed of the region near the equator. The linear speed grows with distance from the rotational axis. The central regions of models in which the density increases with distance from the rotational axis rotate nearly rigidly.

Our dynamically unstable models rotating in accordance with (3) differ from the models obtained in [12] rotating with α = const, where α is the ratio of the centrifugal to the gravitational acceleration, in their larger concentration of the angular momentum toward the rotational axis (Fig. 7). For this reason, the maximum density in the models rotating in accordance with (3) is shifted from the rotational axis. At the same time, the total momentum in these models (see the table) is roughly half the maximum momentum allowed for rigidly rotating cores of evolved massive stars [28].

5. CONCLUSION

The merging of binary white dwarfs with equal masses can give rise to highly flattened ($0.23 \le \varepsilon \le 0.33$), single, rapidly rotating white dwarfs whose masses exceed the Chandrasekhar limit by a factor of two, if the mass and momentum are conserved during the merger of the binary components. For this reason, rotation plays an important role in supporting the equilibrium of the products of such binary mergers. The ratio of the rotational kinetic energy to the absolute value of the gravitational energy in the merger products reaches 20%. Thus, axially symmetric products of white-dwarf mergers are subject to secular instability [15].

The densities in such rapidly rotating white dwarfs are insufficient to support carbon burning in the degenerate matter, in spite of the fact that their mass can exceed the Chandrasekhar limit by a factor of two. The further evolution of the merger products may be associated with the transport of momentum from inner to outer parts of the star, possibly with a subsequent loss of momentum and mass from the equatorial region. We cannot rule out the formation of a triaxial figure of equilibrium as a result of the merger of two white dwarfs of equal mass. Study of the characteristics of such triaxial figures requires three-dimensional computations. We will investigate the possibility of forming a torus around the more massive component in a binary system with white dwarfs with different masses in a separate paper.

Our dynamically unstable models for cool neutron stars rotating in accordance with (3) are characterized by densities at which the elasticity is relatively modest and by a high degree of flattening ($0 \le \varepsilon \le 0.20$); this was also found for equilibrium configurations obtained in numerical simulations of the collapse of a rotating iron core [28] and for models of neutron stars in which the ratio of the centrifugal and gravitational accelerations in the equatorial plane is constant [12]. In contrast to these last models, our dynamically unstable neutron-star models show a higher concentration of momentum toward the rotational axis and, as a consequence, a shift of the maximum density away from the rotational axis. At the same time, the total momentum in our models is about half the maximum possible momentum for rigidly rotating iron cores of evolved massive stars. This suggests that rotation does not play an important role in the initial stages of collapse. The ratio of the rotational kinetic energy to the absolute value of the gravitational energy in our model rapidly rotating neutron stars can be considered to result from the first collapse of an iron core of an evolved massive star [4]; the values we have obtained are in the interval 0.27–0.29, near the boundary of dynamical instability. Since the maximum density in such dynamically unstable neutron stars is displaced from the rotational axis, fragmentation could lead to the formation of systems of two or more neutron stars.

In conclusion, we note that the relatively simple two-dimensional computations for stationary models of rapidly rotating cool stars considered here were intended only to identify likely characteristics of the products of white-dwarf mergers, and do not eliminate the need to conduct more complex, three-dimensional dynamical computations.

ACKNOWLEDGMENTS

This study was supported by the Russian Foundation for Basic Research (project no. 99-02-16205).

REFERENCES

1. A. G. Masevich and A. V. Tutukov, *Stellar Evolution: Theory and Observations* [in Russian] (Nauka, Moscow, 1988).
2. I. Iben and A. V. Tutukov, Astrophys. J., Suppl. Ser. **54**, 335 (1984).
3. L. R. Yungelson, M. Livio, A. V. Tutukov, and R. A. Saffer, Astrophys. J. **420**, 336 (1994).
4. V. S. Imshennik, in *Eruptive Stars*, Ed. by A. G. Masevich [in Russian] (Moscow, 1996), p. 7.
5. C. F. Weizsäcker, Z. Astrophys. **24**, 181 (1947).
6. I. S. Shklovsky, Astrophys. J. Lett. **8**, L101 (1970).
7. V. S. Imshennik, Pis'ma Astron. Zh. **18**, 489 (1992) [Sov. Astron. Lett. **18**, 194 (1992)].
8. S. I. Blinnikov, I. D. Novikov, T. V. Perevodchikova, and A. G. Polnarev, Pis'ma Astron. Zh. **10**, 422 (1984) [Sov. Astron. Lett. **10**, 177 (1984)].
9. G. S. Bisnovatyĭ-Kogan, Astron. Zh. **47**, 813 (1970) [Sov. Astron. **14**, 652 (1971)].
10. N. V. Ardeljan, G. S. Bisnovatyĭ-Kogan, and S. G. Moiseenko, Astrophys. Space Sci. **239**, 1 (1996).
11. A. G. Aksenov and S. I. Blinnikov, Astron. Astrophys. **290**, 674 (1994).
12. A. G. Aksenov, S. I. Blinnikov, and V. S. Imshennik, Astron. Zh. **72**, 717 (1995) [Astron. Rep. **39**, 638 (1995)].
13. S. Bonazzola, E. Gorgoulhon, M. Salgado, and J. A. Marck, Astron. Astrophys. **278**, 421 (1993).
14. P. Haensel, M. Salgado, and S. Bonazzola, Astron. Astrophys. **296**, 745 (1995).
15. J.-L. Tassoul, *Theory of Rotating Stars* (Princeton Univ. Press, Princeton, 1979; Mir, Moscow, 1982).
16. M. J. Clement, Astrophys. J. **194**, 709 (1974).
17. O. Osterby and L. Zlatev, *Direct Methods for Sparse Matrices* (Springer-Verlag, Berlin, 1983; Mir, Moscow, 1987).
18. O. S. Bartunov and S. I. Blinnikov, Astron. Astrophys. **273**, 106 (1993).
19. J. P. Ostriker and P. Bodenheimer, Astrophys. J. **151**, 1089 (1968).
20. S. L. Shapiro and S. A. Teukolsky, *Black Holes, White Dwarfs, and Neutron Stars: the Physics of Compact Objects* (Wiley, New York, 1983; Mir, Moscow, 1985).
21. I. Hachisu, Astrophys. J., Suppl. Ser. **61**, 479 (1986).
22. I. Hachisu, Y. Eriguchi, and K. Nomoto, Astrophys. J. **308**, 161 (1986).
23. P. R. Feynman, N. Metropolis, and E. Teller, Phys. Rev. **75**, 1561 (1949).
24. G. Baym, C. J. Pethick, and P. Sutherland, Astrophys. J. **170**, 299 (1971).
25. G. Baym, H. A. Bethe, and C. J. Pethick, Nucl. Phys. A **175**, 225 (1971).
26. V. Canuto, Annu. Rev. Astron. Astrophys. **12**, 167 (1974).
27. E. Müller and Y. Eriguchi, Astron. Astrophys. **152**, 325 (1985).
28. V. S. Imshennik and D. K. Nadezhin, Pis'ma Astron. Zh. **18**, 195 (1992) [Sov. Astron. Lett. **18**, 79 (1992)].

Translated by D. Gabuzda

Astronomy Reports, Vol. 45, No. 9, 2001, pp. 700–710. Translated from Astronomicheskiĭ Zhurnal, Vol. 78, No. 9, 2001, pp. 807–818.

The Chemical Composition of the Red Giant η Ser

L. I. Antipova and A. A. Boyarchuk

Institute of Astronomy, Russian Academy of Sciences, Pyatnitskaya ul. 48, Moscow, 109017 Russia

Received December 8, 2000

Abstract—The paper presents the results of an analysis of elemental abundances in the atmosphere of η Ser—a red giant of spectral type K2IIIabCN1, according to Hoffleit and Jaschek [4]. The resulting atmospheric parameters correspond to a K0 giant, and the peculiarities of the star's chemical composition provide evidence that the assignment of η Ser to the class of CN stars was erroneous. *© 2001 MAIK "Nauka/Interperiodica".*

1. INTRODUCTION

In the early stages of the evolution of a star, various nuclear reactions take place in its core, leading to the formation of a series of chemical elements in these regions of nuclear burning. When the star evolves off the main sequence into the region occupied by red giants in the Hertzsprung–Russell diagram, it develops a convective envelope. This envelope gradually expands, reaches the inner layers where nuclear reactions were taking place during the star's lifetime on the main sequence, and carries the products of nuclear burning to the stellar surface. As a consequence, the atmospheres of red giants exhibit anomalous abundances of certain elements compared to those observed for the atmospheres of main-sequence stars.

Studies of these anomalies can yield important information about the internal structure of stars and the nuclear synthesis that occurs in their cores at various stages of their evolution. It is also known that the population of red giants is not uniform. Subgroups having certain spectral characteristics can be distinguished. For example, there is a subgroup of barium stars, whose spectra exhibit strong lines of barium and s-process elements, compared to so-called "normal" red giants (field red giants, which do not exhibit any spectral features). There also exist subgroups of stars with strong CH and CN molecular-band emission (CH and CN stars). Stars associated via a common origin (cluster members) also display certain features, and so forth. It is of interest to carry out comparative analyses of the physical conditions and chemical compositions of the atmospheres of red giants of various spectral subgroups, based on uniform spectral observational material and a single reduction technique. This will make it possible to establish relationships between observed spectral properties and evolutionary stages or age characteristics.

In our previous studies (see, for example, [1–3]), we performed such analyses for several field red giants, three "moderate" barium stars, and giants of the young Hyades cluster. Here, we present results for the red giant η Ser, which we selected for our program as a representative of the class of CN stars. When choosing objects for our program, we have been guided by the catalog of bright stars [4], which gives the spectral type of η Ser as K2IIIabCN1.

2. OBSERVATIONS, DATA REDUCTION, AND DETERMINATION OF ATMOSPHERIC PARAMETERS

As for the other stars in our program, the observations of η Ser were carried out using a spectrograph mounted at the Coudé focus of the 2.6-m telescope of the Crimean Astrophysical Observatory in 1996. The data were recorded on a CCD array. The observations were obtained in 19 selected spectral bands with widths to 60 Å. The resulting spectra have signal-to-noise ratios of 150–230; the resolution, determined by the spacing between pixels, is 0.066 Å.

The reduction of the observations, measurement of the equivalent widths, and estimates of the atmospheric parameters were carried out using the same methods as in our earlier studies. These methods are described in detail in [3], which also discusses the accuracy of the resulting parameter estimates. Therefore, we present here only the results of our analysis for η Ser.

Figure 1 shows the abundances of iron-group elements relative to their solar abundances,

$$[X] = \log(N_{elem}/\mathrm{H})_* - \log(N_{elem}/\mathrm{H})_\odot,$$

calculated from the observed equivalent widths of absorption lines in the spectrum of η Ser using various temperatures and $\log g = 3.01$. We also constructed such plots for other values of $\log g$. On each plot, we estimated the scatter of the lines at the point where they intersect. The minimum of this scatter can be used to determine the parameters of the atmosphere of η Ser, as

1063-7729/01/4509-0700$21.00 © 2001 MAIK "Nauka/Interperiodica"

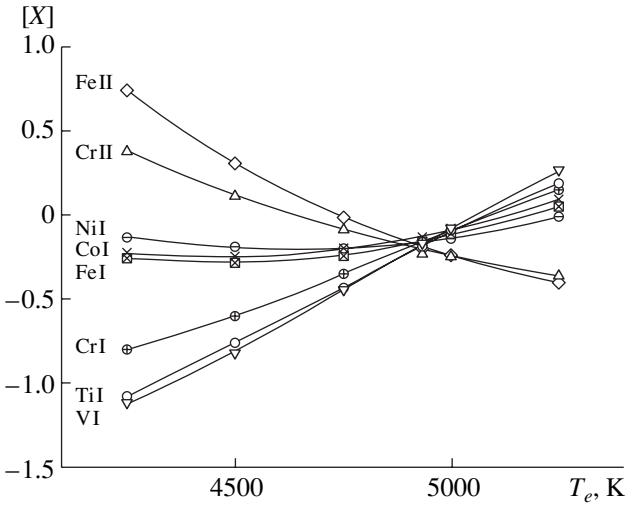

Fig. 1. Abundances of iron-group elements relative to their solar values, calculated from the equivalent widths of absorption lines in the spectrum of η Ser for various temperatures and $\log g = 3.01$.

is clearly illustrated in Fig. 2. Plots such as those in Fig. 1 also yield the metallicity of the star—the ratio of the abundances of iron-group elements in the star's atmosphere to their solar abundances.

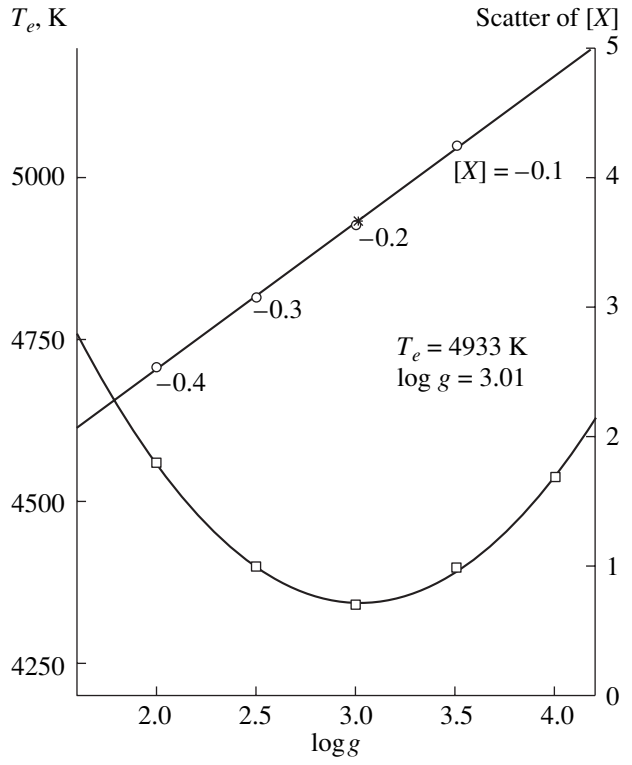

Fig. 2. T_e–$\log g$ diagram for determining the main parameters of the atmosphere of η Ser (see [1] for more information about the construction of this diagram).

Our estimates of the parameters of the atmosphere of η Ser are given in Table 1; we also present the analogous values obtained in other studies for comparison. It is clear from this table that our temperature estimate is in fairly good agreement with those found in other studies; however, it is appreciably higher than expected for a K2 giant, and corresponds to type K0. Our value for $\log g$ is also close to those derived in earlier studies.

3. RESULTS AND DISCUSSION

Table 2 presents a list of the spectral lines used to derive the elemental abundances for the atmosphere of η Ser and the measured equivalent widths. Table 3 presents the abundances calculated from these data using a model atmosphere corresponding to $T_e = 4333$ K and $\log g = 3.01$. It follows from this table that the metallicity (mean abundance of iron-group elements) of η Ser is nearly 0.2 dex higher than the solar value. Figure 3 shows ratios of elemental abundances to the metallicity (M) in the atmosphere of η Ser in comparison with the corresponding "solar" values; i.e.,

$$[X/M] = [X/M]_* - [X/M]_\odot. \quad (1)$$

It is clear that the abundances of Na, Mg, Al, and Si are somewhat higher than their "normal" values, as is observed in other red giants [3]. The overabundances of Na, Al, and Si fit well in the corresponding dependence on the gravitational acceleration constructed on the basis of analyses for other red giants and supergiants (see Figs. 2–4 in [3]). We also observe an overabundance of *s*-process elements (relative to the metallicity), as was found earlier for other red giants [3]. However, on average, these overabundances are somewhat lower than those for field red giants. In this sense, they occupy an intermediate position between field giants and the young Hyades giants.

Note that field giants do not represent a uniform group in either T_e and $\log g$ or in the abundances anom-

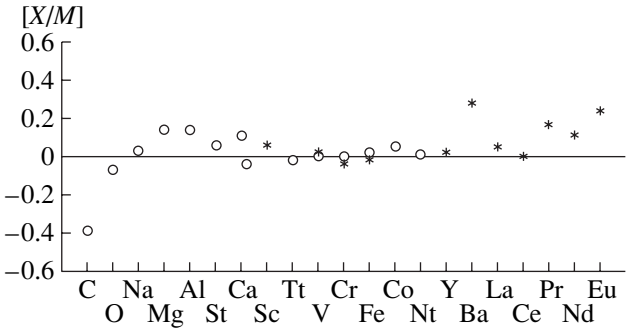

Fig. 3. Chemical composition of the atmosphere of η Ser calculated using a model atmosphere with $T_e = 4933$ K and $\log g = 3.01$.

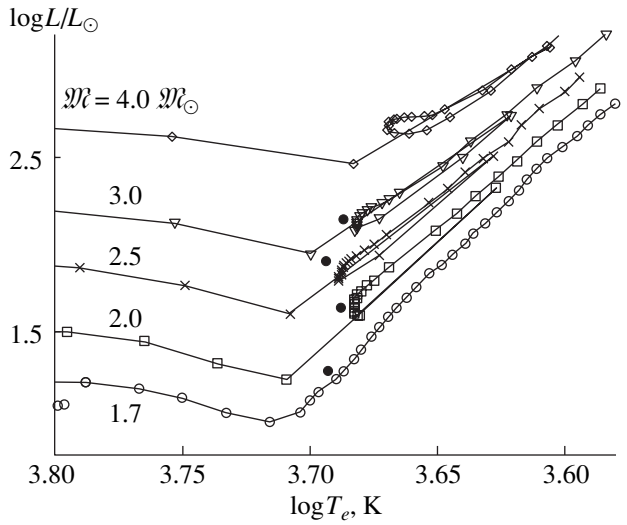

Fig. 4. Positions of stars from Table 4 on evolutionary tracks from [9].

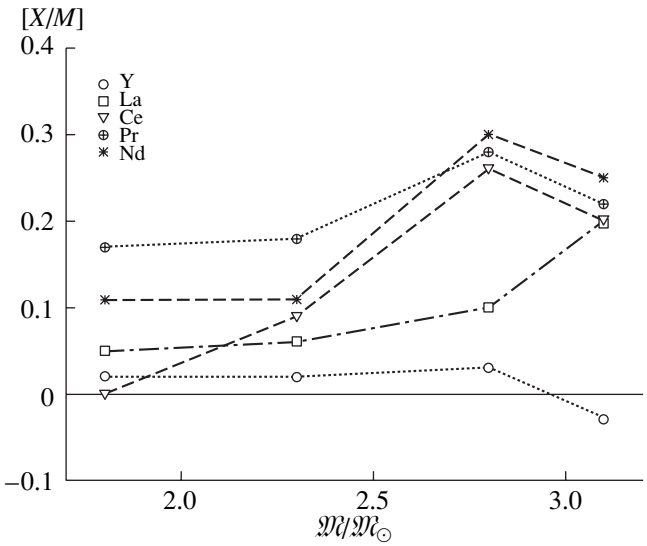

Fig. 5. Comparison of abundances of *s*-process elements in the atmospheres of η Ser and several stars with similar atmospheric parameters (Table 4).

alies for individual elements. Therefore, when comparing the abundances of *s*-process elements in the atmosphere of η Ser with those for other giants, we chose stars whose parameters were most similar to those of η Ser. Figure 4 shows the positions of these stars on the Hertzsprung–Russell diagram, together with evolutionary tracks constructed using the data of [9]. It is clear from this figure that these stars form a distinct group in luminosity and mass; the masses estimated from the evolutionary tracks are presented in Table 4, which also gives the atmospheric parameters and metallicities for these stars obtained in the current and earlier studies.

We investigated the possibility of a relation between a star's overabundance in *s*-process elements and its mass. The overabundances of each of the *s*-process elements as a function of the corresponding stellar mass are plotted in Fig. 5. This plot was constructed using the data of [3] and Table 3; the horizontal axis plots the stellar masses in solar units and the vertical axis the *s*-process element overabundances derived from (1). We are inclined to exclude the *s*-process element barium from this analysis, since its abundances in red giants can be strongly affected by non-LTE effects. It is clear from Fig. 5 and Table 4 that there is a tendency for the overabundances of *s*-process elements to increase with the stellar mass (or equivalently the luminosity). This is evidently associated with the fact that the process of convective mixing is developed to different degrees in stars of different masses when they reach the red-giant stage: the higher the mass, the stronger the convection, the deeper the layers to which it penetrates, and the larger the amount of material that is carried from the core to the surface of the star.

Table 1. Atmospheric parameters of η Ser

T_e, K	log$g$	V_t, km/s	[Fe/H]	References
4933	3.01	0.9	–0.21	This paper
4890	3.21	2.1	–0.42	[5]
4940	2.91	2.4	+0.08	[6]
4912	3.10	0.85	–0.31	[7]
4830	2.90	(1.7)*	–0.20	[8]

* In [8], a single turbulence velocity of 1.7 km/s was adopted for all the studied stars.

Note, however, that the overabundances of these elements also depend on the star's metallicity, which is obviously related to its age; with increase in the metallicity (or decrease in the age), these overabundances decrease. It was shown earlier that red giants of the very young Hyades cluster do not show any overabundances in *s*-process elements in their atmospheres, due to their young ages and the corresponding limited development of mixing processes [2]. Figure 5 also shows some decrease in the overabundances for star with metallicities higher than the solar value.

Due to the limited number of red giants investigated by us thus far, we cannot at this time analyze this question in more detail. Preferring to undertake homogeneous studies in terms of observational material and technique, we decided not to include here data of studies by other authors. However, we hope to return to this question later, after expanding our investigations to additional red giants.

Table 2. List of spectral data

λ, Å	E.P., eV	log*gf*	W_λ, mÅ	λ, Å	E.P., eV	log*gf*	W_λ, mÅ
1	2	3	4	1	2	3	4
CI				SiI			
5380.31	7.68	−1.68	8.8	6145.08	5.59	−1.41	38.0
				6155.20	5.62	−0.80	72.7
OI				6155.70	5.62	−2.22	8.7
6300.34	0.00	−9.76	19.2				
				CaI			
NaI				5260.39	2.52	−1.74	52.4
6154.22	2.10	−1.51	60.4	5867.57	2.92	−1.59	39.8
6160.75	2.10	−1.21	79.0	6156.10	2.51	−2.46	23.3
				6166.44	2.51	−1.15	87.7
MgI				6455.60	2.52	−1.34	82.6
6318.71	5.11	−1.94	57.5				
6319.24	5.11	−2.22	48.4	ScII			
5711.09	4.34	−1.46	130.5	5318.34	1.35	−1.69	28.1
				5334.22	1.49	−2.10	13.5
AlI				5357.20	1.50	−2.15	10.4
6698.67	3.13	−1.86	39.4	5526.81	1.77	0.21	92.0
				5552.22	1.45	−2.10	11.1
SiI				5669.03	1.50	−0.99	56.8
5517.55	5.08	−2.40	20.2	6300.68	1.51	−1.97	17.9
5684.47	4.95	−1.57	61.9	6320.84	1.50	−1.83	22.0
5690.43	4.93	−1.73	53.4	6604.59	1.36	−1.11	59.2
5701.12	4.93	−1.96	45.9				
5772.25	5.06	−1.70	54.8	TiI			
5793.05	4.93	−1.89	46.9	5145.47	1.46	−0.45	72.7
6112.93	5.62	−2.19	12.8	5147.48	0.00	−1.96	90.0
6125.03	5.59	−1.57	33.6	5223.63	2.09	−0.53	45.0
6131.54	5.59	−1.75	28.2	5251.49	0.82	−2.49	18.9
6131.86	5.59	−1.68	29.2	5259.96	2.74	−0.27	17.7
6142.53	5.59	−1.49	35.8	5282.40	1.05	−1.53	49.8

Table 2. (Contd.)

λ, Å	E.P., eV	log*gf*	W_λ, mÅ	λ, Å	E.P., eV	log*gf*	W_λ, mÅ
1	2	3	4	1	2	3	4
5295.78	1.06	−1.65	47.6	6599.11	0.90	−1.99	45.2
5313.25	1.06	−2.25	17.1	6716.68	2.48	−1.14	0.3
5351.07	2.77	−0.07	28.0				
5366.65	0.81	−2.54	22.2	VI			
5384.63	0.83	−2.78	11.3	5240.88	2.37	0.33	18.5
5426.24	0.02	−2.87	43.0	5507.77	2.36	−0.17	9.2
5438.29	1.43	−1.87	13.1	5668.37	1.08	−0.96	26.6
5448.91	2.33	−1.32	9.3	5670.85	1.08	−0.39	65.0
5449.16	1.44	−2.00	16.9	5703.56	1.05	−0.26	77.9
5503.89	2.58	−0.09	37.0	5731.25	1.06	−0.76	44.6
5673.41	3.11	−0.36	8.2	5743.43	1.08	−0.91	31.9
5679.92	2.47	−0.63	19.8	5776.67	1.08	−1.49	10.4
5689.46	2.30	−0.40	36.7	5830.68	3.11	0.69	9.4
5702.64	2.29	−0.65	26.8	6039.69	1.06	−0.64	49.1
5713.88	2.29	−0.93	13.8	6058.18	1.04	−1.39	14.0
5716.45	2.30	−0.78	19.9	6081.44	1.05	−0.63	56.5
5774.03	3.30	0.45	23.5	6090.21	1.08	−0.13	79.3
5823.69	2.27	−1.22	14.7	6111.62	1.04	−0.71	53.4
5832.48	3.34	−0.31	7.6	6119.50	1.06	−0.44	67.7
5839.77	1.46	−2.40	7.5	6135.36	1.05	−0.76	51.5
5880.27	1.05	−1.94	35.8	6150.13	0.30	−1.51	59.4
5999.67	2.23	−0.78	20.2	6216.35	0.28	−0.88	89.3
6031.68	0.05	−3.92	9.2	6224.50	0.29	−1.82	42.9
6064.63	1.05	−1.82	43.0	6285.16	0.28	−1.56	56.4
6092.80	1.89	−1.36	17.4	6292.82	0.29	−1.47	62.7
6098.66	3.06	−0.10	18.1	6326.84	1.87	−0.76	14.5
6121.01	1.87	−1.34	19.2	6504.16	1.18	−0.74	38.0
6126.22	1.06	−1.34	68.2				
6149.74	2.15	−1.26	9.0	VII			
6303.77	1.44	−1.50	40.0	5303.26	2.27	−1.98	14.2
6312.24	1.46	−1.52	39.2	6031.07	2.51	−1.59	8.8
6325.15	0.02	−3.57	18.4				
6336.10	1.44	−1.69	34.0	CrI			
6497.68	1.44	−1.93	26.8	5122.12	1.03	−3.14	46.1

Table 2. (Contd.)

λ, Å	E.P., eV	log*gf*	W_λ, mÅ	λ, Å	E.P., eV	log*gf*	W_λ, mÅ
1	2	3	4	1	2	3	4
5238.97	2.71	−1.34	37.0	5334.88	4.07	−1.62	39.6
5240.46	3.67	−0.59	24.4	5502.09	4.17	−1.89	20.1
5241.46	2.71	−2.05	16.0	5508.62	4.15	−2.01	19.3
5243.35	3.39	−0.59	40.7				
5247.56	0.96	−1.65	113.2				
5272.00	3.45	−0.47	39.8	FeI			
5285.62	3.37	−1.48	10.6	5136.09	4.17	−1.90	40.3
5287.18	3.44	−0.87	22.7	5143.73	2.20	−3.74	59.6
5296.69	0.98	−1.39	128.4	5145.11	2.20	−3.12	76.4
5300.75	0.98	−2.07	97.9	5159.06	4.28	−0.82	71.1
5304.21	3.45	−0.63	28.6	5223.19	3.63	−2.21	45.8
5312.88	3.43	−0.54	33.6	5228.37	4.22	−1.05	70.0
5318.78	3.43	−0.68	29.4	5242.50	3.63	−0.91	100.3
5345.81	1.00	−0.90	169.8	5243.78	4.26	−0.94	77.4
5348.32	1.00	−1.20	133.4	5249.11	4.47	−1.53	28.2
5719.82	3.01	−1.66	17.9	5253.48	3.28	−1.45	91.6
5729.20	3.84	−1.18	6.6	5285.13	4.43	−1.42	38.7
5783.11	3.31	−0.34	50.5	5293.97	4.12	−1.72	46.5
5787.99	3.31	−0.09	60.9	5294.55	3.62	−2.64	31.2
5788.39	3.00	−1.60	18.5	5295.32	4.40	−1.50	41.9
5843.24	3.00	−2.03	8.3	5315.07	4.35	−1.44	44.4
5884.44	3.01	−1.81	12.6	5315.78	3.62	−3.13	12.3
6135.78	4.80	0.55	23.1	5320.05	3.63	−2.43	37.9
6330.09	0.94	−2.83	78.8	5321.11	4.42	−1.24	50.7
6501.21	0.98	−3.61	21.3	5322.05	2.27	−2.81	87.9
6630.02	1.03	−3.48	39.4	5358.10	3.29	−3.23	24.2
6680.14	4.16	−0.40	14.4	5365.40	3.56	−1.05	90.1
6734.16	4.19	−0.71	12.2	5373.71	4.47	−0.69	70.5
				5376.84	4.29	−2.00	28.4
CrII				5379.57	3.69	−1.44	74.6
5237.32	4.07	−1.12	53.2	5385.55	3.69	−3.08	10.6
5305.85	3.81	−2.00	29.2	5386.34	4.15	−1.67	44.6
5310.70	4.05	−2.18	12.1	5389.45	4.41	−0.26	86.2
5313.59	4.06	−1.61	36.1	5395.22	4.44	−1.67	33.0

Table 2. (Contd.)

λ, Å	E.P., eV	log*gf*	W_λ, mÅ	λ, Å	E.P., eV	log*gf*	W_λ, mÅ
1	2	3	4	1	2	3	4
5398.28	4.44	−0.51	78.3	5827.88	3.28	−3.10	28.7
5401.29	4.32	−1.68	38.9	5835.11	4.26	−2.09	26.2
5406.78	4.37	−1.35	49.2	5837.70	4.29	−2.13	17.5
5412.79	4.43	−1.73	32.3	5838.42	3.93	−2.21	36.8
5417.04	4.41	−1.37	46.5	5844.88	4.14	−2.83	8.6
5432.95	4.44	−0.61	78.1	5845.27	5.01	−1.70	11.5
5441.35	4.31	−1.55	44.9	5849.70	3.68	−2.82	19.0
5445.04	4.39	−0.01	109.0	5852.19	4.53	−1.17	57.0
5522.40	4.21	−1.40	55.4	5853.18	1.48	−5.03	35.2
5539.83	4.29	−2.29	14.1	5855.13	4.59	−1.54	36.9
5544.04	4.22	−0.92	74.4	5856.08	4.28	−1.51	49.7
5546.63	4.37	−1.04	62.9	5858.77	4.20	−2.13	26.2
5552.70	4.95	−1.69	11.8	5859.61	4.55	−0.49	82.9
5554.90	4.55	−0.23	94.2	5861.11	4.26	−2.31	15.4
5560.38	4.43	−1.01	58.5	5862.36	4.53	−0.36	92.0
5677.70	4.10	−2.56	15.4	5864.24	4.28	−2.40	14.0
5679.02	4.65	−0.57	66.8	5873.22	4.26	−1.97	32.0
5686.54	4.55	−0.56	83.3	5879.49	4.61	−1.88	20.1
5701.56	2.56	−2.02	113.2	5983.69	4.55	−0.54	72.3
5705.47	4.30	−1.40	52.2	5984.82	4.74	−0.14	79.6
5720.90	4.55	−1.81	25.3	6003.03	3.86	−1.12	97.6
5724.47	4.28	−2.46	11.9	6007.96	4.63	−0.62	72.7
5731.77	4.26	−1.06	63.1	6019.36	3.56	−3.20	20.7
5732.30	4.99	−1.40	20.7	6024.07	4.53	0.12	108.5
5752.04	4.55	−0.80	66.6	6027.06	4.07	−1.03	80.2
5753.13	4.26	−0.55	92.0	6034.04	4.29	−2.28	17.9
5760.35	3.63	−2.32	41.3	6054.10	4.35	−2.16	19.5
5775.09	4.20	−1.10	74.5	6056.01	4.73	−0.30	77.5
5778.47	2.58	−3.42	51.0	6078.50	4.79	−0.26	84.5
5784.69	3.38	−2.24	51.5	6079.02	4.65	−0.91	59.8
5793.91	4.22	−1.55	50.0	6089.57	5.02	−0.79	52.4
5806.73	4.61	−0.82	61.6	6093.65	4.61	−1.30	41.5
5809.22	3.88	−1.59	62.0	6094.38	4.65	−1.50	30.9
5826.64	4.28	−2.83	7.2	6096.67	3.98	−1.71	55.6

Table 2. (Contd.)

λ, Å	E.P., eV	log*gf*	W_λ, mÅ	λ, Å	E.P., eV	log*gf*	W_λ, mÅ
1	2	3	4	1	2	3	4
6098.25	4.56	−1.74	29.0	6653.88	4.14	−2.42	21.5
6102.18	4.83	−0.07	89.1	6699.14	4.57	−2.07	15.8
6105.13	4.55	−1.94	21.4	6703.57	2.75	−2.95	64.0
6120.25	0.91	−5.81	31.4	6704.48	4.20	−2.55	14.6
6148.65	4.30	−2.61	9.8	6710.31	1.48	−4.77	59.8
6151.62	2.17	−3.18	79.4	6712.44	4.97	−2.04	10.7
6157.73	4.06	−1.11	83.4	6713.76	4.77	−1.39	33.7
6159.41	4.59	−1.82	23.5	6715.41	4.59	−1.48	47.2
6165.37	4.12	−1.37	59.7	6716.24	4.58	−1.74	32.7
6173.34	2.21	−2.76	101.3	6726.67	4.59	−0.98	65.6
6187.99	3.94	−1.58	66.2	6732.06	4.58	−2.06	15.0
6200.32	2.61	−2.30	108.6	6733.16	4.64	−1.38	45.5
6213.44	2.22	−2.46	11.1	6737.98	4.56	−1.64	41.5
6219.28	2.20	−2.25	125.8	6739.54	1.55	−4.82	47.7
6226.72	3.88	−2.04	50.9	6752.72	4.62	−1.17	59.3
6290.97	4.73	−0.54	77.1	6783.71	2.58	−3.83	46.3
6297.80	2.22	−2.58	110.4	6786.88	4.17	−1.87	42.9
6307.85	3.64	−3.21	12.6	6793.27	4.12	−2.34	30.4
6322.68	2.59	−2.26	113.6	68704.01	4.65	−1.57	42.7
6330.85	4.73	−1.14	50.1	6806.86	2.73	−3.05	69.7
6385.73	4.73	−1.78	18.0	6810.27	4.61	−0.92	66.9
6392.54	2.28	−3.89	51.3				
6436.41	4.19	−2.35	23.0	FeII			
6481.87	2.27	−2.83	99.7	5100.66	2.81	−4.09	26.4
6495.78	4.81	−0.93	58.8	5234.63	3.22	−2.19	80.0
6496.46	4.77	−0.50	82.8	5325.56	3.22	−3.27	44.0
6498.95	0.95	−4.55	91.2	5414.07	3.22	−3.53	29.2
6593.87	2.42	−2.18	116.2	5425.26	3.20	−3.22	43.8
6597.60	4.77	−0.95	52.2	5991.38	3.15	−3.51	36.2
6608.04	2.28	−3.88	47.4	6084.10	3.20	−3.76	27.0
6609.12	2.56	−2.56	100.8	6113.33	3.21	−4.09	16.9
6627.56	4.55	−1.46	44.6	6149.24	3.87	−2.67	37.3
6646.98	2.60	−3.86	38.3	6416.93	3.89	−2.69	41.8
6648.08	1.01	−5.76	42.2	6432.68	2.89	−3.50	47.8

Table 2. (Contd.)

λ, Å	E.P., eV	log*gf*	W_λ, mÅ	λ, Å	E.P., eV	log*gf*	W_λ, mÅ
1	2	3	4	1	2	3	4
6456.39	3.90	−2.03	58.7	5760.85	4.09	−0.72	45.9
				5805.22	4.17	−0.51	49.9
CoI				5847.01	1.67	−3.39	54.7
5149.79	1.73	−2.16	33.5	5996.74	4.23	−0.96	29.2
5287.78	4.05	−0.31	11.8	6007.31	1.67	−3.30	55.5
5325.27	4.02	−0.03	18.3	6025.77	4.23	−1.68	9.2
5342.70	4.00	−0.62	43.0	6053.68	4.23	−1.01	30.7
5352.05	3.56	−0.02	44.2	6086.28	4.26	−0.39	55.8
5359.19	4.15	0.11	16.8	6108.12	1.68	−2.54	98.4
5368.93	3.51	−1.18	7.3	6111.06	4.07	−0.75	47.6
5381.76	4.24	−0.13	13.8	9118.06	4.09	−2.08	7.5
5523.34	2.32	−1.58	27.3	6128.99	1.67	−3.30	60.6
5530.78	1.70	−2.04	53.0	6130.17	4.25	−0.92	30.2
6000.67	3.61	−0.80	9.0	6133.95	4.07	−1.76	13.2
6005.03	1.70	−3.40	8.0	6175.37	4.09	−0.45	56.4
6093.15	1.70	−2.27	40.4	6176.82	4.09	−0.17	71.2
6117.00	1.78	−2.45	27.5	6177.25	1.83	−3.47	39.8
6188.98	1.71	−2.19	41.8	6186.71	4.10	−0.87	44.7
6347.84	4.39	−0.09	11.8	6204.60	4.09	−1.09	36.9
6455.00	3.63	−0.26	32.5	6223.98	4.10	−0.93	43.4
6632.44	2.27	−1.83	34.7	6316.58	4.15	−1.90	14.5
				6322.17	4.15	−1.16	28.0
NiI				6327.60	1.68	−3.01	80.1
5102.98	1.68	−2.86	74.6	6424.86	4.17	−1.32	23.2
5115.40	3.83	−0.03	78.6	6598.59	4.22	−0.88	34.6
5155.13	3.90	−0.60	56.6	6635.15	4.40	−0.71	37.0
5155.77	3.90	0.06	74.0	6643.64	1.67	−1.86	135.3
5157.98	3.61	−1.53	30.6	6767.78	1.83	−1.95	113.3
5259.48	3.74	−1.80	16.9	6772.36	3.64	−0.89	67.2
5392.33	4.15	−1.28	23.8				
5435.87	1.99	−2.43	79.6				
5682.20	4.10	−0.34	61.6	YII			
5748.35	1.68	−3.15	62.4	5119.12	0.99	−1.35	32.4
5749.31	3.94	−1.95	10.8	5289.82	1.03	−1.84	12.0

Table 2. (Contd.)

λ, Å	E.P., eV	log*gf*	W_λ, mÅ	λ, Å	E.P., eV	log*gf*	W_λ, mÅ
1	2	3	4	1	2	3	4
5402.78	1.84	−0.57	24.6	PrII			
5544.61	1.74	−1.08	14.3	5219.02	0.79	0.11	11.2
6795.41	1.72	−1.12	16.4	5259.73	0.63	−0.04	14.2
				5322.78	0.48	−0.31	12.5
ZrII				5352.40	0.48	−0.60	7.7
5350.10	1.82	−0.87	16.6				
6114.78	1.66	−1.66	5.8	NdII			
				5306.49	0.86	−0.65	7.3
BaII				5356.99	1.26	−0.14	9.2
5853.68	0.60	−0.80	95.0	5385.89	0.74	−0.83	8.7
6141.72	0.70	0.17	147.2	5431.53	1.12	−0.29	11.0
6496.89	0.60	−0.08	143.1	5842.39	1.28	−0.49	6.0
				6790.37	0.18	−1.58	8.8
LaII							
6774.28	0.13	−1.63	13.3	EuII			
				6437.70	1.32	0.05	14.6
CeII				6645.11	1.37	0.20	17.4
5274.24	1.04	0.34	22.6	PrII			
5330.58	0.87	−0.30	10.1	5219.02	0.79	0.11	11.2
6043.39	1.21	−0.25	7.9				

We noted above that η Ser was chosen for our program as a red giant with enhanced CN bands (a CN-strong star), based on the classification of its spectrum as K2IIIabCN1 in the catalog of bright stars [4]. However, we have not found any features characteristic for red giants of this subclass in the chemical composition of its atmosphere. Indeed, we note the following.

(1) According to [10], most CN stars have enhanced metal abundances, while we found for η Ser M = –0.18 dex.

(2) CN stars do not display overabundances of *s*-process elements [10], while we have found such overabundances for η Ser.

(3) It is noted in the review [11] that enhanced abundances of nitrogen ([N/Fe] ~ +(0.5–1.0) dex) are characteristic of CN stars, while a smaller value ([N/Fe] = +0.10 dex) was found in [12] for η Ser. The carbon abundance of η Ser is [C/Fe] = –0.38 dex [12], in good agreement with our estimate –0.39 dex (Table 3), and the essentially normal oxygen abundance [12] is typical of "normal" red giants.

(4) Earlier, based on studies of globular clusters [12], overabundances of Na and Al were considered characteristic of CN stars. Currently, the presence of overabundances of these elements has also been established for "normal" field giants and supergiants [3, 12, 13], and a relation between these overabundances and luminosity has been demonstrated. Thus, this property of η Ser is not characteristic of CN stars.

Thus, we conclude that η Ser is an ordinary field red giant, and that its classification as a CN star in [4] was erroneous. This is confirmed by the fact that, in the later electronic version of the catalog of bright stars [14], the spectrum of η Ser is classified as K0III–IV.

Table 3. Elemental abundances in the atmosphere of η Ser

Element	Number of lines	X	$X_\odot$	$[X]$
1	2	3	4	5
CI	1	−3.98	−3.41	−0.57
OI	1	−3.27	−3.02	−0.25
NaI	2	−5.84 ± 0.00	−5.69	−0.15
MgI	3	−4.52 ± 0.08	−4.48	−0.04
Al	1	−5.64	−5.60	−0.04
SiI	14	−4.61 ± 0.06	−4.49	−0.12
CaI	5	−5.82 ± 0.05	−5.75	−0.07
ScII	9	−9.04 ± 0.06	−8.92	−0.12
TiI	42	−7.19 ± 0.10	−6.99	−0.20
VI	23	−8.14 ± 0.11	−7.96	−0.18
VII	2	−8.15 ± 0.19	−7.99	−0.16
CrI	29	−6.49 ± 0.10	−6.31	−0.18
CrII	7	−6.52 ± 0.11	−6.30	−0.22
FeI	151	−4.70 ± 0.11	−4.53	−0.17
FeII	12	−4.69 ± 0.07	−4.49	−0.20
CoI	18	−7.24 ± 0.11	−7.11	−0.13
NiI	40	−5.92 ± 0.11	−5.75	−0.17
YII	5	−9.86 ± 0.06	−9.70	−0.16
ZrII	2	−9.38 ± 0.02	−9.45	+0.07
BaII	3	−9.80 ± 0.05	−9.90	+0.10
LaII	1	−10.02	−10.79	−0.13
CeII	3	−10.65 ± 0.08	−10.47	−0.18
PrII	3	−11.38 ± 0.03	−11.37	−0.01
NdII	6	−10.70 ± 0.07	−10.63	−0.07
EuII	2	−10.43 ± 0.01	−11.49	+0.06
			$M^{*)} = -0.18 \pm 0.02$	

* The metallicity M was taken to be the average of the abundances of iron-group elements.

Table 4. Red giants with similar atmospheric parameters

Star	T_e, K	$\log g$	M	$\mathcal{M}/\mathcal{M}_\odot$
η Ser	4933	3.01	−0.18	1.8
β Gem	4933	3.00	+0.09	2.3
δ Dra	4897	2.86	−0.10	2.8
η Cyg	4906	2.85	+0.15	3.1

ACKNOWLEDGMENTS

This work was partially supported by the Russian Foundation for Basic Research (project code 00-02-17660). Observations for a number of stars were obtained using a Photometrics GmbH SDS-9000 CCD array mounted on the 2.6-m telescope of the Crimean Astrophysical Observatory, provided by support from the International Science Foundation (grants R2Q000 and U1C000) and the ESO C&EE Program (grant A-05-067).

REFERENCES

1. A. A. Boyarchuk, L. I. Antipova, M. E. Boyarchuk, and I. S. Savanov, Astron. Zh. **73**, 862 (1996) [Astron. Rep. **40**, 783 (1996)].
2. A. A. Boyarchuk, L. I. Antipova, M. E. Boyarchuk, and I. S. Savanov, Astron. Zh. **77**, 96 (2000) [Astron. Rep. **44**, 76 (2000)].
3. A. A. Boyarchuk, L. I. Antipova, M. E. Boyarchuk, and I. S. Savanov, Astron. Zh. **78**, 349 (2001) [Astron. Rep. **45**, 301 (2001)].
4. D. Hoffleit and C. Jaschek, *The Bright Star Catalogue* (Yale Univ. Observatory, New Haven, 1982, 4th ed.).
5. A. McWilliam, Astrophys. J., Suppl. Ser. **74**, 1075 (1990).
6. L. Gratton, S. Gaudenzi, C. Rossi, and R. G. Gratton, Mon. Not. R. Astron. Soc. **201**, 807 (1982).
7. R. Glebocki, Acta Astron. **22**, 141 (1972).
8. P. Kjergaard, B. Gustafsoon, G. A. H. Walker, and L. Hultqvist, Astron. Astrophys. **115**, 145 (1982).
9. G. Schaller, D. Schaerer, G. Meynet, and A. Maeder, Astron. Astrophys., Suppl. Ser. **96**, 269 (1992).
10. P. C. Keenan and A. Heck, Rev. Mex. Astron. Astrofis. **29**, 103 (1994).
11. G. H. Smith, *The Abundance Spread within Globular Clusters: Spectroscopy of Individual Stars*, Ed. by G. Gayrel de Strobel, M. Spite, T. Lloyd Evans (Observatoire de Paris, 1989), p. 63.
12. A. A. Boyarchuk and L. S. Lyubimkov, Izv. Krym. Astrofiz. Obs. **66**, 130 (1983).
13. N. S. Komarov, T. V. Mishenina, and I. D. Motrich, Astron. Zh. **62**, 740 (1985) [Sov. Astron. **29**, 434 (1985)].
14. D. Hoffleit and W. H. Warren, Jr., *The Bright Star Catalogue*, Ed. by D. Hoffleit and C. Jaschek, IV (Yale Univ. Observatory, New Haven, 1991, 5th ed.).

Translated by D. Gabuzda

Astronomy Reports, Vol. 45, No. 9, 2001, pp. 711–717. Translated from Astronomicheskiĭ Zhurnal, Vol. 78, No. 9, 2001, pp. 819–826.

Luminosity Calibration for OB Stars from Hipparcos Trigonometric Parallaxes

A. V. Loktin and G. V. Beshenov

Astronomical Observatory, Ural State University, pr. Lenina 51, Yekaterinburg, 620083 Russia

Received October 16, 2000

Abstract—Hipparcos trigonometric parallaxes and observational data for open clusters are used to determine the absolute magnitudes M_V of O and B stars of various spectral subtypes and luminosity classes, including those with broadened lines and hydrogen emission lines. The same data are used to derive a relation between M_V and the index β of the Strömgren photometric system. The resulting calibrations and the spectroscopic-parallax method are used to determine the distances to young open clusters. © *2001 MAIK "Nauka/Interperiodica".*

1. INTRODUCTION

As the most luminous stars in our Galaxy, OB stars are very convenient objects for investigations of the structure and kinematics of the Milky Way and Magellanic Clouds. The high luminosities of these stars make it possible to study a large fraction of the total volume of the Galaxy using large samples of several thousand stars. The luminosities of these stars are sufficiently high to enable determination of distances to young stellar groupings—open clusters and OB associations—in both the Milky Way and other galaxies. Unfortunately, the luminosity calibrations now available for OB stars are not very trustworthy, due primarily to the fact that they have been based on data for stars in open clusters, and the underlying distance scale for the youngest clusters which contain OB stars has always been the most poorly determined. In the past, open-cluster distance scales were based on the distance to a single cluster—the Hyades, which contains no bright main-sequence stars. Moreover, the upper Zero-Age Main Sequence (ZAMS), which determines the distance scale for OB stars, was constructed by fitting the Hyades main sequence to the main sequences of younger open clusters. This procedure is inevitably fraught with substantial systematic errors, due to the appreciable width of the cluster main sequences. See Kholopov's [1] monograph for a discussion of the problems encountered in constructing the ZAMSs for young stars.

The situation with open-cluster distances improved substantially recently following the release of trigonometric parallaxes measured by the Hipparcos satellite. Robishon *et al.* [2], Loktin and Beshenov [3], and other researchers used Hipparcos parallaxes to refine the distance scale of the nearest open clusters. Using Hipparcos trigonometric parallaxes, Loktin and Beshenov [3] found that the distance scale for young open clusters is in satisfactory agreement with that for intermediate-age clusters. However, the accuracy of this result remains fairly low due to the small number of very young clusters in the nearest solar neighborhood (i.e., those younger than the Pleiades). Problems with the luminosity calibrations of B stars have been pointed out by Jaschek *et al.* [4]. The current work was undertaken in response to the need to refine the luminosity calibrations for O and B stars and improve the reliability of the distance scale for the youngest open clusters.

2. ABSOLUTE MAGNITUDES OF CLASS V, IV, AND III B STARS

Loktin and Beshenov [3] showed that Hipparcos trigonometric parallaxes enable the determination of the absolute magnitudes M_V for a fairly large number of distant stars. For example, at a distance of 1000 pc, the mean error in the absolute magnitude M_V inferred from a trigonometric parallax is $0\overset{m}{.}7$, and, naturally, the errors are smaller for more nearby stars. It follows that 10–20 stars are needed to achieve a calibration accuracy of $0\overset{m}{.}1$. Such samples can be drawn from the Hipparcos catalog for many spectral subtypes and luminosity classes of O and B stars.

We based our calibration sample on a continually updated catalog containing the kinematical characteristics of O and B stars. We first selected from this list all stars having Hipparcos parallaxes (a total of 873 objects). Since this list contains no B6–B8 stars (except supergiants), we added 367 such stars drawn from the Bright Star Catalogue [5] for which Hipparcos parallaxes are available. The combined 1240-object sample contains very few O stars and supergiants, and we accordingly further expanded our calibration database by adding a number of open-cluster stars (see below). However, we first determined the calibration for stars of luminosity classes V, IV, and III based exclusively on the Hipparcos data. We excluded from our initial sample all stars

Table 1. Mean absolute magnitudes of class V, IV, and III B stars derived from Hipparcos parallaxes

Sp	Luminosity class V	Luminosity class IV	Luminosity class III
B0	−3.42 ± 0.25 (11)	−3.49 ± 0.34 (6)	−4.00 ± 0.43 (5)
B0.5	−3.16 ± 0.39 (11)	−3.89 ± 0.29 (6)	−3.58 ± 0.34 (12)
B1	−2.83 ± 0.14 (37)	−3.94 ± 0.33 (4)	−3.79 ± 0.47 (7)
B1.5	−2.21 ± 0.20 (128)	−2.99 ± 0.18 (6)	−3.60 ± 0.27 (5)
B2	−2.11 ± 0.08 (115)	−2.60 ± 0.11 (51)	−2.77 ± 0.23 (21)
B3	−1.56 ± 0.06 (128)	−1.95 ± 0.11 (52)	−2.33 ± 0.15 (35)
B4	−1.44 ± 0.17 (21)	−1.16 ± 0.12 (9)	−2.09 ± 0.62 (6)
B5	−1.20 ± 0.08 (65)	−1.32 ± 0.18 (16)	−1.46 ± 0.17 (29)
B6	−0.86 ± 0.13 (31)	−1.06 ± 0.21 (18)	−1.40 ± 0.18 (13)
B7	−0.58 ± 0.12 (25)	−0.43 ± 0.15 (13)	−1.12 ± 0.18 (21)
B8	−0.12 ± 0.08 (82)	−0.29 ± 0.23 (12)	−0.95 ± 0.13 (44)

with nonstandard spectra; i.e., those with "n" or "e" indices in their spectral types. We analyzed such stars separately. This left us with a total of 935 normal stars, whose absolute magnitudes we derived from their Hipparcos trigonometric parallaxes.

We took into account interstellar extinction as follows. We determined the color excesses of the sample stars in two ways: (1) using the intrinsic color indices and (2) using the so-called Q method, taking into account the stars' luminosity classes in both cases. We included in our sample only stars with published luminosity-class estimates, since color index depends strongly on luminosity class within the given spectral subtypes. We adopted the intrinsic $(B–V)_0$ color indices and Q_{UBV} indices from the corresponding tables in the monograph of Straizys [6]. Stars for which the two methods yielded discrepant color indices (i.e., differing by more than $0^m.1$) were excluded from the sample due to the possibility of large photometric errors or variability. We adopted a total-to-selective extinction ratio of $R = A_V/E(B–V) = 3.3$ for all stars as the mean value for the spectral-type range considered [6]. We did not allow for the dependence of R on Galactic coordinates, since substantial deviations of R from its mean value occur only in limited areas of the sky, where no heliocentric distance dependences of this parameter have been investigated.

We then averaged the resulting absolute magnitudes over each spectral subtype/luminosity class combination with weights inversely proportional to the fractional errors of the trigonometric parallaxes. We excluded all absolute-magnitude estimates that deviated by more than 2σ from the mean, in order to minimize distortion of the distributions due to errors in the assigned spectral subtypes and, more importantly, in the assigned luminosity classes. The resulting absolute magnitudes are summarized in Table 1, whose columns give the mean M_V values derived from the Hipparcos trigonometric parallaxes for the corresponding spectral subtype/luminosity class combination, followed by the standard errors of these quantities. The number of stars used to determined each particular mean M_V is given in parentheses.

Table 1 shows that the Hipparcos data are sufficient to achieve an accuracy of $0^m.1$ for certain spectral subtype/luminosity class combinations, whereas additional data are required for most others, as well as for O stars and supergiants.

3. LUMINOSITY CALIBRATION FOR O AND B STARS OF ALL SPECTRAL SUBTYPES AND LUMINOSITY CLASSES

To extend the calibration toward the domain of supergiants and O stars and refine it for some other types of stars, we decided to use data for open-cluster stars. To this end, we used the Lausanne database created under the supervision of J.-C. Mermilliod to select clusters for which spectral types were determined both for stars in the intervals listed in Table 1 and for stars lying outside these intervals. We used the former data to determine the distances to the open clusters using the spectroscopic-parallax method (to ensure consistency with the distance scale based on the Hipparcos parallaxes), and the latter data to extend the calibration toward other spectral subtypes and luminosity classes. To extend the calibration, we selected a total of 49 clusters, each containing at least four stars whose absolute magnitudes could be determined based on the data in Table 1. We determined the distances to these clusters using the spectroscopic-parallax method.

Figure 1 compares the resulting distance moduli to those given in the latest version of the Homogeneous Catalog of Open Cluster Parameters [9], where we have corrected the distance moduli from [9] by adding a $-0^m.15$ offset, which we inferred from trigonometric parallax data in [3]. It is evident from the figure that the distance scale based on Table 1 coincides with the

corrected distance scale of [9]. Therefore, we conclude that we can use the open cluster stars to expand the calibration. Table 2 summarizes the results of the calibration including the additional open-cluster stars.

Note that we have added cluster stars only for those entries of the table where we considered the previous calibration to be insufficiently accurate. A comparison of the values presented in Tables 2 and 1 clearly shows that our use of the cluster stars enabled a substantial improvement of the accuracy of the calibration in terms of the random errors for many spectral subtype/luminosity class combinations without introducing appreciable systematic errors.

4. CALIBRATION OF THE STRÖMGREN β INDICES

Another way to estimate the absolute magnitudes of O and B stars is to use the luminosity dependence of the β index of the Strömgren photometric system [6]. Determining the absolute magnitudes based on the β indices has an important advantage over the use of the spectroscopic-parallax method, since β is a continuous function of absolute magnitude, whereas the spectroscopic parallax is a discrete measure. To calibrate the $M_V(\beta)$ dependence for B stars, we used stars with nonpeculiar spectral types and Hipparcos trigonometric parallaxes. Our sample contains a total of 791 stars with β indices adopted from [7]. These stars have absolute magnitudes M_V (derived from Hipparcos trigonometric parallaxes) ranging from $-8\overset{m}{.}4$ to $+1\overset{m}{.}1$ and β indices in the range from 2.42 to 2.88. Since our sample contains stars spanning a wide range of interstellar extinctions, we tried to investigate the possible dependence of the calibration on the interstellar extinction by including the corresponding terms in our regression models.

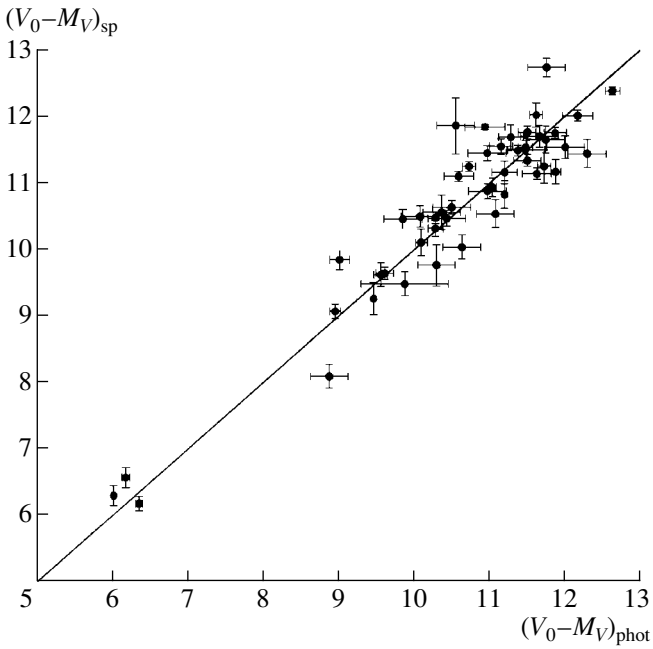

Fig. 1. Comparison of open-cluster distance moduli determined using spectroscopic-parallax and photometric methods.

When deriving a formula relating M_V to β, we computed the coefficients for three least-squares regression models. We analyzed three models rather than one to

Table 2. Mean absolute magnitudes of O and B stars

Sp	Luminosity class V	Luminosity class IV	Luminosity class III	Luminosity class II	Luminosity class Ib	Luminosity class Ia
O6	−5.38 ± 0.16 (6)	–	−5.67 ± 0.14 (5)	–	–	–
O7	−4.80 ± 0.13 (14)	–	−5.20 ± 0.52 (5)	–	–	–
O8	−4.66 ± 0.18 (21)	–	−4.67 ± 0.37 (7)	–	–	
O9	−4.18 ± 0.25 (20)	–	−4.66 ± 0.30 (10)	–	–	–
O9.5	−3.81 ± 0.14 (21)	–	−4.34 ± 0.31 (12)	−4.65 ± 0.27 (6)	−4.52 ± 0.55 (4)	−6.69 ± 0.95 (3)
B0	−3.55 ± 0.15 (32)	−3.59 ± 0.21 (13)	−4.12 ± 0.25 (9)	−4.28 ± 0.21 (23)	−5.15 ± 0.24 (16)	−6.11 ± 0.52 (3)
B0.5	−3.27 ± 0.16 (38)	−3.98 ± 0.23 (10)	−3.67 ± 0.23 (20)	–	–	–
B1	−2.84 ± 0.10 (69)	−3.52 ± 0.29 (10)	−3.89 ± 0.20 (17)	−4.28 ± 0.16 (21)	−4.61 ± 0.18 (25)	−6.51 ± 0.18 (4)
B1.5	−2.24 ± 0.11 (54)	−3.00 ± 0.14 (9)	−3.57 ± 0.22 (7)	–	–	–
B2	−2.11 ± 0.08 (115)	−2.61 ± 0.09 (66)	−2.79 ± 0.20 (27)	−3.50 ± 0.17 (24)	−4.70 ± 0.29 (10)	−6.77 ± 0.45 (4)
B3	−1.56 ± 0.06 (128)	−1.95 ± 0.11 (52)	−2.34 ± 0.15 (36)	−2.79 ± 0.45 (11)	−5.16 ± 0.45 (4)	−6.66 ± 0.15 (7)
B4	−1.38 ± 0.13 (34)	−1.15 ± 0.10 (15)	−2.01 ± 0.57 (7)	–	–	–
B5	−1.20 ± 0.08 (65)	−1.33 ± 0.18 (17)	−1.46 ± 0.17 (31)	−2.60 ± 0.84 (8)	−4.80 ± 0.42 (6)	−6.54 ± 0.63 (4)
B6	−0.86 ± 0.13 (31)	−1.06 ± 0.20 (20)	−1.43 ± 0.16 (17)	−1.39 ± 0.59 (4)	–	–
B7	−0.58 ± 0.12 (25)	−0.45 ± 0.13 ()15	−1.12 ± 0.18 (21)	−2.16 ± 0.51 (6)	–	–
B8	−0.12 ± 0.08 (82)	−0.31 ± 0.19 (16)	−0.95 ± 0.12 (50)	−1.22 ± 0.41 (5)	−3.87 ± 0.27 (4)	−6.34 ± 0.31 (3)

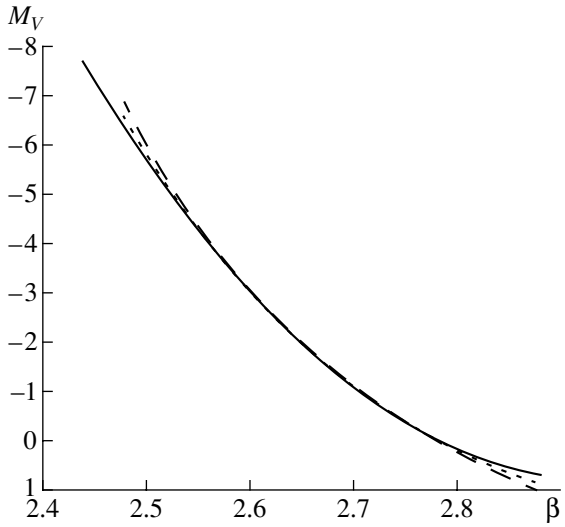

Fig. 2. Comparison of three regression models for the $M_V - \beta$ relation.

minimize errors due to possible inadequate model selection. We obtained the following formulas based on all the sample stars.

Model I:

$$M_V = -28.18 - 0.42A_V + 61.33(\beta - 2) - 32.37(\beta - 2)^2, \quad \sigma = 0.70 \qquad (1)$$

with standard errors of the coefficients equal 1.19, 0.05, 3.44, and 2.47, respectively;

Model II:

$$M_V = -7.50 - 0.42A_V + 57.60e^{-(\beta-2)} - 90.09e^{-2(\beta-2)}, \quad \sigma = 0.70 \qquad (2)$$

with standard errors of the coefficients equal 2.50, 0.05, 9.96, and 9.90, respectively;

Model III:

$$M_V = 9.02 - 0.43A_V - 6.46(\beta - 2)^{-1} - 0.45(\beta - 2)^{-2}, \quad \sigma = 0.70 \qquad (3)$$

with standard errors of the coefficients equal 1.12, 0.05, 1.52, and 0.51, respectively.

As we can see, all three models yield virtually identical standard errors σ for the residuals, so that none of them can be discarded. However, when deriving the coefficients of the regression equations, we ignored one fact that could prove to be very important. Least-squares estimates are unbiased only if all the errors are concentrated on the left-hand sides of the equations. However, in our case, we have, on the one hand, significant errors in the absolute magnitudes M_V derived from the trigonometric parallaxes, and, on the other hand, errors of about 0.015 in the published β indices. Moreover, the sample could contain stars with undetected hydrogen emission features, which decrease the measured β indices. It is known (see, e.g., [8]) that the estimates of regression-model parameters can be biased in this case, with the actual biases depending on the parameters of the distributions of the errors in the factors and the left-hand sides of the equations. Unfortunately, estimating the corresponding corrections for multifactor models is hindered by the fact that the corresponding methods have not been fully developed. Numerical simulations are also difficult to perform, due to difficulties in modeling errors in absolute magnitudes (M_V) derived from trigonometric parallaxes with unequal accuracies and the impossibility of determining the parameters of the error distributions for A_V and β for a particular sample. Therefore, we artificially decreased the scatter in the residuals by gradually excluding stars with the highest residuals. In all three models, we excluded stars with residuals exceeding $2\overset{m}{.}0$, which, in our case, corresponds to approximately 3σ. This yielded the following relations.

Model I:

$$M_V = -29.64 - 0.32A_V + 65.34(\beta - 2) - 35.08(\beta - 2)^2, \quad \sigma = 0.63 \qquad (4)$$

with standard errors of the coefficients equal 1.11, 0.05, 3.19, and 2.29, respectively;

Model II:

$$M_V = -9.79 - 0.30A_V + 67.36e^{-(\beta-2)} - 100.44e^{-2(\beta-2)}, \quad \sigma = 0.63 \qquad (5)$$

with standard errors of the coefficients equal 2.32, 0.05, 9.27, and 9.23, respectively;

Model III:

$$M_V = 6.88 - 0.30A_V - 3.39(\beta - 2)^{-1} - 1.54(\beta - 2)^{-2}, \quad \sigma = 0.64 \qquad (6)$$

with standard errors of the coefficients equal 1.10, 0.05, 1.49, and 0.50, respectively. Again, all three models yield virtually identical dispersions in the residuals. Note that, although the coefficient of A_V has decreased, it remains statistically significant and has the same value in all three models. The plots of the dependences determined by these models in Fig. 2 show that the models are in good agreement throughout the range of β indices of interest to us. Recall that we derived these relations using Hipparcos trigonometric parallaxes as the only source of the absolute magnitudes.

To refine the calibration for luminous stars, we used O stars and supergiants in open clusters. We added a total of 103 stars to our sample. A procedure similar to that described above yielded the following relations.

Model I:

$$M_V = -35.51 - 0.54A_V + 82.01(\beta - 2) - 46.78(\beta - 2)^2, \quad \sigma = 0.61 \tag{7}$$

with standard errors of the coefficients equal to 1.07, 0.03, 3.08, and 2.22, respectively;

Model II:

$$M_V = -22.95 - 0.52A_V + 120.79^{-(\beta-2)} - 154.38e^{-2(\beta-2)}, \quad \sigma = 0.61 \tag{8}$$

with standard errors of the coefficients equal to 2.27, 0.03, 9.02, and 8.97, respectively;

Model III:

$$M_V = 0.56 - 0.51A_V + 5.49(\beta - 2)^{-1} - 4.63(\beta - 2)^{-2}, \quad \sigma = 0.61 \tag{9}$$

with standard errors of the coefficients equal to 1.06, 0.03, 1.43, and 0.48, respectively.

Note that, in this case, we excluded from our sample stars with residuals exceeding $1\overset{m}{.}8$, leading to the smaller dispersions in the residuals compared to the previous case. The resulting dispersions in the residuals show that, in spite of the wider β interval considered, all the models remain adequate. It is interesting that the coefficient of A_V increased, suggesting an appreciable correlation between M_V and A_V and, consequently, between A_V and β for the stars in our sample. Indeed, the corresponding coefficient of the correlation matrix is equal to –0.51. This correlation for our sample of stars could reflect the fact that, on average, more luminous stars are located at greater heliocentric distances and have greater reddenings than less luminous stars. Therefore, the above results should not be interpreted as implying a strong dependence of β on the interstellar extinction. The solution for model III obtained for the expanded sample including cluster stars and without the A_V term has the form

$$M_V = -3.55 + 11.53(\beta - 2)^{-1} - 6.87(\beta - 2)^{-2}, \quad \sigma = 0.63. \tag{10}$$

The increase of the dispersion prevents us from unambiguously deciding whether the A_V term should be included in the model: the dispersion in the residuals of (10) does not significantly exceed the corresponding dispersion for (9). It is well known that adding an arbitrary factor to a regression model decreases the dispersion in the residuals. This leads us to conclude that the index β is independent of interstellar extinction for small interstellar extinctions ($A_V < 2\overset{m}{.}0$ m).

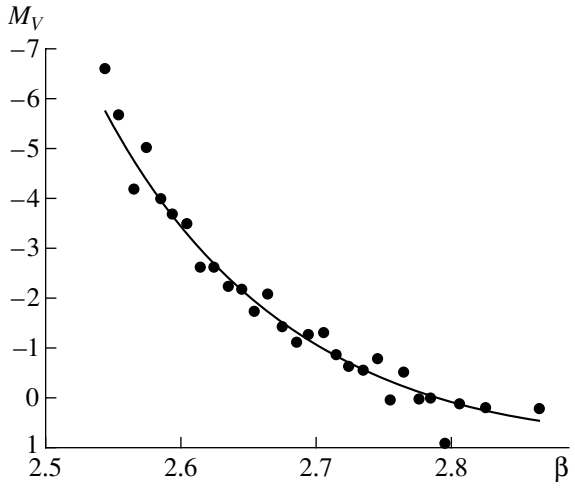

Fig. 3. $M_V - \beta$ relation determined from the loci of maxima (modes) of the β frequency distributions (see text).

Further, we used a somewhat modified technique to determine the $M_V - \beta$ relation. We separated our sample into β bins with widths of 0.01, and constructed the frequency distribution of the absolute magnitudes for each bin. We then determined the modes of these distributions. Figure 3 shows the resulting dependence (dots) plotted along with the least-squares fit

$$M_V = -7.19 + 16.54(\beta - 2)^{-1} - 8.58(\beta - 2)^{-2}, \quad \sigma = 0.24. \tag{11}$$

Of the three regression relations considered here, we adopted the power-law model, since it yielded a somewhat lower dispersion in the residuals and better fits the data points corresponding to the most luminous stars in Fig. 3. The solution based on the modes of the distributions for the β bins is better than all the previous solutions, due to the reduced effect of outliers, especially of stars with undetected hydrogen emission.

We introduced no separate term to allow for the possible dependence of M_V on color index within a given subtype, since any temperature index should be strongly correlated with β and M_V.

Our preferred relation for the determination of absolute magnitudes is (11), which is least affected by systematic errors and possible biases due to stars with undetected emission lines. However, due to the small number of stars in the extreme β bins, Eq. (10) is preferable at the edges of the overall β range.

5. LUMINOSITY CALIBRATION FOR STARS WITH "n" AND "e" INDICES

Among the B stars there are objects whose spectral lines are broadened, probably due to rapid rotation. These objects, whose spectral types include the index

Table 3. Mean absolute magnitudes of Bn stars

Sp	M_V	N	$(B–V)_0$	$(B–V)_0$(Str)
B0	−4.04 ± 0.25	3	−0.24 ± 0.02	−0.30
B1	−3.47 ± 0.24	13	−0.24 ± 0.01	−0.27
B2	−2.57 ± 0.20	17	−0.24 ± 0.01	−0.25
B3	−1.51 ± 0.25	13	−0.16 ± 0.01	−0.21
B4	−1.96 ± 0.26	4	–	–
B5	−1.29 ± 0.17	14	−0.12 ± 0.02	−0.17
B6	−0.69 ± 0.19	8	−0.14 ± 0.01	−0.14
B7	−0.08 ± 0.25	6	−0.12 ± 0.01	−0.13
B8	−0.19 ± 0.10	25	−0.10 ± 0.01	−0.10

"n," are primarily of luminosity class V. This index is rarely found in stars of other luminosity classes, and the number of such objects is clearly insufficient to determine their mean absolute magnitudes. The processes broadening the spectral lines could also result in the luminosities of these stars differing from those of normal stars.

We used both Hipparcos catalog objects and cluster stars to determine the mean absolute magnitudes of On and Bn stars. The first three columns of Table 3 summarize the resulting mean M_V values. These columns present (1) the spectral subtype (only for stars of luminosity class V, since there are very few such stars in other luminosity classes), (2) the estimated mean absolute magnitude and its standard error, and (3) the number of stars used. The intrinsic color indices of such stars, required to estimate the interstellar extinctions, can be determined only from the cluster stars. The corresponding clusters should exhibit no differential extinction, so that the mean $(B–V)_0$ color excess averaged over the cluster can be used to correct for interstellar extinction. The mean $(B–V)_0$ indices and their standard errors are summarized in the fourth column of Table 3 and, for comparison, the fifth column gives the intrinsic colors adopted from the corresponding table of Straizys [6] for normal B stars. It is evident that the differences between the color indices of On and Bn stars and those of normal stars are barely discernible for late B subtypes, and gradually increase toward earlier subtypes.

A comparison of the data in Table 3 with the absolute magnitudes of normal B stars shows that Bn stars are somewhat brighter than normal stars.

We now turn to the determination of absolute magnitudes of stars with hydrogen line emission. Emission-line stars are marked by the index "e" in their spectral types. Note that spectroscopic parallaxes provide the only means for estimating the absolute magnitudes of these stars. The reason is that the index β cannot be applied in this case, since it is appreciably decreased by emission features. Unfortunately, there are few emission-line stars in clusters with weak differential extinction, and we could estimate the intrinsic color indices only for a few B subtypes. The mean color indices for B1Ve stars are $(B–V)_0 = –0.19 \pm 0.02$ (10 stars); for B2Ve stars, $(B–V)_0 = –0.19 \pm 0.02$ (11 stars); for B3Ve stars, $(B–V)_0 = –0.19 \pm 0.01$ (3 stars); and for B6Ve stars, $(B–V)_0 = –0.11 \pm 0.06$ (3 stars). B emission-line stars are, on average, $0^m.03$ redder than normal stars of the same spectral subtypes, and we accordingly applied this correction to estimate the color excesses of such stars. The resulting mean absolute magnitudes are summarized in Table 4, whose layout is similar to that of

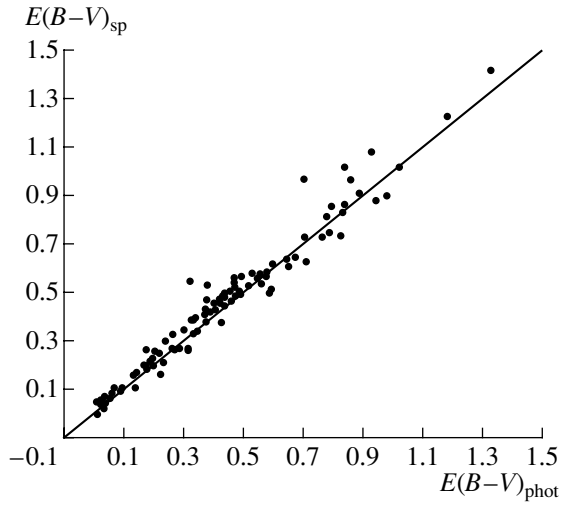

Fig. 4. Comparison of the mean color excesses of 106 young open clusters determined using spectroscopic and photometric methods.

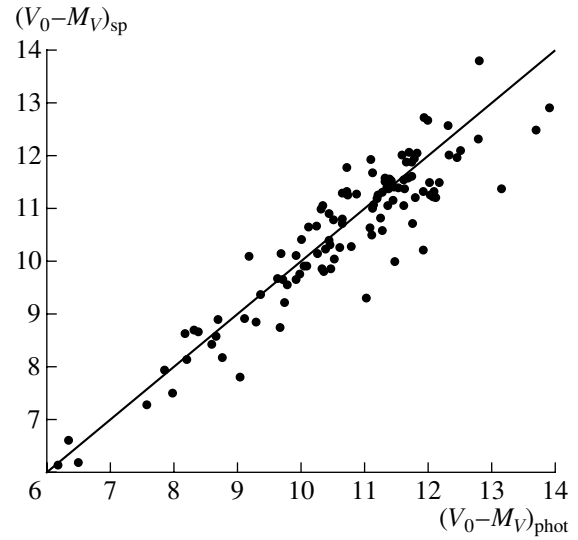

Fig. 5. Comparison of distance-modulus estimates for 106 young open clusters based on photometric and spectroscopic-parallax methods.

Table 4. Mean absolute magnitudes of Be stars

Sp	Luminosity class V	Luminosity class IV	Luminosity class III
B0	–	−4.04 ± 0.11 (5)	–
B1	−2.97 ± 0.23 (14)	–	–
B2	−2.56 ± 0.17 (29)	−3.21 ± 0.27 (5)	−2.81 ± 0.77 (4)
B3	−2.69 ± 0.27 (12)	−3.33 ± 0.64 (4)	–
B5	−1.64 ± 0.26 (10)	–	–
B6	−0.76 ± 0.15 (31)	−2.37 ± 0.39 (4)	–
B7	−1.56 ± 0.31 (25)	−0.85 ± 0.39 (4)	–
B8	−0.69 ± 0.15 (10)	–	–

Tables 1 and 2. Despite the small number of emission-line stars in our sample, the data of Table 4 indicate that emission-line stars are more luminous than normal stars, and that their absolute magnitudes are, on average, $0^m.5$ lower than those of normal stars.

6. DISTANCES TO THE YOUNGEST OPEN CLUSTERS

Having derived the calibrations for normal, rapidly rotating, and emission-line O and B stars, we determined the distances to the maximum possible number of open clusters using the spectroscopic-parallax method. We included all open clusters with at least three stars for which the Lausanne database gives two-dimensional spectral classifications, so that their absolute magnitudes can be determined using Tables 2–4. We found a total of 106 such clusters. Figures 4 and 5 compare our mean color excesses and distance moduli, respectively, with those of [9]. Naturally, the accuracies of the distance moduli differ from cluster to cluster, and some data points in Fig. 3 lie far from the 45° line. However, on average, the two sets of estimates are in satisfactory agreement.

We included the resulting color-excess and distance-modulus estimates in the Homogeneous Catalog [9] in order to improve the mean accuracy of the distance determinations for the youngest open clusters. The latest version of the catalog (Version 2.1), including the results of this paper, can be obtained from the authors at the e-mail address Alexander.Loktin@usu.ru.

7. CONCLUSIONS

The calibrations of the spectroscopic parallaxes and β indices reported in this paper are based on extensive samples, are highly trustworthy, and were derived from direct trigonometric parallax measurements. The calibrations for Bn and Be stars will enable the use of a large number of stars that were previously neglected or had incorrect absolute magnitudes in investigations of Galactic structure and kinematics.

The good agreement, on average, between the open-cluster distances derived using the spectroscopic parallaxes and the photometric method support the conclusion of Pinsonneault *et al.* [11] that the latter method is highly trustworthy. Doubts about the reliability of the photometric method raised after the first determinations of distances to nearby open clusters based on Hipparcos trigonometric parallaxes (see, e.g., [10]) should be readdressed to the Hipparcos parallax system, which apparently is not free of systematic errors in some areas of sky, in particular, in the region of the Pleiades cluster.

ACKNOWLEDGMENTS

We are grateful to A. Vasilevskiĭ for useful discussions of the statistical methods used in this work.

REFERENCES

1. P. N. Kholopov, *Star Clusters* (Nauka, Moscow, 1981).
2. N. Robishon, F. Arenou, J.-C. Mermilliod, and C. Turon, Astron. Astrophys. **345**, 471 (1999).
3. A. V. Loktin and G. V. Beshenov, Pis'ma Astron. Zh. **27** (6), 450 (2001) [Astron. Lett. **27**, 386 (2001)].
4. C. Jaschek, A. Valbousquet, and F. Oschenbein, Astron. Astrophys. **312**, 815 (1996).
5. D. Hoffleit and W. H. Warren, Jr., *The Bright Star Catalogue* (Yale Univ. Obs., New Haven, 1991, 5th revised ed.).
6. V. Straizys, *Multicolor Stellar Photometry* (Mokslas, Vilnius, 1977; Pachart Publ. House, Tucson, 1992).
7. B. Hauck and J.-C. Mermilliod, Astron. Astrophys., Suppl. Ser. **86**, 107 (1990).
8. I. Vuchkov, L. Boyadzhiev, and E. Solakov, *Applied Linear Regression Analysis* [in Russian] (Finansy i Statistika, Moscow, 1987).
9. A. V. Loktin, T. P. Gerasimenko, and L. K. Malisheva, Astron. Astrophys. Trans. (in press).
10. J.-C. Mermilliod, C. Turon, N. Robichon, *et al.*, Eur. Space Agency, Spec. Publ. **ESA SP-402**, 643 (1997).
11. M. H. Pinsonneault, J. Stauffer, D. R. Soderblom, *et al.*, Astrophys. J. **504**, 170 (1998).

Translated by A. Dambis

Astronomy Reports, Vol. 45, No. 9, 2001, pp. 718–728. Translated from Astronomicheskiĭ Zhurnal, Vol. 78, No. 9, 2001, pp. 827–838.

Levels of Coronal and Chromospheric Activity in Late-Type Stars and Various Types of Dynamo Waves

E. A. Bruevich[1], M. M. Katsova[1], and D. D. Sokolov[2]

[1]*Sternberg Astronomical Institute, Universitetskiĭ pr. 13, Moscow, 119899 Russia*

[2]*Faculty of Physics, Moscow State University, Vorob'evy gory, Moscow, 119899 Russia*

Received January 9, 2001

Abstract—We analyze the X-ray emission and chromospheric activity of late-type F, G, and K stars studied in the framework of the HK project. More powerful coronas are possessed by stars displaying irregular variations of their chromospheric emission, while stars with cyclic activity are characterized by comparatively modest X-ray luminosities and ratios of the X-ray to bolometric luminosity L_X/L_{bol}. This indicates that the nature of processes associated with magnetic-field amplification in the convective envelope changes appreciably in the transition from small to large dynamo numbers, directly affecting the character of the $(\alpha - \Omega)$ dynamo. Due to the strong dependence of both the dynamo number and the Rossby number on the speed of axial rotation, earlier correlations found between various activity parameters and the Rossby number are consistent with our conclusions. Our analysis makes it possible to draw the first firm conclusions about the place of solar activity among analogous processes developing in active late-type stars. © *2001 MAIK "Nauka/Interperiodica".*

1. INTRODUCTION

The first systematic investigations of solar-type activity in other stars were begun in the middle of the 1960s by Wilson at Mt. Wilson Observatory, and have continued since that time in the framework of the so-called "HK project" [1, 2]. Observational studies of chromospheric activity include determinations of the ratio of the central fluxes of the Ca II H and K lines (3968 Å and 3934 Å, respectively) to the flux in the nearby continuum (4001 Å and 3901 Å)—the quantity $S_{Ca\ II}$ (the mean ratio for the two lines). This approach has provided a uniform description of levels of chromospheric activity and made it possible to monitor such activity over several decades.

Several dozen fairly bright stars with spectral types from F2 to M2, in which it was believed solar-type magnetic activity could develop, were chosen for study. Beginning in 1977, the number of program stars grew to 111, and this database became fundamental for investigations of chromospheric variability on time scales from decades down to the rotational periods of the stars.

The quantity $S_{Ca\ II}$ (further S) proved to be a good indicator of chromospheric activity [3]. Objects with both large and small values of S are encountered among stars with similar spectral types. Baliunas *et al.* [3] attributed these differences in the level of chromospheric activity primarily to differences in age, at least in the case of single stars. The mean (for the given interval of effective temperatures) value of S varies somewhat with spectral type.

It has now become clear that the processes giving rise to the complex of activity phenomena manifest in the interiors—convective zones—of stars encompass virtually the entire atmosphere from the photosphere to the corona. The first results on variations of the optical continuum of stars in the HK project over roughly the last ten years are presented in [4]; results for some BY Dra stars (spotted red dwarfs) are presented in [5, 6]. In general, these data testify that the photospheric activity of these stars resembles that of the Sun, but, in some cases, the relative areas occupied by star spots are two to three orders of magnitude larger than on the Sun at the solar-cycle maximum. Data that can be used to compare the properties of activity in different levels of the outer atmospheres of specific stars and the Sun are already available.

Long-term, uniform data sets on the coronal fluxes of specific late-type stars are not yet available, except for the Sun. However, measurements of the soft X-ray emission of more than 1000 active late-type stars have been made. These are primarily data obtained for nearby, bright stars by the ROSAT satellite at 0.1–2.4 keV [7, 8]. The ROSAT data confirmed and expanded the general results obtained by the Einstein observatory concerning the dependence of the X-ray luminosity on the speed of axial rotation, at least for main-sequence stars; the saturation of the X-ray luminosity relative to the bolometric luminosity L_X/L_{bol} for red dwarfs (discovered by Vilhu and Walter [9]); and the presence of high-temperature patches in the coronas of some late-type stars [10]. Important information has been obtained for active late-type stars in RS CVn binary systems, enabling in a num-

1063-7729/01/4509-0718$21.00

ber of cases a better understanding of the regularities observed for active processes on single late-type stars.

An analysis of the X-ray emission of stellar coronas based on Einstein data was presented by Katsova *et al.* [11], who determined the densities at the bases of the uniform coronas of dwarfs of various spectral types. The coronas with the highest densities are possessed by the most active red dwarfs, with spectral types K5–M3; their coronal densities are an order of magnitude higher than the corresponding solar value.

The X-ray emission of HK-project stars detected by ROSAT was considered by Hempelmann *et al.* [12], who compared the X-ray emission of late-type stars with constant levels of Ca II line emission and with regular and irregular (chaotic) long-term variations of this emission. They found that the distribution of X-ray fluxes associated with the stellar coronas is appreciably different for stars with variable Ca II line fluxes: on average, stars with irregular chromospheric activity have higher X-ray fluxes. Hempelmann *et al.* [12] attempted to relate this result to a dependence of coronal activity on the Rossby number, and to the possible existence of a Maunder minimum at the current epoch for some quiescent late-type stars.

Uniform X-ray catalogs of the nearest bright stars are now available [7, 8], as well as the results of new analyses of long-term chromospheric and photospheric activity. Therefore, it is valuable to investigate the coronal activity of HK-project stars with different types of cycles and compare the results with the main expectations of dynamo theory. This can provide information about the effectiveness of the dynamo mechanism on F–K stars with differing levels of activity.

2. CHROMOSPHERIC ACTIVITY AND POSITION OF A STAR ON THE HERTZSPRUNG–RUSSELL DIAGRAM

In most stars with variable Ca II line emission, the calcium-line flux shows modulations with the period of rotation of the star. This rotational modulation virtually disappears for stars of similar spectral types with the smallest and largest values of S, due to either a lack of active regions on these stars or, on the contrary, the presence of a very large number of active regions more or less uniformly distributed over the surface (if the stellar rotational axis is perpendicular to the line of sight, this implies a uniform distribution in longitude).

Observations carried out over the past 35 years have enabled the detection of long-term variations of this activity index for selected variable stars. Roughly one-third of the studied stars show no periodicities in these variations (this type of chromospheric variability is designated after [3] as "Var"). Long-term periodicity in variations of S were directly detected in 50 of the 111 HK-project stars. Applying spectral analyses to the long-term data on chromospheric activity made it possible to determine for each star the degree to which cycles analogous to the solar cycle were present and well defined. The periods for the cycles were from several years to decades.

Using formal statistical criteria, Baliunas *et al.* [3] categorized stars into four groups according to the degree to which their chromospheric-activity cycles were well defined: "Excellent," "Good," "Fair," and "Poor." This division was carried out based on the probability that the periodicity for stars in a given group was not associated with Gaussian noise. A quantitative index for this division is the false alarm probability (FAP), or the probability that the observed behavior is the result of Gaussian noise; for "Excellent" cycles FAP $< 10^{-9}$, for "Good" cycles $10^{-9} <$ FAP $< 10^{-5}$, for "Fair" cycles $10^{-5} <$ FAP $< 10^{-2}$, and for "Poor" cycles $10^{-2} <$ FAP $< 10^{-1}$. A standard statistical treatment indicates that the critical value of the FAP for which the null hypothesis of the presence of cyclicity can be rejected is about 0.05. Formally, this means that one out of 20 cases that are in fact due to Gaussian noise will be taken to represent cyclic behavior. However, between these extreme cases of pure Gaussian noise and strictly periodic variations, there are many different possible types of variability that formally contain some periodic components, which can be revealed by Fourier analysis. In some cases, it is also important to accurately exclude harmonics. Therefore, a trustworthy identification of cycles requires the application of not one but several methods and criteria. Recent progress in finding solutions to this problem has come about with the development of wavelet analysis, which enables the analysis of non-uniform time series. In summary, the FAP can serve as a certain relative measure of the extent to which cyclic variations are well defined. The broad range for the Good group ($10^{-9} <$ FAP $< 10^{-5}$) essentially means that there is already a watershed here dividing cycles that can be distinguished with certainty from cases with more complex activity on time scales of several years.

In their analysis, Baliunas *et al.* [3] note that cycles are more easily distinguished for K stars and for G stars with small S values, while the chromospheric activity of some F stars is higher, but more chaotic (cyclicity is virtually absent). This result can be represented pictorially by plotting the HK-project objects with chromospheric activity on a Hertzsprung–Russell diagram. We determined the stars' bolometric luminosities using the fundamental parameters given in [13, 14] (see Tables 1 and 2). Figure 1 illustrates the behavior of the stars with chromospheric activity by plotting their bolometric luminosities (in solar units) $\log L_{\rm bol}/L_\odot$ as a function of their effective temperatures $\log T_{\rm eff}$. Here, we have drawn the conventional zero-age main sequence and two evolutionary tracks demonstrating the arrival to and departure from the main sequence of solar-mass stars [15].

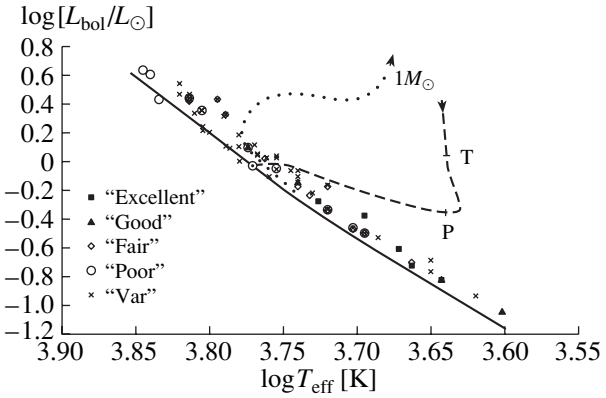

Fig. 1. Position in the Hertzsprung–Russel diagram of late-type stars with chromospheric activity included in the HK project. The various symbols correspond to different manifestations of chromospheric activity, from chaotic irregular variations (crosses) to cyclic activity (filled squares). The solid curve shows the main sequence; the dashed curve shows the track for the arrival to the main sequence of a solar-mass star from the evolutionary status of T Tauri (T) through the post-T Tauri stage (P). The dotted curve shows the departure of a star of the same mass from the main sequence. The position of the Sun is marked with a solar sign. A number of stars with the same spectral type are superposed, so that the number of stars in the diagram is fewer than the number in Tables 1 and 2.

We can see that these stars are located fairly close to the main sequence. This reflects the fact that the youngest stars, with spectral types later than F0, and evolved objects were not considered either in the HK project or in the current paper. However, there is some scatter in the ages of the stars studied, which may affect their activity levels to some extent. Our independent analysis and the analysis of [3] show that the cyclicity of long-term chromospheric variations begins to be manifest in stars of spectral type G0, and is clearly defined in spotted K stars, while this activity is irregular in F stars. Recent data on chromospheric activity and new observations of long-term variations in the optical continuum of the HK-project stars enable us to refine this conclusion.

Beginning with [16], the idea has been developed that all these late-type stars can be divided into two groups according to their activity levels. This division becomes more obvious when considering the calcium emission fluxes. In other words, in place of the index S, the flux of a star in both calcium emission lines normalized to the bolometric luminosity, $\log R'_{HK}$ [17], was introduced as a measure of activity, and began to be used in subsequent studies. In relations plotting $\log R'_{HK}$ as functions of spectral type or other stellar parameters, two groups can clearly be distinguished, with stars with well defined cycles being less active. This tendency has been traced in several studies, in particular in [4], which presents the results of ten years of optical-continuum observations of a number of HK-project stars. It has also become possible to compare long-term activity at the chromospheric and photospheric levels, which increases our ability to determine the extent to which variations display well defined cyclicity.

Note that the difference in the activity levels of these two groups of stars depends on their speeds of axial rotation, which also indirectly reflects the influence on rotation of several factors, first and foremost age. All these considerations lead us to believe that cycles can be distinguished with a high degree of certainty only for stars in the Excellent group. We have already noted that stars in the Good group have FAPs that cover a very wide range (four orders of magnitude). This means that this group includes both stars with well defined cycles (with periods, however, that have not been strictly maintained over the forty years of observations) and stars with irregular variations of their chromospheric and photospheric emission. Note that Baliunas *et al.* [3] ascribe only 13 stars, including the Sun, to the "Excellent" group; well defined cycles are observed in only a few of the 8 stars in the Good group.

3. X-RAY EMISSION AND CYCLIC ACTIVITY OF LATE-TYPE STARS

To analyze the coronal emission of late-type stars, we used ROSAT observations of more than 1500 nearby, bright main-sequence stars and subgiants, contained in the two X-ray catalogs of Hünsch *et al.* [7, 8]. Both catalogs present measurements in the 0.1–2.4 keV range carried out either as part of the ROSAT all-sky survey or during directed observations. We were able to find X-ray flux measurements for 78 of the HK-project stars. We used the data for these objects from [7, 8] reduced to a unified system. In several cases when the total X-ray flux from a binary system was registered (HD 131156AB, HD 165341AB, HD 201091, and HD 201092, HD 219834AB), we ascribed this flux equally to both components if their speeds of axial rotation were essentially the same. In two such cases, we divided the total flux of the binary in proportion to the rotational speeds of the two stars. Note also that the X-ray luminosity of HD 81809 may be overestimated, since this is a spectroscopic binary.

The X-ray luminosities L_X for the HK-project stars (when observed) are presented in Table 1 (for stars with more or less regular chromospheric activity) and Table 2 (for stars with chaotic variability). These tables also list a number of other physical characteristics of these stars: their color indices, spectra, periods of axial rotation P_{rot} [18], bolometric luminosities L_{bol}, etc. For the Sun, we present the X-ray luminosity in the ROSAT band for epochs of high activity ($L_X = 5 \times 10^{26}$ erg/s) [19].

Figure 2a presents the X-ray luminosities of the HK-project stars and the Sun together with characteristics of their chromospheric activity as functions of their rotational periods. The main tendency for more rapidly rotating late-type stars to possess higher X-ray fluxes—first discovered in Einstein data [20]—can clearly be

Table 1. Stars with regular chromospheric activity

HD	Gliese	Star	$B–V$	Spectrum	$\log L_X$ [erg/s]	P_{rot}, day	P_{cyc}, year	$\log L_X$ [erg/s]	$D/D_\odot$
				"Excellent"					
		Sun	0.66	G2 V	26.70	25	10.0	33.58	1.00
4628			0.88	K4 (K2V)	27.59	39	8.4	33.33	0.41
10476	68	107 Psc	0.84	Kl V		35	9.6	33.37	0.51
16160			0.98	K3 V	27.26	48	13.2	33.22	0.27
26965		o^2 Eri A	0.82	Kl V	27.61	43	10.1	33.38	0.34
32147			1.06	K5 V	27.18	47	11.1	33.18	0.28
81809			0.64	G2 V	28.10	41	8.2	33.59	0.37
103095	451	Grmb 1830	0.75	G8 VI		31	7.3	33.44	0.65
152391	641	V 2292 Oph	0.76	G7 V	28.94	11	10.9	33.42	5.17
160346	688		0.96	K3 V	27.48	37	7.0	33.25	0.46
166620	706		0.87	K2 V		43	15.8	33.34	0.34
201091	820 A	61 Cyg A	1.18	K5 V	27.15	35	7.3	33.08	0.51
219834B	894.2	94 Aqr B	0.91	K2 V	27.58	43	10.0	33.31	0.34
				"Good"					
3651	27	54 Psc	0.85	K0 V		44	13.8	33.36	0.32
78366			0.60	G0 V	28.95	10	12.2	33.60	6.25
114710		β Com	0.57	G0 V	28.06	12	16.6	33.72	4.34
115404	505		0.93	K1 V	28.02	18	12.4	33.28	1.93
149661		V 2133 Oph	0.82	K0 V	28.16	21	17.4	33.38	1.42
156026	664	V 2215 Oph	1.16	K5 V	27.75	21	21.0	33.13	1.42
201092	820 B	61 Cyg B	1.37	K7 V	27.15	38	11.7	32.93	0.43
219834A		94 Aqr A	0.80	G5 IV–V	27.59	42	21.0	33.40	0.35
				"Fair"					
1835	17.3	BE Cet	0.66	G2 V	28.99	8	9.1	33.54	9.77
18256		ρ^3Ari	0.43	F5 V	28.69	3	6.8	34.05	69.44
20630	137	κ Cet	0.68	G5 V	28.89	9	5.6	33.50	7.72
26913		V 891 Tau	0.70	G8 V	29.20	7	7.8	33.49	12.76
82885		SV LMi	0.77	G8 IV–V	28.38	18	7.9	33.42	1.93
100180		88 Leo	0.57	F7 V	27.77	14	3.6	33.72	3.19
154417	654.1	V 2213 Oph	0.57	F8 V	28.82	8	7.4	33.72	9.77
157856			0.46	F5 V	29.21	4	15.9	33.93	39.06
161239		84 Her	0.65	G6 V		29	5.7	33.58	0.74
165341A	702	70 Oph A	0.86	K0 V	28.31	20	5.1	33.35	1.56
187691		o Aql	0.55	F8 V	28.05	10	5.4	33.75	6.25
190007	775		1.17	K4 V	27.81	29	13.7	33.10	0.74
190406	779	15 Sge	0.61	G1 V	27.80	14	2.6	33.64	3.19
				"Poor"					
3229		14 Cet	0.44	F2 V (F IV)	29.53	2	4.9	33.00	156.25
37394			0.84	K1 V	28.55	11	3.6	33.37	5.17
76572		61 Cnc	0.43	F3 V		4	7.1	34.05	39.06
82443	354.1		0.77	K0 V	29.30	6	2.8	33.42	17.36
111456			0.46	F6 V	29.41	1	7.0	33.93	625.00
120136	527 AB	τ Boo	0.48	F7 V	28.95	4	11.6	33.87	39.06
155885		36 Oph B	0.86	K1 V	28.28	21	5.7	33.35	1.42
176051			0.59	G0 V	28.06	16	10.0	33.69	2.44
182101			0.44	F6 V	28.97	2	5.1	34.00	156.25
188512	771 AB	β Aql	0.86	G8 IV	28.56	52	4.1	33.35	0.23
194012			0.51	F5 V	28.36	7	16.7	33.82	12.76
206860		HN Peg	0.59	G0 V	29.25	5	6.2	33.69	25.00
224930	914 AB	85 Peg	0.67	G3 V	27.51	33	10.2	33.52	0.57

Table 2. Stars with chaotic chromospheric activity

HD	Gliese	Star	$B–V$	Spectrum	$\log L_X$ [erg/s]	P_{rot}, days	$\log L_{bol}$, [erg/s]	$D/D_\odot$
3443	25		0.72	G5 V		30	33.77	0.69
3795	27.2		0.70	G3 V		33	33.49	0.57
6920		44 And	0.60	F8 V	29.48	14	33.66	3.19
9562			0.64	G2 V		29	33.59	0.74
10700		τ Cet	0.72	G8 V	27.00	34	33.47	0.54
10780			0.81	K0 V	28.34	23	33.40	1.18
12235	83.2	112 Psc	0.62	Gl V	28.46	14	33.63	3.19
13421		64 Cet	0.56	F8 V		17	33.73	2.16
16673			0.52	F8 V	28.54	7	33.79	12.76
17925	117		0.87	K0 V	28.08	7	33.34	12.76
22049		ε Eri	0.88	K2 V	28.32	12	33.33	4.34
22072			0.89	G7 V		55	33.32	0.21
23249		δ Eri	0.92	K0 V	26.95	71	33.30	0.12
25998		50 Per	0.46	F7 V	29.54	2	33.93	156.25
26923		V 774 Tau	0.59	G0 V	29.21	7	33.69	12.76
29645			0.57	G3 V		17	33.72	2.16
30495		58 Eri	0.63	Gl V	28.83	11	33.61	5.17
33608			0.46	F6 V	29.15	3	33.93	69.44
35296		111 Tau	0.53	F8 V	29.44	4	33.78	39.06
39587		χ^1 Ori	0.59	G0 V	29.08	5	33.69	25.00
43587	231.1A		0.61	G0 V		20	33.64	1.56
45067			0.56	F8 V		8	33.73	9.77
61421	280AB	α CMi	0.42	F5 IV–V	28.28	3	34.08	69.44
72905		π^1 UMa	0.62	F7 V	29.11	5	33.63	25.00
75332			0.49	F7 V	29.56	4	33.87	39.06
76151			0.67	G3 V	28.33	15	33.52	2.78
88355		34 Leo	0.46	F6 V		5	33.93	25.00
88737			0.56	F5 V		8	33.73	9.77
89744			0.54	F6 V		9	33.77	7.72
95735	411	Lld 21185	1.51	M2.1 Ve	26.78	53	32.50	0.22
97344			0.61	G0 V		8	33.64	9.77
100563		89 Leo	0.46	F5 V	29.13	4	33.93	39.06
101501	434	61 UMa	0.72	G8 V	28.21	17	33.47	2.16
106516			0.46	F6 V	27.93	7	33.93	12.76
107213		9 Com	0.50	F8 V		9	33.85	7.72
114378	501AB	α Com	0.45	F5 V+F5 V	29.34	3	33.95	69.44
115043	503.2		0.60	Gl V	28.95	6	33.66	17.36
115383		59 Vir	0.58	F8 V	29.51	3	33.70	69.44
115617	506	61 Vir	0.71	G6 V		29	33.48	0.74
124570		14 Boo	0.54	F6 V		26	33.77	0.92
124850		ι Vir	0.52	F7 IV	29.63	7	33.79	12.76
126053	547		0.63	G3 V		22	33.61	1.29
129333	559.1	EK Dra	0.61	G0 V	30.01	3	33.64	69.44
131156A	566 A	ζ Boo A	0.76	G8 V	28.90	6	33.42	17.36

Table 2. (Contd.)

HD	Gliese	Star	*B–V*	Spectrum	$\log L_X$ [erg/s]	P_{rot}, days	$\log L_{bol}$, [erg/s]	$D/D_\odot$
131156B	566 B	ζ Boo B	1.17	K4 V	28.34	11	33.10	5.17
136202		5 Ser	0.54	F8 IV–V		14	33.77	3.19
137107AB	584AB	η Cr B	0.58	G2 V+G2 V	28.41	14	33.70	3.19
141004	598	λ Ser	0.60	G0 V	27.66	26	33.66	0.92
142373	602	χ Her	0.56	F9 V		15	33.73	2.78
143761	606.2	ρ Cr B	0.60	G2 V		17	33.66	2.16
155885		36 Oph A	0.86	K0 V	28.28	21	33.35	1.42
158614	678		0.72	G8 IV–V		34	33.47	0.54
159332			0.48	F4 V		7	33.89	12.76
165341		70 Oph B	1.16	K6 V	28.38	34	33.13	0.54
176095			0.46	F5 IV	29.00	4	33.93	39.06
178428			0.70	G4 V	28.23	22	33.49	1.29
182572	759	31 Aql	0.77	G8 IV	27.59	41	33.42	0.37
185144	764	σ Dra	0.80	K0 V	27.61	27	33.40	0.86
187013		17 Cyg	0.47	F5 V	28.68	6	33.90	17.36
190360	777		0.73	G6 IV		38	33.46	0.43
207978		15 Peg	0.42	F0 V		3	34.08	69.44
212754	9782	34 Peg	0.52	F5 V		12	33.79	4.34
216385	9801	σ Peg	0.48	F7 IV		7	33.89	12.76
217014	882	51 Peg	0.67	G5 V		37	33.52	0.46

traced here. Recall that the stars in Fig. 2 are near the main sequence (Fig. 1), for which the relationship between X-ray luminosity and rotational speed is undoubted. The presence of some scatter among the points, especially the deviation from the lower envelope toward larger luminosities, is due to the fact that some stars, even those near the Sun, are younger than the Sun. The influence of age is manifest first and foremost in the rotation speed: younger stars have shorter rotational periods. However, the shift of the points in Fig. 2a due to the influence of age is not strictly along the *X* axis; this becomes clear, for example, if we join the points from [10] for G stars with different ages. This means that, even if we consider a single rotational period, younger objects are higher in this diagram than stars that are older or the same age as the Sun.

The uniform data considered here clearly show a result noted earlier in [12]: the X-ray luminosities of stars with irregular, chaotic activity are higher than those of objects with well established activity cycles. One exception is the rapidly rotating star V2292 Oph (HD 152391; P_{rot} = 11 days), whose unusual chromospheric and photospheric variations were recently noted in [21].

Analysis of the X-ray data for the groups of stars with different degrees of cyclicity shows that stars within a single group tend to cluster in a $\log L_X - P_{rot}$ diagram. This is especially true of the eight stars in the Excellent group and two stars in the Good group with clearly defined cycles. These stars, with spectral types G7–K7 (except for HD 81809, whose spectral type is close to that of the Sun), are clustered near $\log L_X \approx 27.5$ and $P_{rot} \approx 40$ days. They also occupy a very small region in the $\log L_X/L_{bol} - P_{rot}$ diagram with $\log L_X/L_{bol} \approx -5.7$.

Stars with other activity parameters, which rotate more rapidly, and which have poorly defined cycles demonstrate less strong clustering; their X-ray luminosities are factors of three to one hundred higher than those of stars with better defined cyclicity.

Similar behavior can be seen in Fig. 2b, which plots the ratio of the X-ray to the bolometric luminosity as a function of the *B–V* color index. We can see that stars with well defined cycles have roughly the same ratio $\log L_X/L_{bol} \approx -5.7$. At the same time, for most stars with irregular chromospheric activity, this ratio covers the wide range $\log L_X/L_{bol} = -4.2$ to -6.0. These values are far from the limiting value for X-ray saturation for active red dwarfs and components of RS CVn binary systems, $\log L_X/L_{bol} \approx -3$.

The mean value of $\log L_X/L_{bol}$ for the Sun is roughly a factor of 30 lower than for most of the HK-project

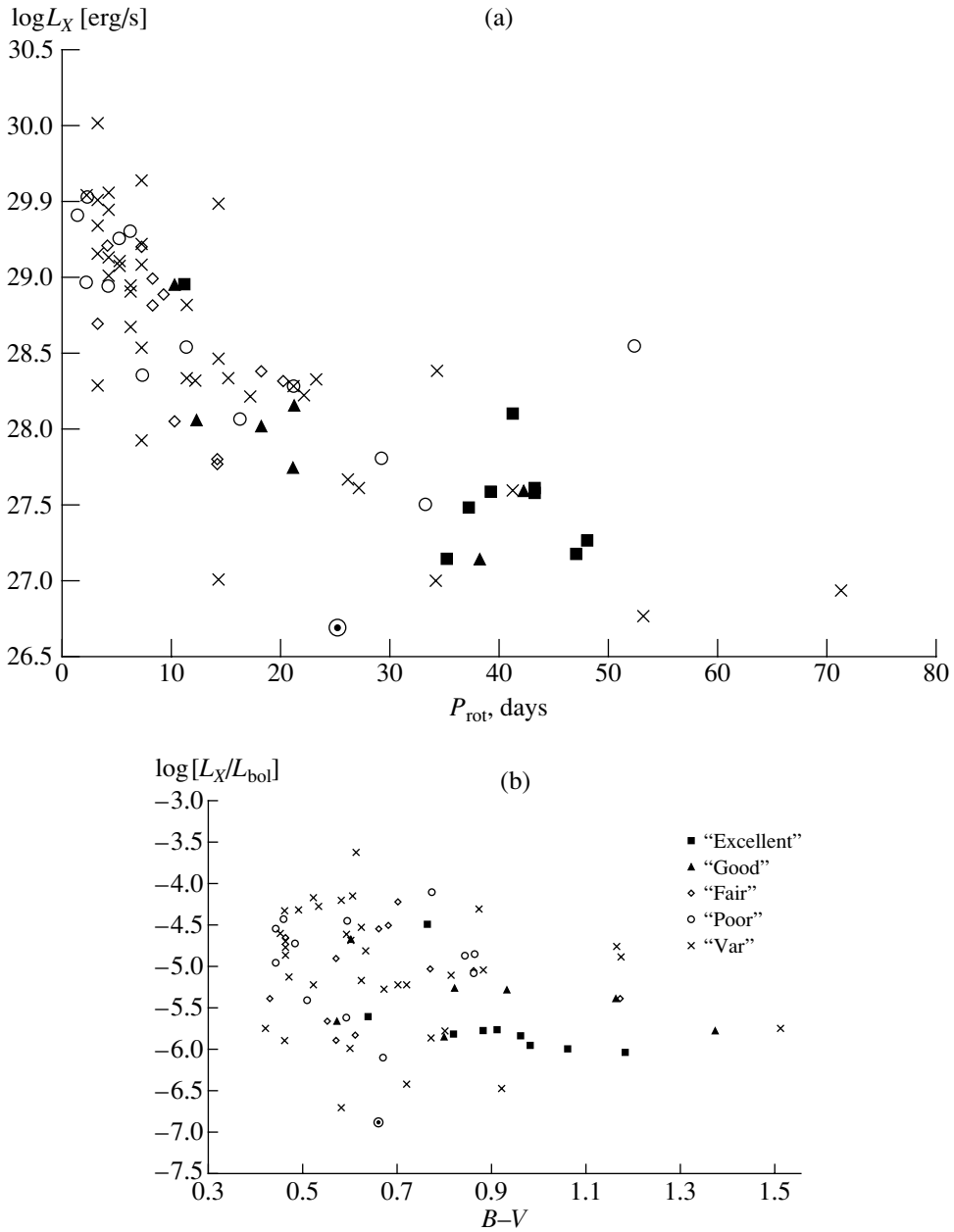

Fig. 2. (a) X-ray luminosity as a function of the period of axial rotation for HK-project stars (from ROSAT data). (b) Ratio of the X-ray to the bolometric luminosity for HK-project stars as a function of *B–V*. Notation is the same as in Fig. 1.

stars considered here. This is primarily due to the different ages for these stars and the Sun. In addition, this could reflect individual properties of the Sun's activity compared to the analogous processes developing on other stars. Note that the Sun is the most rapid rotator among the stars with well defined cycles (with the exception of V2292 Oph, discussed above).

It is interesting to ask what determines the duration of the cycle of an individual star. The available observations made over 35 years contain only limited information about this question. Figure 3 compares the cycle durations and rotational periods for the groups of stars with differing degrees of cyclicity. In a number of cases, a statistical analysis leads to poorly defined, long-term variations being represented as a superposition (as a rule, of two) periodic components; clearly, such cycle durations should be treated with caution. Therefore, we have presented two pairs of values in Fig. 3 (the duration of the cycle and its harmonic) only for the three stars HD 78366, HD 114710 (β Com), and HD 149661 (V2133 Oph), whose main cycles are characterized as Good.

Stars with well defined cycles rotate slowly, and the durations of their cycles are from 7 to 17 years. In con-

trast to the earlier opinion that well defined cycles usually have durations of 10–11 years, Fig. 3 shows that the scatter in the durations is appreciable. As noted above, V2292 Oph has an exception cycle, as can also be seen in this figure.

The durations of the cycles of rapidly rotating stars with poorly defined periods for their long-term variations cover a wide range from 2.8 to roughly 20 years, but nearly half of them have "cycles" shorter than 8 years. This provides evidence that decreasing the rotational speed not only leads to the formation of a stable cycle, but that the duration of this cycle will exceed the values typical of rapidly rotating stars.

The information discussed above can be used to address the question of the place of solar activity among similar processes occurring on late-type stars. Here, we should bear in mind several important factors. The Sun has the earliest spectral type in the group of stars with well defined cycles. The chromospheric activity of the Sun as a star is similar to the mean activity level for stars of this group, as is indicated by a comparison of the flux in the Ca II H and K lines $\log R'_{HK}$; this can be seen in Fig. 8a of [4]. On the other hand, the X-ray luminosity of the Sun is appreciably smaller than those of other stars with cycles, as is clearly reflected by the ratio of its X-ray to its bolometric luminosity. In addition, the Sun rotates appreciably more rapidly than the remaining stars with well defined cycles. It is possible that the Sun is located near the boundary where chaotic, irregular activity is transformed into more regular, cyclic behavior. This could be an important argument in searching for the origin of the Maunder minimum.

Thus, we can see that stars with well defined activity cycles and those whose activity is fairly irregular form two clusters in our diagrams. Well defined cycles correspond to longer durations of the activity cycles, longer rotational periods, and lower X-ray fluxes; i.e., lower magnetic-field strengths. This last correlation can also be seen in the figure presented in [23], although it is not specially discussed in that work.

This last conclusion may, at first glance, seem paradoxical from the point of view of dynamo theory, which explains both the magnetic-field strength and the cycle duration in the framework of a single mechanism for the generation of the magnetic field. Below, we will demonstrate that this correlation can fit into the stellar-dynamo mechanism.

4. PARAMETERS OF STELLAR CYCLES AND THE PARKER DYNAMO

The explanation of the origin of stellar cycles in the framework of dynamo theory proposed by Parker in 1955 can be reduced to the following. The poloidal component of the large-scale magnetic field of a star, which can be expressed in terms of the azimuthal component of the vector potential of the magnetic field A, is wound up by differential rotation, leading to the formation of an azimuthal component of the magnetic field B. In turn, the helicity of the convective flows α acts on the azimuthal field component, giving rise to a poloidal magnetic field and closing the cycle of self-excitation. This process can be described quantitatively using the Parker dynamo equations, which, in the simplest case, have the form

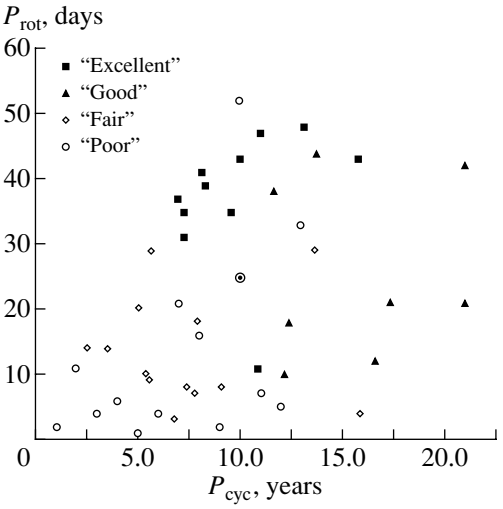

Fig. 3. Periods of axial rotation and cycle durations for HK-project stars with more or less well defined activity cycles. Notation is the same as in Fig. 1.

$$\frac{\partial A}{\partial t} = \alpha B + \frac{\partial^2 A}{\partial \theta^2}, \quad (1)$$

$$\frac{\partial B}{\partial t} = -DG\cos\theta\frac{\partial A}{\partial \theta} + \frac{\partial^2 B}{\partial \theta^2}, \quad (2)$$

where θ is latitude, and $G = r^{-1}\frac{\partial \Omega}{\partial r}$ is the radial gradient of the angular velocity in units of its maximum value. The quantity α is also measured in units of its maximum value. The dimensionless number D, called the dynamo number, characterizes the intensity of sources of magnetic-field generation. This number is expressed in terms of parameters characterizing the hydrodynamics of the convective envelope; in the simplest case, we can use the approximate expression

$$\frac{D}{D_\odot} = \left(\frac{R}{R_\odot}\right)^3\left(\frac{h_\odot}{h}\right)\left(\frac{v_{conv}^\odot}{v_{conv}}\right)^2\left(\frac{\Omega}{\Omega_\odot}\right)^2, \quad (3)$$

where R is the radius of the zone of magnetic-field generation, h is the scale height, Ω is the angular velocity of the stellar axial rotation, and v_{conv} is the convective velocity. Here, when calculating G, we exchanged $\frac{\partial \Omega}{\partial r}$ with $\frac{\Omega}{R}$ and estimated α using the so-called Krause formula (see, for example, [24]).

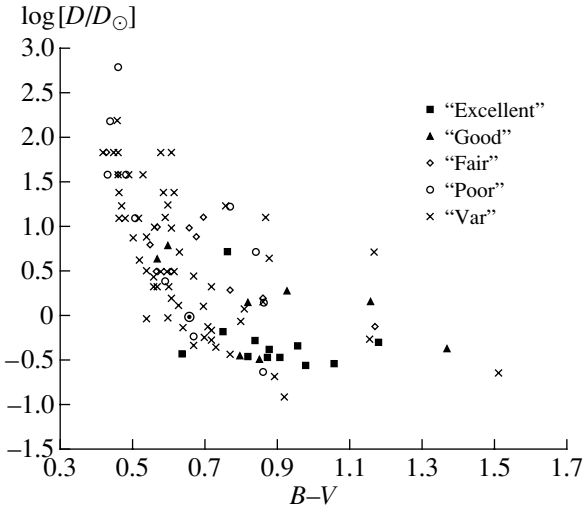

Fig. 4. Variation of the dynamo number (relative to the solar value) as a function of *B–V* for HK-project stars. Notation is the same as in Fig. 1.

When deriving the Parker dynamo equations, it is assumed that the convective zone, indeed, forms a sort of envelope. If the convective zone is very narrow, then the term corresponding to radial diffusion of the magnetic field must be kept in equations (1) and (2). In the case of very narrow, vanishingly thin convective zones, this term becomes dominant and disrupts the dynamo action, so that the magnetic field decays. If the convective zone occupies the entire star, the generation of magnetic field is possible, but it has an appreciably different character than in the case of a convective envelope. In particular, the generation sources must usually have appreciably higher intensities than in the case of a convective zone with moderate thickness. The question of the character and origin of the change in the type of dynamo in the presence of a degenerate point radiative core remains poorly studied theoretically. We emphasize that our stars have convective zones of moderate thickness.

Applying (3) to specific late-type stars, we should note that the first three multiplicative factors on the right-hand side compensate each other to a large extent. For example, if we use classical models for the convective zones, the products of these three factors for stars from F5 to M3 differ by only a factor of two. Thus, if we do not consider the limiting cases of stars with very thin convective zones and the latest M stars with complete convection, the dynamo number can be taken to be proportional to the square of the angular velocity of rotation of the star.

Traditionally, the behavior of periods of stellar activity has been analyzed using the Rossby number. Since both the dynamo numbers and the Rossby numbers of our stars are primarily determined by the angular velocity of rotation (relative to that of the Sun), the two parametrizations are similar in practice. However, conceptually, the dynamo number characterizes the sources of field generation in the dynamo mechanism and appears in the Parker equations explicitly, so that we will use this quantity in our analysis.

We estimated the dynamo numbers using (3), and present the dependences of parameters of the stellar cycles on the dynamo number (in units of the solar value) in Fig. 4. We can see that well defined cycles correspond to comparatively low dynamo numbers *D* and modest magnetic-field strengths. When the dynamo number increases, the magnetic-field strength also increases, as seems natural (increased intensity of the generator leads to a growth in the generated field). However, the degree of organization of the cycle decreases, so that stars with very well defined cycles give way to stars with higher, less constant levels of activity and weakly defined cycles.

To explain this correlation, we turn to the properties of Eqs. (1) and (2). They have solutions in the form of travelling waves, called dynamo waves, whose propagation through the convective zone reflects the phenomenon of stellar activity. The dispersion relation linking the complex eigennumber of these equations—i.e., the growth rate and cycle frequency—and the dynamo wavelength separates out the dynamo wave with the maximum growth rate. It is natural to suppose that it is this wave that determines the formation of waves of stellar activity, and that precisely its parameters are inherited at the stage of evolution of the magnetic field when non-linear effects cease the exponential growth of the dynamo-wave amplitude. It is not difficult to convince oneself that the wavelength and period of this distinguished dynamo wave decrease with growth in *D*. Precisely this tendency can be seen in Fig. 4 (see [23]).

The decrease in the wavelength of the dynamo wave with growth in the dynamo number for a fixed convective-zone radius means that more and more half-waves of magnetic activity begin to be present between the poles and equator. It is natural to expect that, in the nonlinear regime, each of these half-waves lives a comparatively independent life; in the language of the theory of dynamical systems, Eqs. (1) and (2) describing the magnetic field as a distributed system with an infinite number of degrees of freedom can be approximately reduced to a certain dynamical system. The number of variables (degrees of freedom) in this system is determined by the number of half-waves present in the direction of propagation of the dynamo wave. This effective number of degrees of freedom increases with the dynamo number. Similar phenomena are typical of a wide circle of problems in non-linear dynamics. This was first noted by Hopf in his formulation of a scenario for the transition from laminar to turbulent flow. The growth in the number of degrees of freedom occurs in a discrete fashion, making it tempting to interpret the existence of discrete groups with different characters of stellar activity—though, of course, distinguished somewhat arbitrarily—as a reflection of real discreteness

associated with an increase in the number of half-waves.

An increase in the number of degrees of freedom of a dynamical system usually leads to a qualitative change in its behavior. In the case of a small number of degrees of freedom (modest dynamo number), the nonlinear evolution of the dynamical system has the character of self-excited oscillations (the system has extreme cyclicity). As the number of degrees of freedom grows, a regime of chaotic behavior in the form of strange attractors usually arises. We suggest that the numerous cases of aperiodic variations of stellar activity are associated with large dynamo numbers, with their corresponding chaotic regimes. The transition from extreme cyclicity to strange attractors and chaotic behavior represents a modern scenario for the development of turbulent flow from laminar flow; at its base lies a bifurcation that increases the dimension of the corresponding dynamical system. We propose that the appearance of discrete classes of stellar activity has analogous origins. In other words, we propose to interpret the fact that stars with well defined cycles display comparatively low-intensity magnetic-field generation, while stars with more intensive field generation do not have well defined cycles, as observational confirmation of a "cyclic behavior–chaotic behavior" bifurcation in the stellar dynamo, associated with an increase in the effective dimension of the system as the dynamo number is increased.

A possible alternative interpretation is that, in the case of large dynamo numbers, the magnetic field in the depths of the convective zone preserves cyclic behavior, but, for some reason, the link between the magnetic field and surface activity tracers is disrupted. We believe that this point of view encounters more difficulties, since the overall level of activity is increased when the dynamo number is increased, and only its cyclic character disappears.

In connection with our proposed interpretation, it is valuable to consider the position of the Sun in these diagrams separately. Of course, the assignment of the Sun to the ranks of stars with very well defined activity periods is due to the anomalously small distance of the Sun from the Earth, and the associated exceptionally detailed study of solar activity that has been possible. It is well known that the intensities of different solar-activity cycles can differ substantially; observing two such cycles on a distant star, it is doubtful that we would classify its cyclic activity as ideal. On the other hand, to a first approximation, the Hale polarity law is fulfilled on the Sun; i.e., data on sunspots specify in each hemisphere only a single half-wave of solar activity. At the same time, data for other tracers of solar activity specify additional waves, such as the polar wave, visible in analyses of polar facculae. Finally, the time dependence of solar activity reveals a well defined periodic component with an added chaotic component in the form of rare long-term drops in activity such as the Maunder minimum. All these data are consistent with the idea that the position of the Sun in our diagrams is near the edge of the region of well defined periodic behavior.

5. CONCLUSION

Thus, among late-type stars, the soft X-ray luminosities and ratios $L_X/L_{\rm bol}$ are substantially higher for stars with irregular activity than for those with well defined cycles. This is consistent with the result obtained earlier in [12]. A detailed analysis for stars with reliably distinguished activity cycles indicates that, for comparatively slowly rotating stars of spectral types later than G0, the power of the corona decreases with the development of well defined cyclicity. This conclusion does not pertain to flare stars, for which a new effective mechanism for coronal heating probably begins to operate, associated with the occurrence of numerous weak flares (microflaring). The influence of age on the X-ray flux can be traced in our sample, however it is not strong for these solar-neighborhood stars, and cannot be responsible for the observed variations of L_X and $L_X/L_{\rm bol}$.

Our conclusions are relevant for stars with spectral types from F5 to M3, in which the thickness of the surface convective zones is neither very small, nor very large compared to the stellar radius. This is consistent with the idea that realization of the dynamo mechanism requires the existence of an envelope in which the magnetic-field amplification can develop. It goes without saying that efficient operation of the dynamo mechanism requires differential rotation and turbulent convection.

Our analysis demonstrates that the level of X-ray emission is primarily determined by the parameter that also determines the efficiency of the dynamo mechanism—the dynamo number. In the stars considered here, the influence of factors connected with the structure of their convective zones compensate each other to a large extent, so that, in accordance with (3), the dynamo number is determined by the square of the speed of axial rotation. The transition from small to large dynamo numbers gives rise to a change in the character of the dynamo process, increasing its chaotic component.

We note especially that the general dependence of the activity on Rossby number discovered earlier is also preserved, due to the strong influence of the speed of axial rotation on both characteristic numbers—the Rossby and dynamo numbers. The behavior we have found has a more direct relationship to the theory of the $(\alpha - \Omega)$ dynamo. This behavior can be disrupted in stars with anomalously weak differential rotation, such as members of close binary systems, whose differential rotation is damped by tidal forces.

In conclusion, we note that these results prompt us to re-evaluate the position of solar activity among analogous processes occurring on other stars. If we do not consider the exceptional star V2292 Oph, the Sun is

located at the boundary of the region in Fig. 2a occupied by stars with cyclic activity, with the Sun rotating more rapidly than the other stars with well defined cycles. Note that the Sun's level of chromospheric activity is fairly high: the ratio of the luminosity in chromospheric emission to the bolometric luminosity is roughly the same as that of other stars with well defined cycles (see, for example, [4]). On the other hand, the solar corona is appreciably weaker than the typical coronas of active late-type stars: the solar ratio L_X/L_{bol} is about 10^{-7}, while this ratio for other active stars on the lower part of the main sequence is several orders of magnitude higher.

ACKNOWLEDGMENTS

The authors thank M.A. Livshits for fruitful discussions. This work was supported by the Russian Foundation for Basic Research (project code 01-02-17693), a grant for the Support of Leading Scientific Schools of the Russian Federation (00-15-96553; M. M. K.), the State Science and Technology Program in Astronomy (project 1.4.3.4; E. A. B. and M. M. K.), and a NATO Collaborative Linkage Grant (PST.CLG.976557; M. M. K.).

REFERENCES

1. O. C. Wilson, Astrophys. J. **138**, 932 (1968).
2. O. C. Wilson, Astrophys. J. **226**, 379 (1978).
3. S. L. Baliunas, R. A. Donahue, and W. H. Soon, Astrophys. J. **438**, 269 (1995).
4. R. R. Radick, G. W. Lockwood, B. A. Skiff, and S. L. Baliunas, Astrophys. J., Suppl. Ser. **118**, 239 (1998).
5. I. Yu. Alekseev and R. E. Gershberg, Astron. Zh. **73**, 579 (1996) [Astron. Rep. **40**, 528 (1996)]; Astron. Zh. **73**, 589 (1996) [Astron. Rep. **40**, 538 (1996)].
6. I. Yu. Alekseev, Astron. Zh. **76**, 784 (2000) [Astron. Rep. **44**, 696 (2000)].
7. M. Hünsch, J. H. M. M. Schmitt, and W. Voges, Astron. Astrophys., Suppl. Ser. **132**, 155 (1998).
8. M. Hünsch, J. H. M. M. Schmitt, M. F. Sterzik, and W. Voges, Astron. Astrophys., Suppl. Ser. **135**, 319 (1999).
9. O. Vilhu and F. M. Walter, Astrophys. J. **321**, 958 (1987).
10. M. Güdel, E. F. Guinan, and S. L. Skinner, Astrophys. J. **483**, 947 (1997).
11. M. M. Katsova, O. G. Badalyan, and M. A. Livshits, Astron. Zh. **64**, 1243 (1987) [Sov. Astron. **31**, 652 (1987)].
12. A. Hempelmann, J. H. M. M. Schmitt, and K. Stepien, Astron. Astrophys. **305**, 284 (1996).
13. V. Straizis and G. Kuriliene, Astrophys. Space Sci. **80**, 353 (1981).
14. R. E. Gershberg, M. M. Katsova, M. N. Lovkaya, *et al.*, Astron. Astrophys., Suppl. Ser. **139**, 555 (1999).
15. M. Schüssler, P. Caligari, A. Ferriz-Mas, *et al.*, Astron. Astrophys. **314**, 503 (1996).
16. A. H. Vaughan and R. W. Preston, Publ. Astron. Soc. Pac. **92**, 385 (1980).
17. R. W. Noyes, L. W. Hartmann, S. L. Baliunas, *et al.*, Astrophys. J. **279**, 763 (1984).
18. S. L. Baliunas, D. D. Sokoloff, and W. Soon, Astrophys. J. Lett. **457**, L99 (1996).
19. L. W. Acton, in *The Cool Stars, Stellar Systems, and the Sun*, Ed. by R. Pallavicini and A. K. Dupree, Astron. Soc. Pac. Conf. Ser. **109**, 45 (1996).
20. R. Pallavicini, Astron. Astrophys. Rev. **1**, 177 (1989).
21. I. Yu. Alekseev, R. E. Gershberg, M. M. Katsova, and M. A. Livshits, Astron. Zh. **78** (6), 558 (2001) [Astron. Rep. **45**, 482 (2001)].
22. M. Güdel, J. L. Linsky, A. Brown, and F. Nagase, Astrophys. J. **511**, 405 (1999).
23. S. Baliunas, E. Nesme-Ribes, D. Sokoloff, and W. Soon, Astrophys. J. **460**, 848 (1996).
24. G. Belvedere, A. Lanza, and D. Sokoloff, Sol. Phys. **183**, 435 (1998).

Translated by D. Gabuzda

Astronomy Reports, Vol. 45, No. 9, 2001, pp. 729–737. Translated from Astronomicheskiĭ Zhurnal, Vol. 78, No. 9, 2001, pp. 839–848.

The Plane of Polarization of the Solar Coronal Emission on August 11, 1999

Y.-D. Park[1], I. S. Kim[2], O. I. Bugaenko[2], M. I. Divlekeev[2], V. V. Popov[2], and V. N. Dermenjiev[3]

[1]*Korea Astronomy Observatory, Whaam-dong 61-1, Yuseong-gu, Taejeon 305-348, Korea*
[2]*Sternberg Astronomical Institute, Universitetskiĭ pr. 13, Moscow, 119899 Russia*
[3]*Institute of Astronomy, Bulgarian Academy of Sciences, blvd. Tsarigradsko Shosse 72, Sofia, Bulgaria*

Received February 20, 2001

Abstract—A two-dimensional polarization image of the inner regions of the solar corona ($R \le 1.5R_\odot$) during the total solar eclipse of August 11, 1999 is presented. This image clearly exhibits both small- and large-scale structure in the distribution of deviations of the plane of polarization from its theoretical direction for coronal emission in the near infrared (570–800 nm). An accuracy for the deviation angles of ≤1° was achieved by reducing the instrumental scattered light in the telescope, installing a continuously rotating polaroid near the image plane of the entrance pupil (i.e., the Lyot stop plane), and developing a special algorithm for constructing the polarization images based on the IDL software, in which the properties of the light are described in terms of the Stokes parameters. This algorithm was used to process 24 digitized polarization images of the corona, corresponding to one complete rotation of the polaroid. Analysis of the polarization image for angles of 0°–5° indicates the existence of significant deviations in the inner corona. The polar and equatorial coronal regions are characterized by diffuse and almost uniform structure of the deviation angles, 0.5° ± 0.5°, corresponding to Thomson scattering of the photospheric radiation by free electrons. Four large-scale structures over the NE, SE, NW, and SW limbs covering about 60° in position angle have deviations of 1°–3°. Numerous small-scale structures with dimensions up to 30″ and deviation angles of 3°–5° tracing strongly curved coronal streamers were detected in active coronal regions, especially over the NE limb. Interpretation of these deviations in terms of flows of moving electrons implies tangential velocities of up to 2.5×10^4 km/s, i.e., electron energies of up to 2×10^3 eV. © *2001 MAIK "Nauka/Interperiodica".*

1. INTRODUCTION

Both space and ground-based observations in the continuum and cool and hot emission lines testify to the presence of appreciable structure in the upper atmosphere of the Sun. Knots, loops, arches, streamers, and ejections with transverse spatial sizes in the plane of the sky less than 1″ (≈725 km at the solar surface) are typical of both cool prominences and the hot corona, whose emission is associated with three components. Continuum observations show the so-called white-light corona, which is composed of the K component, due to Thomson scattering of photospheric radiation by free coronal electrons, and the F component, associated with scattering by interplanetary dust. On the other hand, observations in hot or cool emission lines reveal the structure of the E (emission-line) corona and of prominences, respectively. Fine structure becomes more prominent in polarized light, since the emission of the upper atmosphere (in particular, of the corona and prominences) becomes polarized due to the disruption of the spatial symmetry that occurs in various physical processes giving rise to the observed emission [1], such as excitation by radiation or a directed particle beam, the influence of magnetic fields (the Zeeman and Hanle effects) and macroscopic electric fields (the Stark effect), and so on.

Polarimetric data provide information about the emission mechanisms and physical conditions in the upper layers of the solar atmosphere. We shall briefly consider problems associated with polarization measurements of the white-light corona and present the results of our own measurements of the coronal plane of polarization on August 11, 1999, during the total solar eclipse in Shabla (Bulgaria).

1.1. Problems Associated with Polarization Measurements of the Weak Upper Solar Atmosphere near Bright Inner Layers

Accurate polarization measurements in the upper solar atmosphere remain quite difficult. The main sources of errors are [2]

(1) polarization of the sky,

(2) instrumental polarization,

(3) nonuniform characteristics of the polaroids over their surface.

The *brightness of the day-time sky* at high-mountain coronal observatories, on average $(1 - 5) \times 10^{-5}B_\odot$ (where $B_\odot$ is the brightness at the center of the solar disk), is comparable to that of the white-light corona ($5 \times 10^{-5}B_\odot$) at

a distance of $\approx 1.2R_\odot$. (Distances are measured from the center of the solar disk, and $R_\odot$ is the apparent radius of the solar disk.) Therefore, noneclipse coronographic polarimetric observations suffer from appreciable errors and, as a rule, are used primarily for the qualitative identification of the electron component. On the other hand, the sky brightness decreases to $(10^{-9}–10^{-8})B_\odot$ during total solar eclipses. As a result, the conditions imitate those for space observations, without instrumental errors due to the contribution of the sky, at least for polarimetric studies at $R < 1.5R_\odot$.

The *instrumental polarization* for coronal measurements during a total solar eclipse is due primarily to the emission of the innermost regions in the corona ($R < 1.15R_\odot$), which is diffracted by the entrance aperture, and to the microroughness of the telescope's primary optical system. This polarization can be appreciable, since the variations in brightness at $(1.15–1.5)R_\odot$ can reach two to three orders of magnitude. In the case of a refractive primary optical system, its contribution can be minimized using the Lyot coronographic method [3]. Unfortunately, there are have been no theoretical or experimental studies of this problem.

To our knowledge, the *nonuniform characteristics of the polaroids* over their surfaces has likewise not been studied in detail previously. This factor is especially important when polaroids based on polaroid films are mounted near the image plane of the object being studied; i.e., when the rays from different points in the object pass through different parts of the polaroid. In this case, this nonuniformity in the polaroid characteristics, in particular the transmission, leads to a considerable decrease in the accuracy of the polarization measurements and to blurring of the structure of the polarization images.

1.2. Summary of Polarization Studies of the White-Light Corona

We will now briefly discuss polarization studies of the white-light corona during total solar eclipses, which were initiated in the beginning of the last century but were conducted successfully only in the late 1940s.

Most studies have indicated that the degree of polarization increases with distance, reaches its maximum of $\approx 50\%$ at $1.5R_\odot$, then decreases in accordance with expectations for Thomson scattering of photospheric photons by free coronal electrons, described by the model of van de Hulst. A review of all the steps involved in measuring the degree of polarization was given in [4]. In our opinion, the problem of the existence of regions with anomalous degrees of polarization (60–80%) detected in some studies [5–8] remains unresolved.

The determination of the plane of polarization of solar coronal emission is even more difficult. The theoretical prediction is that the plane of polarization (i.e., plane of oscillations of the magnetic vector) should coincide with the radial direction.[1] A rotation of the plane of polarization would provide evidence for the presence of a directed high-speed electron flow [9] or nonuniform photospheric emission field [10, 11]. Early photographic [5, 12] and photoelectric [13] measurements revealed deviations of the plane of polarization from the radial direction as large as 20°. Contradictory results for the orientation of the plane of polarization of the white-light coronal emission have been obtained over the past decade, in particular for the corona on July 11, 1991, by two groups working at the same observing site. On the one hand, photoelectric measurements using a scanning electropolarimeter (with a polarization resolution of 1′–3′) indicated deviations as large as 9° [14]. Another study [15] with a rather high polarization resolution (≈10″) using a rotating sectorial polaroid near the image plane and an original photographic method for analysis of the isophotes found that the orientation of the polarization plane was in agreement with the theoretical prediction everywhere in the corona within the measurement accuracy of 1°.

1.3. The Accuracy of Polarization Measurements

Polarimetric studies of the white-light corona are usually based on the analysis of three coronal images corresponding to three different orientations of the polaroid, to derive three characteristics of the linearly-polarized light: the intensities of the polarized and unpolarized components and the orientation of the plane of polarization. The degree of polarization P is described by the expression

$$P = \frac{I_t - I_r}{I_r + I_t},$$

where I_t and I_r are the tangential and radial components of the intensity. To estimate the error in the degree of polarization, we differentiate this expression and assume as a first approximation that $dI_r \approx dI_t \approx dI$. Then, after some manipulation, we obtain

$$\left|\frac{dP}{P}\right| \approx 2\left|\frac{dI}{I}\right|.$$

The accuracies of intensities determined using photographic methods is 3–4%. Consequently, the actual error in the degree of polarization will be >6–8%.

The deviation of the plane of polarization from the radial direction χ is given by the expression

$$2\chi = \arctan\frac{P_t}{P_r},$$

where P_t and P_r are the projections of the polarization onto the tangential and radial directions, respectively,

[1] Note that the theoretical orientation of the plane of polarization is defined by various authors as the orientation of the plane of oscillation of either the magnetic or electric vectors.

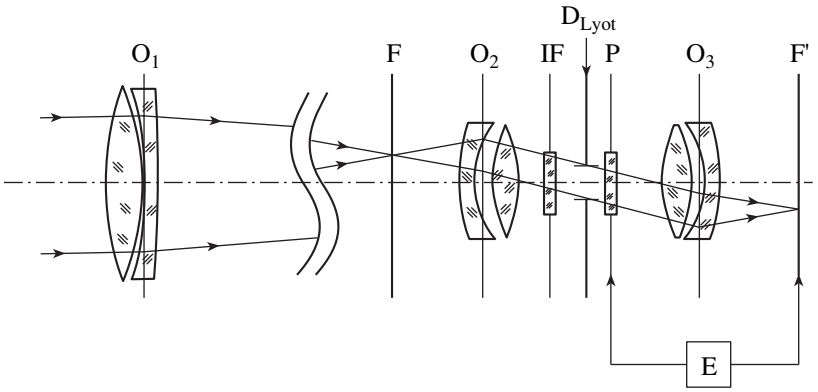

Fig. 1. Optical scheme of the coronographic polarimeter.

in a coordinate system whose origin is at the solar-disk center. When these angles are less than 10° and the radial degree of polarization is P_r = 0.2–0.5, as is typical for the solar corona, we can write

$$d\chi = \frac{1}{2P_r}\left(dP_t - P_t\frac{dP_r}{P_r}\right) \approx \frac{1}{2}\frac{dP_t}{P_r},$$

since the second term in parentheses is one to two orders of magnitude less than the first term. If the radial degree of polarization is 30–50% and the error in the tangential degree of polarization is 10%, typical of the photographic method, we find that the accuracy of the deviation angles in the inner corona is 5°–9°. Use of the equidensity method and the subsequent registration of the equidensities will inevitably increase these errors, due to the considerable radial gradient of the coronal brightness.

The accuracies of photoelectric methods reach 1–2% and 1°–2°, but their spatial resolution is relatively low. As a rule, photoelectric methods based on successive scanning of different coronal regions cannot be used to obtain an "instantaneous" distribution of the polarization parameters in the corona.

The main problem faced by polarization studies is to increase the *actual* accuracy of the measurements to 1–2% for the degree of polarization and 1° for the plane of polarization.

2. OUR CINECORONOGRAPHIC POLARIMETER

To achieve accuracies of 1–2% in the degree of polarization and 1° in the plane of polarization, we developed the following techniques for polarization studies of the inner corona, taking into account the factors noted in the Introduction.

(1) We considerably reduced the instrumental background due to the diffraction of light from the inner corona by the entrance aperture using the Lyot coronographic method. We believe this procedure to be necessary, since the brightness of the innermost coronal regions at 1.05–1.2$R_\odot$ can exceed the coronal brightness at 1.5$R_\odot$ by two to three orders of magnitude.

(2) We filmed continuously through the polaroid, whose rotation was strictly synchronized with the operation of the movie camera. This yielded a large number of pictures corresponding to different polariod orientations, whose subsequent statistical analysis was designed to remove systematic errors.

(3) The polaroid was mounted near the Lyot aperture, making it possible to obtain uniform polarization measurements in which the nonuniform polariod characteristics made the same contribution at each point of the corona.

(4) Recording the coronal emission in the infrared during the total solar eclipses made it possible to neglect the contribution of the sky.

(5) We have developed a special algorithm for constructing the polarization images, based on the IDL software and on the description of the light in terms of the Stokes parameters. The first version of this algorithm was used in our polarization studies of the corona on November 24, 1994 [16].

2.1. Optical Scheme

The development of a portable, expeditionary cinecoronographic polarimeter began at the Sternberg Astronomical Institute in 1991. The instrument was subsequently modernized taking into account the results of observations during the total solar eclipse in 1994 [17]. Figure 1 shows an optical scheme of the version used for our observations on August 11, 1999, in which the contributions of instrumental effects were minimized to an appreciable extent. The light from the expeditionary coelostat was directed to the main objective O_1 (D = 60 m, F_e = 339 mm). The image of the entrance pupil was formed by the lens O_2 (we used a photographic objective with focal distance 50 mm, whose focal plane was coincident with that of the main objective). A rotating polaroid P was placed behind the image plane of the entrance pupil (D_{Lyot}). In this

scheme, collimated beams of rays from each point of the coronal image passed through the same polaroid surface. The diameter of the corresponding light beam at the polaroid was less than 9 mm. The coronal image was reconstructed in the focal plane of a full-size KONVAS professional movie camera using the objective O_3, with a focal length 50 mm. The filming rate was five frames per second, with an exposure time of 0.1 s. The rotation of the polaroid was strictly synchronized with the operation of the movie camera. One complete rotation of the polaroid corresponded to 24 film frames, with the period of rotation being 5 s.

A set of filters IF was mounted in front of the Lyot stop for use in the relative and absolute calibrations and for polarization studies in the continuum and emission lines using neutral and narrow-band interference filters. The optical alignment of such a coronograph is complicated, however the reliability of the measurements is considerably increased.

2.2. Nonuniformity of the Polaroid Characteristics

Polaroid filters based on polaroid film are widely used in polarization studies of the Sun. The most widespread version—a polaroid film placed between two optical glass plates—is manufactured by several firms. We tested polaroids produced by the Zagorsk Mechanical Factory (Russia) and SOLIGOR (Japan). The uniformity of transmission of the polaroids over their surfaces was carefully measured in various spectral ranges using the spectrograph of the solar tower telescope of the Sternberg Astronomical Institute. A collimated light beam was transmitted through a polaroid mounted 10 mm from an spectrograph entrance slit. The light source was an incandescent or cadmium lamp (CdE).

A MOPS-series TCD 1301D device manufactured at the Institute of Spectroscopy of the Russian Academy of Sciences recorded the signal and redirected it to a personal computer for subsequent processing via the corresponding interface. The Japanese CCD used in the TCD 1301D device has 3648 elements, with the each element being 8 μm × 200 μm, and operates at 270–950 nm. Devices of the MOPS series have a dynamic range of 1300, exposures of 10–10000 ms, 1–10000 frames, and 12 bits in the analog-to-digital converter.

A number of diameter cross sections corresponding to the central part of the polaroid with a diameter of 29 mm were recorded for each filter. We measured the spectra at three wavelengths (6438, 5085, and 4799 Å) for each cross section without the polaroid (marked I_0), with the polaroid oriented along the slit (I_0''), and with the polaroid oriented perpendicular to the slit ($I_0^{\perp}$). These last two spectra were normalized to the I_0 for a certain element using the corresponding coefficients. A spectrum obtained without the polaroid (I_0) was subtracted from the normalized spectra. The resulting cross section (with the errors due to nonuniform illumination of the slit, variations in the sensitivity of the elements, and so on minimized) describes the nonuniformity of the polaroid transmission along the corresponding direction.

Figure 2a presents an example of the resulting cross section at 5085 Å for a polaroid manufactured by the Zagorsk Mechanical Factory. The element (pixel) number is plotted along the horizontal axis and the intensity in relative units (where $I_0 \approx 3000$) along the vertical axis. Part of this cross section (with length is 2 mm, centered relative to the element marked by the dotted line) is presented in Fig. 2b. The marked element was used in the normalization of the spectra. The central ≈1000–1300 elements (i.e., 8–10.5 mm) of the spectrum under consideration are characterized by a quasi-periodic transmission structure, with periods of about 7, 14, 50, and 100 elements (corresponding to 0.06, 0.12, 0.4, and 0.8 mm on the polaroid surface). Variations in I_p' between neighboring points can reach 50; i.e., ≈3% of $0.5I_0$. Peripheral zones include some regions 2–2.5 mm in size whose transmission variations reach 10–12% of $0.5I_0$. A comparative analysis of the characteristics of polaroids manufactured by different firms will be presented in more detail in other publications.

Qualitative estimates of the polaroid characteristics in various spectral intervals can be obtained by observing the bright filament of an incandescent lamp through two polaroids with perpendicular orientations. Motion of the eye along the polaroid surface results in scintillation of the lamp filament, whose color is characteristic of the polaroid quality in the corresponding spectral range.

We chose one of the five polaroids manufactured by the Zagorsk Mechanical Factory for mounting in the cinecoronographic polarimeter used during the total solar eclipse of August 11, 1999 for polarization studies of the upper solar atmosphere.

2.3. Infrared Spectrozonal Air Photofilm

A PION-500 spectrozonal, negative, perforated 35-mm aerial photofilm was used as the detector. This film was recently developed by FOMOS for daytime air photography in relative colors from moderate and high altitudes in space. The sensitivity limits of the film in layers beyond the OS-14 filter are 570–690 nm (orange–red, OR) and 670–800 nm (near-infrared, IR); the sensitivity $S_{0.85}$ beyond the OS-14 filter is 1000 GOST at IR and 500 GOST at OR wavelengths. The contrast γ is 2.5 at IR and 2.1 at OR wavelengths, the optical fog density D_0 is 0.14 at IR and 0.25 at OR wavelengths, and the resolution is 120 line/mm. The film is processed using C-41 developer at 30–38°C for six minutes.

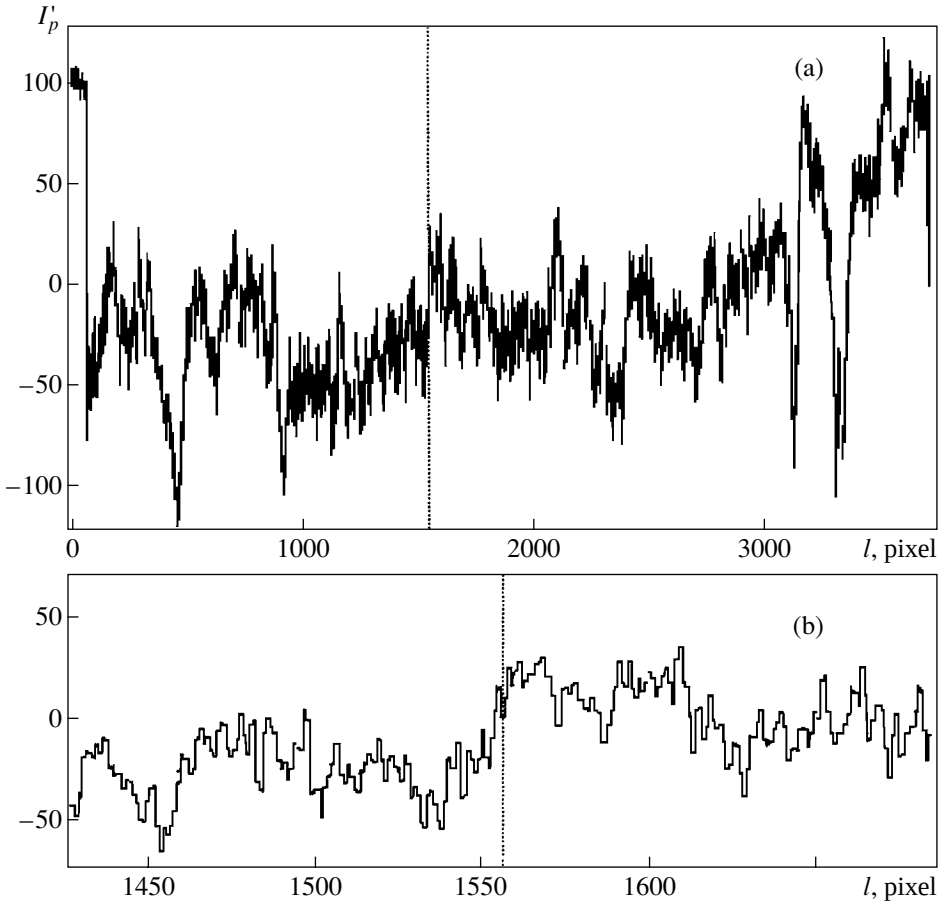

Fig. 2. Nonuniformity of the polaroid transmission along its diameter. The horizontal and vertical axes plot element number and intensity in relative units. The dotted line marks the position of the element whose intensity was used in the normalization of the polaroid transmission.

3. OBSERVATIONS AND PHOTOMETRY

3.1. Observations of the White-Light Corona During Totality

We carried out polarization observations of the upper solar atmosphere using the cinecoronographic polarimeter on August 11, 1999 near Shabla in Bulgaria ($\lambda = 28°35.5'$, $\phi = +43°32'$), which was near the center of the totality pass. The duration of the totality was about 2 min 30 s, and the time of maximum eclipse was $T_{max} \approx 11:12:30$ UT. We filmed continuously, accompanied by rotation of the polaroid, during the totality. An orange filter OS-14 was mounted in front of the primary objective. Our observers (V.V. Popov and E.V. Popova) changed the neutral and interference filters in accordance with our program of studies of the upper solar atmosphere. They recorded the white-light corona in two 10-s filming runs centered about the center of totality using the NS-8 and NS-9 neutral filters (with transmission coefficients of $\approx 1.7 \times 10^{-1}$ and $\approx 2.1 \times 10^{-2}$).

3.2. Absolute and Relative Calibrations

Observations for the absolute calibration were conducted 30 min before the center of totality in the operational regime, using two 10-s filming runs of the crescent Sun with the neutral-filter combinations NS-11 + NS-10 and NS-11 + NS-9 (with transmission coefficients $\approx 3 \times 10^{-9}$ and $\approx 2 \times 10^{-8}$).

We carried out the relative calibration in two ways. Before and after the expedition, we printed a 21-step photometric wedge with an exposure of 0.05 s from an incandescent lamp whose color temperature corresponded to the solar disk (5500 K). In addition, under the expedition conditions, we used a special setup to photograph a nine-step quartz attenuator illuminated by sky light passed through an OS-14 orange filter and a set of neutral filters. The corresponding exposures were 1/60–3 s. The materials obtained during the eclipse and the films with the absolute and relative calibrations were developed simultaneously (for the process C-41 at 36°C).

3.3. Digitizing

The films were digitized using a Perkin–Elmer 1010 GM microdensitometer at the Korea Astronomy Observatory, enabling us to measure the coordinates and optical density of the image elements. A slit of size 0.01×0.01 mm^2 corresponds to $6'' \times 6''$ on the film. We scanned along both coordinates in steps of 0.01 mm, with the scanned area of each frame equal to 701×701 pixels. We scanned the photometric-wedge and quartz-attenuator fields over an area of 200×200 pixels.

3.4. Photometry

We constructed a characteristic curve from measurements of the 21-step wedge with a logarithmic brightness gradient $\log I = 0.15$. Our previous experience working with photoemulsions has shown that, in the underexposed region and linear interval, the characteristic curve can be approximated very well by the function $D_{ap} = D_0 + \gamma \log(J + e^{-J})$, where $J = I/I_0$. We found the function D_{ap} by searching for and testing expressions satisfying the facts that $D \sim I^2$ in the underexposed region and $D \sim \log I$ in the linear interval of the characteristic curve.

Fifteen wedge fields, corresponding to density variations by two orders of magnitude in the coronal image at distances of $1.1–1.5R_\odot$, were sufficient to make the transformation from densities to intensities. We obtained a least-squares fit for three approximation parameters of the developed emulsion—the background density D_0, contrast γ, and so-called sensitivity $1/I_0$—using the 15 wedge fields. In the case under consideration, the mean-square density residual was ~0.012. The measured mean background was in agreement with the calculated value of D_0 with accuracy to 0.01, which is within the detected irregularity of the background over the emulsion.

An exact inversion of $D_{ap} \equiv D_{ap}(J)$ to the function $J(D_{ap})$ can be carried out only iteratively. A sufficiently good approximation with an error $\delta J/J < 0.6\%$ that is acceptable for a photographic process is given by the expression

$$J(D_{ap}) = \sqrt{x^2 - 1} + \frac{x - 1}{x^2 + 4x - 2}, \quad x = 10^{(D_{ap} - D_0)/\gamma},$$

which we used in the computer reduction of the data.

4. ALGORITHM FOR CONSTRUCTING THE POLARIZATION IMAGES

The polarization pattern is repeated cyclically after a half turn of the polaroid (i.e., in our case, after 12 frames). Flare spots are unavoidable in a multi-component optical system, which result in a modulation of the signal at the polaroid rotation frequency due to the large brightness gradients in the corona. Therefore, we separated the polarization film of the white-light corona we obtained into several series containing 24 successive frames, corresponding to a complete rotation of the polaroid. We selected only one series centered relative to the center of totality for subsequent processing. All frames of this series were processed simultaneously in order to suppress the instrumental contribution.

We used the IDL software in the data reduction. The optimal procedure for mutual registration of the frames proved to be blink comparison with visual control on a display screen. We measured the background of each frame in two corners free of the image emission and averaged over an area of 50×50 pixels.

After centering 24 successive frames, we obtained an image of the corona averaged over the density $\mathbf{D} \equiv D(i, j)$, where i and j are the integer Cartesian coordinates of an image pixel with the coordinate origin at the center of the solar disk. We later used the density distribution in this frame as an indicator of the noise level in various statistical procedures.

Transforming the densities into intensities yielded a succession of frames $\mathbf{S}_k$, which contain information on the distribution of the polarization parameters. There are three such parameters for partially linearly polarized sources: the intensity I, degree of polarization P, and orientation of the plane of polarization χ. However, using these parameters *before* applying statistical procedures leads to systematic errors (biased estimates). On the other hand, a set of parameters in the form of the Stokes vector does not suffer from this drawback. The first parameter of this set is the same intensity $I = I_* + I_\updownarrow$, which is a sum of the intensities of the unpolarized I_* and linearly polarized $I_\updownarrow$ components of the light flux. Two other parameters are the sign-variable quantities Q and U. They are the projections of the linearly polarized component onto the axes of an arbitrarily chosen Cartesian coordinate system in the image plane. Q and U can be interpreted as the projections of a vector with length $I_\updownarrow = \sqrt{Q^2 + U^2}$ and orientation φ given by the expression $\tan\varphi = U/Q$. Then, the degree of linear polarization is $P = I_\updownarrow/I$, and the angle of the plane of polarization is defined to be $\chi = \varphi/2$.

In accordance with Malus' law, partially linearly polarized light (I, Q, U) will have the following intensity after passage through an ideal polaroid:

$$S \sim I_* + 2I_\updownarrow \cos^2(\chi - \alpha)$$

$$= (I_* + I_\updownarrow) + I_\updownarrow \cos(2\chi - 2\alpha) = I + Q\cos 2\alpha + U \sin 2\alpha,$$

where α is the orientation of the polaroid plane of polarization in the same coordinate system in which the angle χ is defined. From here on, we shall consider the intensities I, Q, and U as functions of the coordinates (i, j) introduced above; i.e., we shall consider the frames $\mathbf{I} \equiv I(i, j)$, $\mathbf{Q} \equiv Q(i, j)$, and $\mathbf{U} \equiv U(i, j)$. In our experiment, the polaroid plane of polarization changed by the con-

stant value 360°/24 = 15° between successive frames, so that $\alpha_k = \alpha_0 + \pi k/12$ for the kth frame. Here, α_0 is the orientation of the polaroid plane in the first frame.

Thus, we can use results for 24 successive frames $\mathbf{S}_k$ to write the 24 equations

$$\mathbf{S}_k \equiv \mathbf{S}_k(i, j) = \mathbf{I} + \mathbf{Q}'\cos\frac{\pi k}{12} + \mathbf{U}'\sin\frac{\pi k}{12},$$

$$k = 0, 1, \ldots, 23,$$

for each pixel with the coordinates (i, j). Here, the vector $(\mathbf{Q}', \mathbf{U}')$ is related to the vector $(\mathbf{Q}, \mathbf{U})$ via a rotation through the angle $2\alpha_0$, which is not known in advance with sufficient accuracy:

$$\begin{pmatrix} \mathbf{Q}' \\ \mathbf{U}' \end{pmatrix} = \begin{pmatrix} \cos 2\alpha_0 & \sin 2\alpha_0 \\ -\sin 2\alpha_0 & \cos 2\alpha_0 \end{pmatrix}\begin{pmatrix} \mathbf{Q} \\ \mathbf{U} \end{pmatrix};$$

$$\begin{pmatrix} \mathbf{Q} \\ \mathbf{U} \end{pmatrix} = \begin{pmatrix} \cos 2\alpha_0 & -\sin 2\alpha_0 \\ \sin 2\alpha_0 & \cos 2\alpha_0 \end{pmatrix}\begin{pmatrix} \mathbf{Q}' \\ \mathbf{U}' \end{pmatrix}.$$

The least-squares solution of the system of equations $\mathbf{S}_k$ with respect to $\mathbf{I}$, $\mathbf{Q}'$, and $\mathbf{U}'$ has the form

$$I = \frac{1}{24}\sum_{k=0}^{23}\mathbf{S}_k, \quad \mathbf{Q}' = \frac{1}{12}\sum_{k=0}^{23}\mathbf{S}_k\cos\frac{\pi k}{12},$$

$$\mathbf{U}' = \frac{1}{12}\sum_{k=0}^{23}\mathbf{S}_k\sin\frac{\pi k}{12}.$$

Due to the presence of large brightness gradients in the corona, subsequent statistical procedures associated with spatial smoothing in regions of small densities (where the noise associated with the photographic processes can reach ±100% of the polarization amplitude) are carried out more efficiently using frames of the type

$$\mathbf{q}' \equiv q'(i, j) = \mathbf{Q}'/\mathbf{I} \quad \mathbf{u}' \equiv u'(i, j) = \mathbf{U}'/\mathbf{I}.$$

These quantities are the sign-variable components of the degree of polarization, whose absolute value is $\mathbf{P} = \sqrt{\mathbf{q}^2 + \mathbf{u}^2}$. In contrast to $\mathbf{Q}'$ and $\mathbf{U}'$, the gradients in the $\mathbf{q}'$ and $\mathbf{u}'$ frames are usually expected to be small. We should emphasize that smoothing a $\mathbf{P}$ frame in the presence of noise inevitably results in overestimated (biased) polarization values. The spatial structure of the $\mathbf{q}'$ and $\mathbf{u}'$ frames is substantially simplified if we assume that the coronal emission is polarized due to scattering by electrons and a finely-dispersed aerosol. In this case, the plane of polarization is always perpendicular to the scattering plane and to the radius vector of a scattering point in the plane of the sky. In the ideal case, a transformation to a coordinate system (specific for each image point) in which one axis is always directed toward the center of Sun leads to a zero radial projection of the polarization vector, while the tangential projection coincides with the absolute value of the polarization vector. In the presence of measurement noise, this remains valid for the mathematical expectations of the projections. On the other hand, this property is violated if regions of anomalous polarization are present in the corona [6–8].

We can transform to the local coordinates of the polarization vector by rotating the vector $(\mathbf{q}', \mathbf{u}')$ through the angle $2\psi \equiv 2\psi(i, j)$. It can easily be shown that $\cos 2\psi = \frac{i^2 - j^2}{\sqrt{i^2 + j^2}}$, and $\sin 2\psi = \frac{2ij}{\sqrt{i^2 + j^2}}$. For example, the tangential $\mathbf{t}'$ and radial $\mathbf{r}'$ frames can be obtained from the Cartesian projections $\mathbf{q}'$ and $\mathbf{u}'$ via the transformation

$$\begin{pmatrix} \mathbf{t}' \\ \mathbf{r}' \end{pmatrix} = \begin{pmatrix} \cos 2\psi & \sin 2\psi \\ -\sin 2\psi & \cos 2\psi \end{pmatrix}\begin{pmatrix} \mathbf{q}' \\ \mathbf{u}' \end{pmatrix}.$$

Recall that we introduced the primed quantities because the initial orientation of the polaroid α_0 was uncertain.

Assuming that the radial component of the polarization averaged over the corona, $\langle\mathbf{r}\rangle$, must equal zero, the angle α_0 is given by the expression $\tan 2\alpha_0 = \langle\mathbf{r}'\rangle/\langle\mathbf{t}'\rangle$. The corresponding rotation of the $(\mathbf{t}', \mathbf{r}')$ frames through the angle $2\alpha_0$ transforms them into the $(\mathbf{t}, \mathbf{r})$ frames with zero mean $\mathbf{r}$.

To calculate the mean values $\langle\mathbf{r}'\rangle$ and $\langle\mathbf{t}'\rangle$, we used only regions of the coronal image in which the densities in the averaged frame $\mathbf{D}$ were in the interval 0.2–0.8. We estimated the actual level of the "polarization" noise in various coronal zones from the level of fluctuations in the radial component in the $\mathbf{r}$ frame. These fluctuations were well correlated with the density in the $\mathbf{D}$ frame. To suppress the noise, we used a parametric procedure for the calculation of moving smoothed values for the t and r frames. Each pixel in the $\mathbf{t}$ and $\mathbf{r}$ frames was assigned a value averaged over a square of $(2k + 1) \times (2k + 1)$ pixels with its center in the current pixel. The smoothing parameter k was determined by the density in the corresponding pixel of the $\mathbf{D}$ frame, which was previously smoothed over a 66″ × 66″ square. The dependence of k on the density interval in the $\mathbf{D}$ frame was found empirically, checking the level of fluctuations in the r frame; the following parametrization in k was used:

$$D_\infty \longleftarrow 1 \longrightarrow D_{0.3} \longleftarrow 2 \longrightarrow D_{0.15} \longleftarrow 3$$
$$\longrightarrow D_{0.10} \longleftarrow 5 \longrightarrow D_{0.03} \longleftarrow 10 \longrightarrow D_0.$$

5. RESULTS

Figure 3 presents an image of the deviation of the plane of polarization from the radial direction for the solar coronal emission on August 11, 1999 in the near-infrared at distances of $\leq 1.5R_\odot$. As noted above, the accuracy of the orientation of this plane is ≤1°. North is at the top, and East is to the left. A relative color scale

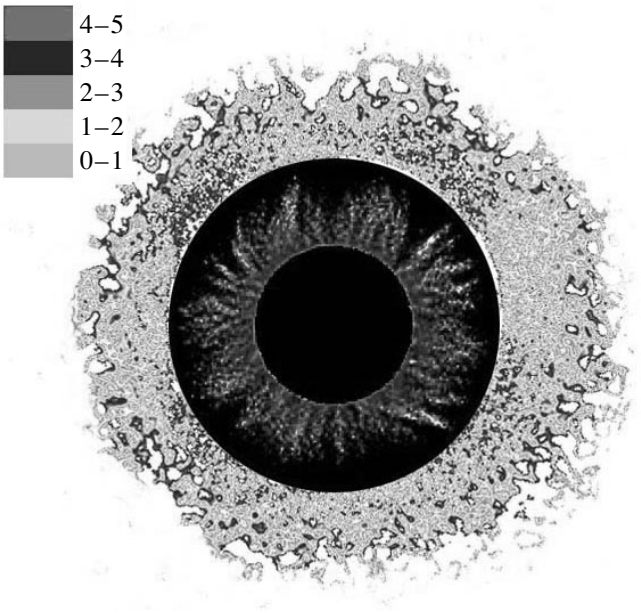

Fig. 3. Orientation of the plane of polarization for coronal emission in the near-infrared continuum. A relative color scale for the deviation of the polarization plane from the radial direction in degrees is given in the left upper corner. A picture of the coronal structure is superposed on the lunar disk.

for the absolute values of the deviation angles in degrees is given in the left upper corner. Superposed on the image of the Moon is a picture of the coronal structure constructed during our reduction of a series of differing exposures of the corona, obtained at the same observing site with the same spatial resolution using an MS 3M-5SA photographic objective (F = 500 mm, 1/8) and the same type of spectrozonal infrared aerial photofilm (the observer was N. L. Krusanova). The position angles were aligned with an accuracy of 0.5°. We used the knots of a high-altitude active prominence at the SW limb as reference points. The actual spatial resolution, determined by blurring at the Moon's limb, was equal on average to 15″–20″.

Both large-scale and small-scale structures in the distribution of the deviation angles can clearly be traced in Fig. 3. Comparison with the coronal structure leads to the following conclusions. The polar and equatorial regions are characterized by a diffuse and almost uniform structure, corresponding to angles 0.5° ± 0.5°, in agreement with the van de Hulst model. Individual occasional filamentary and quasi-pointlike structures with angles 1°–3° do not appreciably affect the general pattern.

There are four large-scale regions over the NE, SE, SW, and NW limbs covering a position-angle range of about 60° that are characterized by angles of 1°–3°. These regions include small-scale structures with sizes up to 30″ with deviation angles of 4°–5°. In particular, multiple points with angles of 4°–5° observed in the NE sector to heights of $0.17R_\odot$ (≈100 000 km) over the limb clearly follow curved coronal streamers to distances of $1.6R_\odot$. This coronal region is characterized by the presence of coronal condensations and bright loop H_α prominences.

As was shown by Molodensky [9], scattering of photons by moving electrons rotates the plane of polarization due to aberration of the light in the coordinate system moving with the electron flow. Consequently, deviations of the plane of polarization from the radial direction reflect the presence of high-speed electron flows. This deviation is equal to $\delta = v_t/c$, where v_t is the velocity component tangent to the limb and c is the speed of light. His search for such angle deviations in eclipse data led Koutchmy *et al.* [15] to conclude that there were no deviations exceeding 1° in the inner corona at distances below $1.5R_\odot$.

However, our measurements in the inner corona indicate that the component of the electron flow velocity tangent to the limb can reach 2.6×10^3 km/s in the polar and equatorial regions, 10^4 km/s in large-scale structures centered on the boundaries of coronal streamers or tracing strongly-curved streamers, and 2.6×10^4 km/s in individual small-scale structures with sizes below 30″ localized in active regions.

6. CONCLUSION

We have presented the results of our determination of the plane of polarization for emission from inner regions of the solar corona to distances of $<1.5R_\odot$ in the near-infrared continuum (570–800 nm). These measurements have a spatial resolution of 15–20″ and yield an accuracy of the plane of polarization of ≤1°. To our knowledge, these results for the orientation of the plane of polarization for the white-light corona are the most accurate made thus far. We were able to achieve an accuracy of ≤1° by implementing the following techniques:

(a) decreasing the instrumental background level (due primarily to scattering of light from the bright inner corona by the entrance aperture) by using the classic coronographic method of Lyot;

(b) installing a polaroid near the plane of the Lyot aperture, which results in averaging of the polaroid characteristics over a surface with a diameter of 9 mm;

(c) developing a special algorithm for statistical reduction of the numerical images using the IDL software package, based on representing the light in terms of the Stokes parameters.

Assuming the existence of moving electrons, the observed deviations of the plane of polarization from the radial direction suggest that the electron energies can reach 2×10^3 eV. A careful comparative analysis of the fine coronal structure and the distribution of the degree of polarization enabling us to calculate the electron density and, thereby estimate the currents in the

upper solar atmosphere, will be presented in a future paper.

ACKNOWLEDGMENTS

Our polarimetric studies of the upper solar atmosphere were supported by the Russian Foundation for Basic Research (project code 99-02-18430) and INTAS–RFBR (project code 97-IR-1088) (97-02-71029). Development of the apparatus was supported by an Astronomy grant of the Federal Scientific and Technical Program (project no. 2.1.4.2). We are grateful to our collaborators from the Sternberg Astronomical Institute of Moscow State University E. A. Kolezhonkov and G.D. Stanilovskiĭ for their help in preparing some of the mechanical units of the portable cinecoronographic polarimeter. We are especially grateful to our colleagues from the Institute of Astronomy of the Bulgarian Academy of Sciences for their assistance in preparing for the expedition.

REFERENCES

1. J. O. Stenflo, in *The Last Total Solar Eclipse of the Millenium in Turkey*, Ed. by W. Livingston and A. Ozguc, Astron. Soc. Pac. Conf. Ser. **205**, 41 (2000).
2. I. S. Kim, in *Advances in Solar Research at Eclipses, from Ground and from Space*, Ed. by J.-P. Zahn and M. Stavinski (Kluwer, Dordrecht, 2000), NATO ASI Ser., Ser. C **558**, 67 (2000).
3. B. Lyot, C. R. Acad. Sci. **99**, 580 (1930).
4. O. G. Badalyan, M. A. Livshits, and J. Sykora, Astron. Zh. **74**, 767 (1997) [Astron. Rep. **41**, 682 (1997)].
5. K. Saito, Publ. Astron. Soc. Jpn. **11**, 234 (1959).
6. G. M. Nikol'skiĭ and A. A. Sazanov, Astron. Zh. **47**, 1038 (1970) [Sov. Astron. **14**, 831 (1970)].
7. S. Koutchmy and K. H. Schatten, Sol. Phys. **17**, 117 (1971).
8. G. M. Nikolsky, A. A. Sazanov, and A. K. Kishonkov, Sol. Phys. **53**, 79 (1977).
9. M. M. Molodensky, Sol. Phys. **28**, 465 (1973).
10. M. M. Molodenskiĭ, Soln. Dannye, No. 8, 63 (1974).
11. A. K. Kishonkov and M. M. Molodensky, Sol. Phys. **42**, 341 (1975).
12. M. A. Vashakidze, *Results of an Expedition to Observe the Total Solar Eclipse of September 21, 1941* (Akad. Nauk SSSR, Moscow, 1941), p. 186.
13. E. P. Ney, W. F. Hych, R. W. Maas, *et al.*, Astrophys. J. **132** (3), 812 (1960).
14. V. Kulidzhanishvili, A. K. Mayer, V. A. Mayer, and S. V. Danik, in *Solar Coronal Structures (IAU Colloquium 144)*, Ed. by V. Rusin, P. Heinzel, and J.-C. Vial (VEDA Publ. Comp., Bratislava, 1994), p. 529.
15. S. Koutchmy, M. M. Molodenskiĭ, G. M. Nikol'skiĭ, and B. P. Filippov, Astron. Zh. **70**, 563 (1993) [Astron. Rep. **37**, 286 (1993)].
16. I. S. Kim, O. I. Bugaenko, I. A. Bilenko, *et al.*, Izv. Vyssh. Uchebn. Zaved., Radiofiz. **39** (11), 1298 (1996).
17. I. S. Kim, O. I. Bugaenko, I. A. Bilenko, *et al.*, *Solar Data: Articles and Communications 1995–1997* (1997), p. 145.

Translated by Yu. Dumin

Astronomy Reports, Vol. 45, No. 9, 2001, pp. 738–745. Translated from Astronomicheskiĭ Zhurnal, Vol. 78, No. 9, 2001, pp. 849–858.

The Structure of the Global Solar Magnetic Field Excited by the Turbulent Dynamo Mechanism

V. N. Krivodubskiĭ

Astronomical Observatory, Shevchenko Kiev National University, ul. Glushkova 6, Kiev, 252127 Ukraine

Received January 5, 2001

Abstract—A mixing-length approximation is used to calculate $K\lambda$ for a Parker dynamo wave excited by the dynamo mechanism near the base of the solar convection zone (K is the wave number of the dynamo wave and λ the extent of the dynamo region). In a turbulent-dynamo model, this number characterizes the modes of the global magnetic field generated by a mechanism based on the joint action of the mean helical turbulence and solar differential rotation. Estimates are obtained for the helicity and radial angular-velocity gradient using the most recent helioseismological measurements at the growth phase of solar cycle 23. These estimates indicate that the dynamo mechanism most efficiently excites the fundamental antisymmetric (odd), dipole, mode of the poloidal field ($K\lambda \approx -7$) at low latitudes, while the conditions at latitudes above 50° are more favorable for the excitation of the lowest symmetric (even), quadrupole, mode ($K\lambda \approx +8$). The resulting north–south asymmetry of the poloidal field can explain the magnetic anomaly ("monopole" structure) of the polar fields observed near solar-cycle maxima. The effect of α quenching increases the calculated period of the dynamo-wave propagation from middle latitudes to the equator to about seven years, in rough agreement with the observed duration of the solar cycle. © *2001 MAIK "Nauka/Interperiodica".*

1. INTRODUCTION

Magnetographic studies indicate that the poloidal field of the Sun can usually be described by a simple dipole that has asymmetric polarity with respect to the equator. However, at recent solar-activity maxima, both poles of the poloidal magnetic field had the same sign: the reversals of the northern and southern polar fields occurred one to two years apart. To account for this magnetic anomaly, some investigators have suggested that a quadrupolar mode of the poloidal field (magnetically symmetric about the equatorial plane) was dominant at those epochs [1, 2]. According to the model calculations by Parker based on the turbulent dynamo mechanism [3], the excitation thresholds for the dipole and quadrupole modes of the global field are very close. For this reason, excitation of the quadrupolar mode due to random factors, or, more likely, changes in the physical conditions in the solar interior, cannot be ruled out. For example, helioseismological measurements suggest that regions with different angular velocities of rotation can exist inside the Sun. Here, we use turbulent-dynamo theory and recent helioseismological measurements of the rotational velocity of the solar interior to investigate the possibility of exciting the quadrupolar mode of the poloidal magnetic field at a specified phase of the activity cycle.

Helioseismological data [4–9] testify that the rotational pattern depends strongly on both depth in the solar convection zone (SCZ) and heliographic latitude. The regular velocity field in the SCZ can be divided into domains of fast (equatorial) and slow (polar) rotation, with different signs of the radial angular-velocity gradient $\partial\Omega/\partial r$. The angular velocity decreases with depth ($\partial\Omega/\partial r > 0$) near the equator and, in contrast, increases with depth near the poles ($\partial\Omega/\partial r < 0$). The transition from fast to slow differential rotation occurs in the relatively narrow latitude zone 40°–50° with a radius-independent angular velocity; this zone separates the SCZ in each hemisphere into two spatial domains with opposite signs of $\partial\Omega/\partial r$. Moreover, in a relatively thin layer near the base of the SCZ [10, 11], known as the *tachocline*, the latitudinally differential rotation sharply changes into almost uniform rotation of the radiative zone, with an angular velocity typical of the SCZ at latitudes 40°–50°. Finally, the recent helioseismological discovery of substantial temporal and spatial angular-velocity variations in the SCZ [8, 9] was quite unexpected.

During the four and a half years from May 1995 to November 1999, at the growth phase of solar cycle 23, two independent research teams carried out complementary, nearly continuous helioseismological measurements of the Doppler velocity field over the entire solar disk. The first team conducted observations using the GONG (Global Oscillation Network Group) ground-based network of six observatories, while the other used the Michelson Doppler Imager (MDI) aboard the SOHO space station. Solving for the rotational splitting of the frequencies for acoustic and gravity (p and f) global-oscillation modes enabled the detection near the tachocline of appreciable *time variations* in the angular velocity Ω about its mean values over 4.5 years [8].

1063-7729/01/4509-0738$21.00 © 2001 MAIK "Nauka/Interperiodica"

Near the equatorial plane, the amplitude of variations in the residual angular velocity $\delta\Omega$ has a period of ~1.3 years and reaches 6 nHz, whereas, at high latitudes, this period decreases to one year and the amplitude increases to 12 nHz. It is also interesting that the time variations in the angular velocity are in antiphase at fixed points of the solar radius above and below the tachocline.

Another important result of these observations has to do with the structure of coupled zonal streams with velocities of up to 600 cm/s ($\delta\Omega \sim 1.5$ nHz), which migrate from the poles to the equator over 22 years. This structure is usually determined from direct Doppler observations of the solar surface (so-called torsional oscillations). However, helioseismological measurements [9] show that it extends inward in the SCZ to depths of at least 60 Mm ($r \approx 0.92R_\odot$), which is much deeper than 35000 km where the angular velocity reaches its maximum value in the layer of negative radial shear at low and middle latitudes. Systematic *time variations* in the residual rotational velocity $\delta\Omega$ were also detected for subphotospheric oscillations. In the equatorial plane, the angular velocity Ω continuously decreased during the 4.5-year interval, while a transition to a more complex pattern of faster rotation was noted at higher latitudes.

Obviously, in view of the magnetic nature of dynamical variations within the SCZ, changes in the strong toroidal magnetic field in the course of the solar cycle should primarily perturb the parameters of the low-energy turbulence—the eddy viscosity and, especially, the turbulent-convection helicity, which is the most ordered. Unfortunately, even the unperturbed values of the turbulence parameters deep in the SCZ cannot be determined using currently available techniques. At the same time, helioseismology, which has already proven itself a powerful tool for studies of the interior rotation, has recently demonstrated its use in identifying spatial and temporal variations in the regular velocity field. Detailed numerical models of the SCZ taking into account variations of the turbulence parameters as functions of the magnetic induction have not been calculated (and it is not quite clear what kind of magnetic field should be considered—small-scale or large-scale, continuous, fragmented, or intermittent). At the same time, the influence of rotation and large-scale magnetic field (the excitation of macroscopic magnetism by helical turbulence) in convective envelopes was studied by solving MHD equations. Rotation leads to the tensor nature of the helicity parameter, while the magnetic field causes the generation to slow down (α quenching) [12]. Moreover, our computations show that the helicity parameter changes sign near the base of the SCZ [13], since the contributions to this parameter from radial plasma-density inhomogeneities and turbulent pulsations vary with depth. In this region, the large-scale magnetic field also significantly inhibits the turbulence diamagnetism acting against the magnetic buoyancy [14], which is important for estimates of the magnetic fields retained near the base of the SCZ.

Therefore, it is important to concentrate on the question of how the specific features of the interior rotation detected in helioseismic measurements, together with the variations in the helicity and turbulence-diamagnetism parameters deep in the SCZ revealed by solutions to the MHD equations, affect the conditions in which the turbulent dynamo operates. We now turn to the question of how these factors can be reflected in the structure of the global magnetic field that is generated.

2. A TURBULENT DYNAMO AND THE MODES OF THE GLOBAL SOLAR MAGNETIC FIELD

It is currently believed that the axisymmetric global magnetic field $\mathbf{B}$ of the Sun consists of two components–a stronger toroidal (azimuthal) field $\mathbf{B_T}$ stretched along the solar parallels and a weaker poloidal (meridional) field $\mathbf{B_P}$, which is mainly localized at middle and low latitudes on both sides of the equator, and is observed mainly in polar regions [15–17]. The observed regularities of solar magnetic activity testify that the poloidal and toroidal fields are coupled and are evidently generated by a single process, with the 22-year magnetic cycle being the physical basis of solar activity. The most widespread view is that a turbulent magnetic dynamo acts as the trigger for the solar cycle. This dynamo is localized in the SCZ, where the interaction between rotation and convection produces a combination of rotational inhomogeneity and helical turbulent convection [15, 16].

We introduce a spherical coordinate system (r, θ, φ) with its origin at the center of a sphere of radius $R_\odot$ and its polar axis directed along the rotational axis of the Sun (the heliographic latitude θ^* often used by observers is $90° - \theta$). The vector magnetic fields in a spherical region can be described by surface and radial spherical functions; the components $\mathbf{B_P}$ and $\mathbf{B_T}$ can thus be represented by sums of individual fields corresponding to particular degrees of multipolarity of spherical functions: $l = 1$, dipole; $l = 2$, quadrupole; $l = 3$, octupole; etc. [17]. The degree of multipolarity l characterizes the dependence of the field structure on the polar angle θ and azimuth φ, giving the number of nodal (zero) lines (circles on the spherical surface) where the sign of the magnetic field changes. In the case of axial symmetry, when the field configuration is independent of azimuth φ (zero azimuthal order for the spherical functions, $m = 0$), the nodal lines will be parallel to the equator, dividing the solar surface into $l + 1$ latitude zones with definite magnetic-field signs (polarities).

The observed manifestation of the structure of the surface global magnetism is the distribution of unipolar magnetic fields, whose boundaries are defined by prominences, filaments, filament channels, and plage couloirs. These distributions are used to construct H_α maps of the polarity (sign) of the radial magnetic-field component [18]. Another source of information about

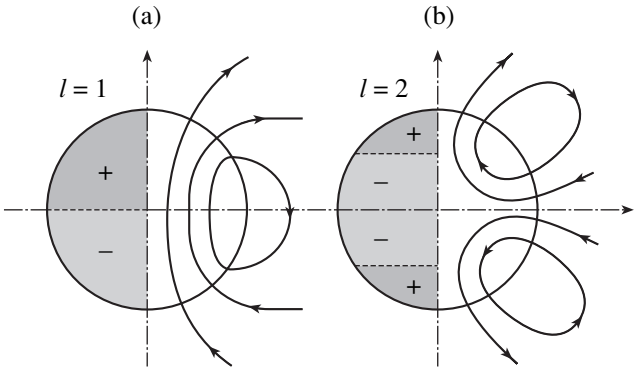

Fig. 1. The fundamental antisymmetric (A0) and symmetric (S0) poloidal-field modes excited by the αΩ process. (a) right: dipole field lines (the first odd term in the poloidal-field expansion), left: dipole latitude zones with positive (+) and negative (–) polarities of the surface (background) field ($l + 1 = 2$); (b) right: quadrupole field lines (the first even term in the poloidal-field expansion), left: quadrupole latitude zones with positive (+) and negative (–) polarities of the surface field ($l + 1 = 3$).

the sign of the surface field is magnetographic observations. Analyses of the zonal structure of large-scale photospheric magnetic fields based on Mt. Wilson magnetographic observations [19] and H_α maps [20] indicate that the degree of the latitude zonal mode l on the solar surface can range from one to nine at different phases of the cycle.

A model with a turbulent dynamo generating a mean (global) magnetic field through the combined action of helical (cyclonic) turbulence and solar differential rotation was first suggested by Parker [21], who called his solutions to the magnetic-induction equations in the form of migratory waves of magnetic field "dynamo waves." The observed migration of bipolar magnetic regions and high-latitude carriers of weak magnetic fields in the course of the solar cycle can be accounted for in dynamo models if the angular velocity of rotation Ω varies with radius in the SCZ.

Accordingly, if we take into account only the radial shear $\partial\Omega(r, \theta)/\partial r$ in the regular velocity field $\mathbf{V}(r, \theta) = \Omega(r, \theta) \times \mathbf{r} = r\sin\theta\Omega(r, \theta)\,\mathbf{i}_\varphi$ (where r is distance from the center of the Sun), the induction equation describing the evolution of the global magnetic field in the kinematic problem can be broken down into two equations [15–17, 21]:

$$\partial\mathbf{A}/\partial t = \alpha\mathbf{B_T} + D_T\Delta\mathbf{A}, \quad (1)$$

$$\partial\mathbf{B_T}/\partial t = r\sin\theta(\mathbf{B_P}\nabla)\Omega\mathbf{i}_\varphi + \mathrm{curl}(\alpha\mathbf{B_P}) + D_T\Delta\mathbf{B_T}. \quad (2)$$

Here, $\mathbf{A}$ is the toroidal vector potential ($\mathbf{B_P} = \mathrm{curl}\,\mathbf{A}$); $\mathbf{i}_\varphi$ is an azimuthal unit vector; $\nabla \equiv \partial/\partial r$, $\alpha \cong -(\tau/3)\langle\mathbf{u} \cdot \mathrm{rot}\,\mathbf{u}\rangle \cong -(2/3)\Omega l^2\nabla\ln(\rho v_r)$ is the parameter of the mean helicity (gyrotropy) of the turbulent motion (helicity necessarily arises in a rotating turbulent (convecting) plasma with nonuniform density ρ); $\mathbf{u}$, τ, and l are the velocity vector, the characteristic time for turbulent pulsations, and their mean mixing length, respectively; v_r is the radial component of the rms turbulent velocity $v = \langle\mathbf{u}^2\rangle^{1/2}$; $\nabla \equiv \partial/\partial r$, $D_T = \nu_m + \nu_T = c^2/4\pi\sigma_T\mu_T$ is the magnetic eddy diffusivity; $\nu_m = c^2/4\pi\sigma$ and $\nu_T \cong (1/3)vl$ are the magnetic and eddy viscosities, respectively, (in the solar plasma, $\nu_T \ll \nu_m$, so that $D_T \cong \nu_T$); σ and σ_T are the gas-kinetic and the eddy electrical conductivity, respectively; and μ_T is the magnetic eddy permeability. The action of the nonuniform rotation on the original poloidal field $\mathbf{B_P}$ generates a toroidal field $\mathbf{B_T}$ (the Ω effect); helical turbulence acts on this toroidal field, exciting a poloidal field with polarity opposite to that of the original field (the α effect), closing the solar dynamo cycle. The inductive effect of the solar differential rotation is several orders of magnitude stronger than the excitation of fields due to the α effect; therefore, the second term on the right-hand side of (2) can be neglected. Thus, we arrive at a system of equations describing the so-called αΩ mechanism for the generation of the global magnetic field [15–17, 21].

The simplest solutions to the system of induction equations (1), (2) are the antisymmetric mode A0 and symmetric mode S0 of the fundamental (first two) terms in the multipolar expansion, representing purely dipolar ($l = 1$) and purely quadrupolar ($l = 2$) fields (see Fig. 1 for an illustration of the basic modes of the poloidal field). Higher-degree multipoles ($l = 3, 4, 5, \ldots$) are similar to the dipole and quadrupole in terms of their symmetry about the equatorial plane. The field that is actually realized is determined by the particular conditions for the field excitation.

3. WAVE NUMBERS OF THE DYNAMO WAVES

Parker [3] suggested seeking solutions to the induction equations (1) and (2) in the form of dynamo waves migrating in the meridional direction:

$$C\exp[t/\tau - i(q\mathbf{Kr})], \quad (3)$$

where

$$K = (\alpha G/\nu_T^2)^{1/3} = N_D^{1/3}k \quad (4)$$

is the wave number of the dynamo wave, which characterizes the scale of the field variations. Here, k is the normal wave number, $q = k/K$ the dimensionless wave number, C an arbitrary constant, $N_D = \alpha G/\nu_T^2 k^3$ the dimensionless dynamo number, which reflects the intensity of the dynamo process, and $G = r\partial\Omega/\partial r$ a measure of the radially differential rotation. Substitution of the required wave-type form of solution into the system of dynamo equations (1) and (2) yields a dispersion relation (algebraic equation for the dimensionless wave number q) characterizing the dynamo effect:

$$(A + q^2)^2 - iq = 0, \quad (5)$$

where

$$A = 1/\tau\nu_T K^2 + k^2/K^2. \quad (6)$$

The rate of field production or annihilation is determined by the growth exponent

$$\mathrm{Re}(1/\tau) = \pm\left|\frac{1}{2}\alpha Gk\right|^{1/2} - \nu_T^2 k, \qquad (7)$$

whereas the oscillation frequency of the field ω is determined by

$$\mathrm{Im}(1/\tau) = \pm\left|\frac{1}{2}\alpha Gk\right|^{1/2} \quad (\text{for } \alpha Gk > 0), \qquad (8)$$

or

$$\mathrm{Im}(1/\tau) = \mp\left|\frac{1}{2}\alpha Gk\right|^{1/2} \quad (\text{for } \alpha Gk < 0).$$

Accordingly, the dynamo-wave period is

$$T = 2\pi/\omega = 2\pi\left|\frac{1}{2}\alpha Gk\right|^{1/2}. \qquad (9)$$

The direction of the meridional migration of the wave depends on the sign of the product αG [22]: for $\alpha G < 0$ [and $K < 0$, in accordance with (4)], the wave travels toward the equator (in the northern hemisphere); for $\alpha G > 0$ ($K > 0$), the wave travels poleward. A necessary condition for growth of the field is $|\alpha Gk| > 2\nu_T^2 k^4$, which acquires the very simple form $|N_D| > 2$ if the dimensionless dynamo number is used.

We note that, when treated using new analytical methods [23, 24], the Parker dynamo equations predict the existence of three dynamo waves of the solar magnetic field with different intensities, localizations, and directions, even for the same (negative) sign of the product αG. In a region extending over most of a solar hemisphere, the most intense, direct Parker dynamo wave travels toward the equator from high latitudes. However, the migration of the wave is opposite in the polar zone. Thus, at high latitudes ($\geq 80°$), an inverse Parker dynamo wave (incident polar wave) can be identified, which travels poleward and is much weaker than the direct wave. Finally, a third, even weaker, reflected polar wave propagates from the pole toward the equator, decaying exponentially as it travels from the pole. Here, we restrict our consideration to applying classic Parker techniques to the structure of the global magnetic field, leaving investigations of the evolution and dynamics of the fields using new methods to future analyses.

Parker [3] analyzed several spatially localized dynamo models in order to demonstrate the possibility of generating various magnetic-field modes under various excitation conditions. To simplify the model calculations, he considered a very thin spherical layer, which can be taken to be planar, and used a Cartesian rather than spherical geometry. From his solutions to the dynamo equations in a spherical and locally Cartesian coordinate system (with the radial direction chosen for the *x* axis, the azimuthal direction of rotation for the *y* axis, and north for the *z* axis), Parker found that quantitative

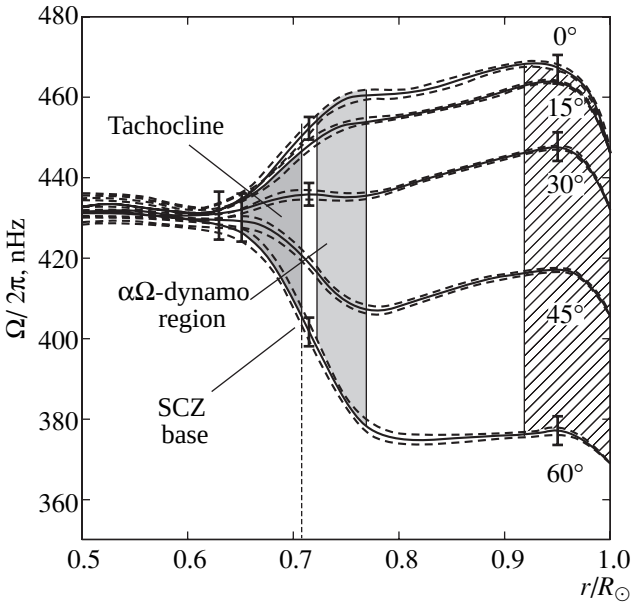

Fig. 2. Radial distribution of time-averaged (over 1995–1999) velocities of the interior rotation of the Sun for various latitudes, measured helioseismologically using the ground-based GONG network (from [8]). Directly above the base of the SCZ ($r \cong 0.71R_\odot$), in the tachocline [$r \approx (0.66–0.71)R_\odot$)], an abrupt transition from the latitudinally differential to almost uniform rotation of the radiative zone takes place. The vertical bars (for latitudes 0°, 30°, and 60°) mark the amplitudes of time variations in the angular velocity, which are in antiphase at fixed points above ($r = 0.72R_\odot$) and below ($r = 0.63R_\odot$) the tachocline. The period of these oscillations varies from ~1.3 years (in the equatorial plane, where $|\delta\Omega|$ is ~6 nHz) to ~1 year (at latitude 60°, where $|\delta\Omega| \sim$ 12 nHz). The shading at distances $(0.92–1.00)R_\odot$ indicates the region where the structure of the torsional oscillations is maintained. The vertical bars at $0.95R_\odot$ mark the range of time evolution of these oscillations over four years, $|\delta\Omega| \sim$ 5–6 nHz (results of observations on the GONG network and with MDI aboard the SOHO space station [9]). The region of efficient $\alpha\Omega$ generation studied here, $r \approx (0.73–0.77)R_\odot$, is also shown.

estimates for the relatively thin solar convective envelope are essentially independent of the geometry. It is important that stationary fields vanish in extended thin layers, while primarily oscillatory modes are excited. To determine the size of the rectangular dynamo region, Parker introduced the parameter λ describing the horizontal dimension of the dynamo region, which extends in the (meridional) *z* direction from the equatorial plane to the poles (see Fig. 3 in [3]). By definition, $\lambda > 0$ for the northern and $-\lambda < 0$ for the southern hemisphere. The parameter describing the vertical extent of the dynamo region is its thickness measured along a radius, which corresponds to a relatively thin sublayer of the convective envelope. The (larger) horizontal size of the dynamo region determines the efficiency of field generation and the (smaller) vertical size field dissipation.

The boundary conditions of the problem (field continuity at the equator and vanishing of the azimuthal

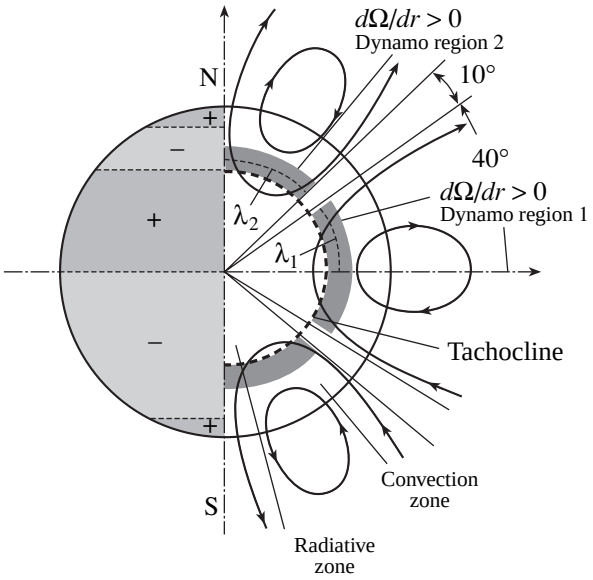

Fig. 3. Dipole and quadrupole poloidal-field modes excited by the αΩ-dynamo mechanism in the lower part of the SCZ (in the neighborhood of the tachocline) at the growth phase of activity cycle 23. Right: magnetic field lines of the dipole ($\theta^* \le 40°$) and quadrupole ($\theta^* > 50°$); left: the corresponding latitude zones of positive (+) and negative (–) magnetic polarity of the surface (background) field.

and latitudinal magnetic-field components at the poles) reduce the solution to separate treatments of the dispersion relations for the wave numbers $K\lambda$ of the even and odd dynamo-wave modes. The character of the excitation depends on $K\lambda$. By solving the dispersion relations, Parker found [3] that a stationary dynamo ($\mathrm{Im}(1/\tau) = \omega = 0$] is more likely for moderate $K\lambda$ ($|K\lambda| \approx 3$–6), while a tendency for the excitation of oscillatory fields ($\omega \neq 0$) can be observed as this number is increased.

Since we are primarily interested in periodic fields, we will consider in detail the requirements for the $K\lambda$ eigenvalues for which a global oscillatory magnetic field can be excited:

Odd modes (dipole, octupole, etc.):

for negative $K\lambda$:

$K\lambda = -7.43$ (dipole), –16.1 (octupole), – 24.8, –33.5, …

for positive $K\lambda$:

$K\lambda = +9.10$ (dipole), +17.8 (octupole), +26.5, +35.2, …

Even modes (quadrupole, etc.):

for positive $K\lambda$:

$K\lambda = +7.43$ (quadrupole), +16.1, +24.8, +33.5, …

for negative $K\lambda$,

$K\lambda = -9.10$ (quadrupole), +17.8, +26.5, +35.2, …

Clearly, for negative $K\lambda$, the fundamental odd (antisymmetric), i.e., dipole, mode can be excited most effectively, since it requires $K\lambda = -7.43$, whereas $K\lambda = -9.10$ is required for the excitation of the even (symmetric), i.e., quadrupole, mode. In contrast, the quadrupole mode is preferred for positive $K\lambda$, since it requires $K\lambda = +7.43$, which is smaller than the value $K\lambda = +9.10$ required for the dipole mode.

It is important that the excitation thresholds for the fundamental modes of the global field, A0 and S0 (dipole and quadrupole), do not differ greatly. Therefore, as already noted, excitation of the quadrupole mode due to small changes in the physical parameters of the SCZ cannot be ruled out. An important source of the information needed to resolve this question is helioseismic measurements, which provide invaluable data on spatial and temporal angular-velocity variations in the solar interior.

4. MODEL CALCULATIONS

The αΩ dynamo cannot operate in the upper region of the SCZ, since the field losses due to magnetic buoyancy are very large [16]. The overshoot layer near the base of the SCZ is believed to be most favorable for efficient dynamo action, due to two factors that facilitate the generation of strong fields in that region. First, the rate at which the magnetic field rises should be lowest in deep layers because of the high density there [16]. Second, diamagnetism due to the highly developed turbulence in the lower half of the SCZ counteracts magnetic buoyancy and, according to our studies [14, 25], can suppress the rising of especially strong magnetic fields over long times. Moreover, in the lower part of the SCZ, the relative radial gradient of turbulent pulsations, $\nabla v_r/v_r$, makes a larger contribution to the helicity parameter $\alpha \approx -(2/3)\Omega l^2 \nabla \ln(\rho v_r)$ than does the relative vertical gradient of the density, $\nabla\rho/\rho$. As a result, the α effect changes sign there from positive to negative (in the northern hemisphere) [13, 26]. In combination with the positive $\partial\Omega/\partial r$, this yields a negative product αG near the equator, which is necessary for dynamo waves to propagate toward the equator.

We add the following notes concerning the differential rotation to the above considerations. By analogy to the tachocline, we will refer to the region of a radius-independent angular velocity at latitudes 40°–50° extending from the solar surface to the radiative zone (of almost rigid rotation) as the "tachoconst." It plays a very important role in distributing the angular velocity in the solar interior, dividing the SCZ into domains of fast (dependent on distance from the rotational axis) and slow (dependent on distance from the equatorial plane) rotation with opposite signs of $\partial\Omega/\partial r$, in contact with the radiative zone. Obviously, the signs of the calculated dynamo wave numbers $K\lambda$ will be different in these domains. Therefore, the conditions for the dynamo effect should be studied for the deepest SCZ layers and for the two latitude ranges 0°–40° and 50°–90°. In our calculations, we will use the SCZ model of Stix [27].

We specify a rectangular local-dynamo region as follows. We consider a relatively thin convective layer of thickness $\Delta z \cong 30$ Mm ($\Delta r \cong 0.04 R_\odot$) in the lower part of the SCZ, at depths $z \cong$ ranging from 160 to 190 Mm, where the helicity parameter α is negative [13, 26]. Then, the midplane of the vertical extent of the dynamo region ($z \cong 175$ Mm) is located a distance $r_D \cong 5.2 \times 10^{10}$ cm from the center of the Sun, where the eddy viscosity is $\nu_T \cong 3 \times 10^{12}$ cm^2/s [14]. We define the meridional horizontal extent λ_1 of the low-latitude (equatorial) dynamo region as its size on the spherical surface r_D = const from the equator to the tachoconst, i.e., to the latitude $\theta^* = 40°$; specifically, $\lambda_1 \cong 2\pi r_D(40°/360°) \cong 3.6 \times 10^{10}$ cm. We will refer to this equatorial region as dynamo region 1 (DR1). Similarly, the extent of the high-latitude (polar) dynamo region 2 (DR2) from the tachoconst (latitude $\theta^* = 50°$) to the pole is $\lambda_2 \cong 3.6 \times 10^{10}$ cm.

We will now directly estimate $K\lambda$ for deep SCZ layers in a mixing-length approximation using our schematic rectangular dynamo model. To this end, we must average $\alpha(r, \theta)$ and $\partial\Omega(r, \theta)/\partial r$ over the vertical (radial) and horizontal (latitudinal) extents of the dynamo region in each domain. We will use here the values of these parameters at the points corresponding to depth $z \cong 175$ Mm and latitudes of 20° and 70° (the central latitudes of DR1 and DR2) as the average physical parameters.

To determine the magnitude and sign of $\partial\Omega(r, \theta^*)/\partial r$, we used helioseismological data obtained at the growth phase of activity cycle 23 (1995–1999) [8], in the form of curves representing the angular velocity averaged over the entire observation period as a function of the relative solar radius $r/R_\odot$ for five heliographic latitudes—0°, 15°, 30°, 45°, and 60° (Fig. 2), and interpolated these dependences. The angular-velocity curves were analyzed using the *Mathcad 2000* software package. To find the latitude distribution of the angular velocity, we constructed a 6×41 matrix of angular-velocity values along a radius in the SCZ for five latitudes. A harmonic analysis using the trapezia method was applied to these values to find the coefficients of the Fourier series for the given latitudes. The correlation between the experimental data and the values obtained from the Fourier series was 0.93–0.99 when sixth-order coefficients were used. The latitude-dependent (as the latitude cosine squared) Fourier coefficients of the polynomial regression were used to obtain continuous latitude dependences for the angular velocity. The Fourier series determines the angular-velocity distribution in polar coordinates (r, θ^*). According to these interpolations, in the region DR1, the radial decrease in angular velocity over depths 160–190 Mm in the 20° latitude plane is $\Delta\Omega \cong +3$ nHz, which corresponds to the radial gradient $\partial\Omega^{(1)}/\partial r \cong \Delta\Omega/\partial r \cong +3$ nHz/30 Mm $\cong +1 \times 10^{-9}$ nHz/cm = $+ 6.3 \times 10^{-18}$ rad/s cm. Accordingly, the magnitude of the differential rotation will be $G_1 \equiv r_D \partial\Omega^{(1)}/\partial r \cong +3.3 \times 10^{-7}$ rad/s.

The kinematic numerical simulations produced in a number of studies based on the $\alpha\Omega$-dynamo mechanism and the actual physical parameters of the SCZ reproduce well the basic observed regularities of the magnetic activity of the Sun. However, the dynamo-wave period T computed according to (9) is much shorter (about one year) than the observed mean duration of the solar cycle (about 11 years) [15, 28]. This compels searches for ways to lengthen the calculated dynamo-wave period. The main source of hope for this is nonlinear effects.

As shown by Rüdiger and Kichatinov [12, 29], a global magnetic field B that gives rise to turbulence anisotropy slows magnetic-field excitation via the α effect (so-called α quenching) and inhibits macroscopic diamagnetism in a nonuniform turbulent plasma. Magnetic quenching of field generation is described by the expression $\alpha(B) = \alpha_0 \Psi_\alpha(B)$ (where α_0 is the nonmagnetic value of the turbulence-helicity parameter and $\Psi_\alpha(B)$ is the quenching function normalized to unity at $B = 0$ [12]), whereas the suppression of turbulence diamagnetism is given by the expression $V_D(B) = 6V_\mu \Psi_D(B)$ (where $V_D(B)$ and $V_\mu = -\nabla\nu_T/2$ are the field-transport rates in the nonlinear and kinematic regimes, respectively, and $\Psi_D(B)$ is the diamagnetism-suppression function normalized to 1/6 at $B = 0$ [29]).

According to our calculations [25], turbulence diamagnetism is substantially inhibited in nonlinear regimes near the base of the SCZ, but even the reduced velocity of the downward field transport is sufficient to compensate the magnetic rising of strong fields. For this reason, strong magnetic fields (B ≅ 3000–4000 G) can be held there for a long time, substantially suppressing the α effect. The quenching function is ≅0.4 [26]; therefore, the helicity parameter α assumes much smaller values than predicted by calculations in the kinematic approximation. This means that α quenching will considerably lengthen the calculated dynamo-wave period. Moreover, the helicity parameter changes sign at a depth of 155 Mm (from positive to negative with increased depth in the solar interior) [13, 26], which is important in determining the direction of dynamo-wave propagation. According to our estimates taking into account α quenching, the azimuthal component of the helicity tensor, $\alpha_{\varphi\varphi}/\cos\theta \cong -(2/3)\Omega_0 l^2 \nabla \ln(\rho v_r)$ (where Ω_0 is the surface value of the angular velocity at the equator), reaches about -10^3 cm/s near the base of the SCZ [26]. If we adopt the mean value $\alpha_{\varphi\varphi} \cong -5 \times 10^2$ cm/s for $z \cong 175$ Mm, the helicity parameter at these depths at a latitude of 20° in domain DR1 will be $\alpha_1 = \alpha_{\varphi\varphi}\cos(90°–20°) \cong -2 \times 10^2$ cm/s.

Based on the estimates for all the necessary parameters, we can directly calculate the wave number $K\lambda$ of the dynamo wave in DR1 (for the northern hemisphere) to be

$$K_1\lambda_1 = (\alpha_1 G_1 \lambda_1^3/\nu_T^2)^{1/3} \approx -7,$$

which is close to the eigenvalue required for a dipole ($K\lambda = -7.43$) derived by Parker from the dispersion

relations. Thus the turbulent dynamo excites, first and foremost, the lowest antisymmetric oscillatory mode of the poloidal field—the dipole mode (Fig. 3). The intensity of the dynamo process is characterized by the dimensionless dynamo number N_D; as already noted, a necessary condition for the growth of the field is $|N_D| > 2$. The dynamo number can conveniently be represented in terms of the special magnetic Reynolds numbers $R_\alpha = \alpha_1\lambda_1/\nu_T$ and $R_\Omega = G_1\lambda_1^2/\nu_T$, which characterize the intensities of the α- and Ω effects, respectively: $N_D = R_\alpha R_\Omega$. A typical indication of the αΩ process is the condition $|R_\Omega| \gg |R_\alpha|$. According to our calculations, $|R_\alpha| \cong 2.5$, $|R_\Omega| \cong 140$, and $|N_D| \cong 350$, so that the physical parameters of the SCZ provide the conditions necessary for an αΩ dynamo in DR1. The radial shear $\partial\Omega^{(1)}/\partial r$ produces a strong two-ring toroidal field from the dipole field. Our estimates yield the following period for the propagation of the dynamo wave from latitude 40° to the equator ($K_1 < 0$):

$$T_1 = 2\pi/\left|\frac{1}{2}\sin(90°–40°)\alpha_1 G_1 k_1\right|^{1/2}$$

$$\approx 2\pi/\left|\frac{1}{2}\sin 50°(\alpha_1\partial\Omega^{(1)}/\partial r)(r_D/\lambda_1)\right|^{1/2} \approx 7 \text{ years},$$

in satisfactory agreement with the mean duration of the solar cycle (here, we have assumed $k_1 \approx 1/\lambda_1$).

In the polar domain, the radial nonuniformity of the rotation changes sign. Our estimates indicate that the radial gradient of the angular velocity within the field-generation region in the 70° latitude plane is $\partial\Omega^{(2)}/\partial r \cong -8 \times 10^{-18}$ rad/s cm ($G_2 \equiv r_D\partial\Omega^{(2)}/\partial r \cong -4 \times 10^{-7}$ rad/s), and the helicity parameter is $\alpha_2 \cong \alpha_{\varphi\varphi}[\Omega(r_D, 70°)/\Omega_0]\cos(90°–70°) \cong -3 \times 10^2$ cm/s. Therefore, the calculated wave number will be positive ($K_2\lambda_2 \approx +8$) in DR2, and the conditions will be more favorable for excitation of the fundamental symmetric, quadrupole mode (which, according to Parker, requires $K\lambda = +7.43$); see Fig. 3. In this case, the period for the dynamo wave's propagation toward the pole ($K_2 > 0$) is about half that in the equatorial domain.

5. DISCUSSION

Thus, the physical parameters of deep SCZ layers near the tachocline provide the conditions necessary for the αΩ process. A schematic model with a locally rectangular Parker dynamo taking into account the time-averaged interior rotation of the Sun suggests that the fundamental antisymmetric (odd) poloidal-field, dipole, mode can be excited more easily at low latitudes, whereas the conditions at latitudes higher than 50° are more favorable for the excitation of the lowest symmetric (even), quadrupole, mode. For this reason, the net poloidal field is asymmetric about the equatorial plane. In one—e.g., the northern—hemisphere, the poloidal field should be reduced at middle latitudes, where the magnetic field lines of the dipole and quadrupole are oppositely directed. At the same time, the poloidal field will be enhanced at middle latitudes in the southern hemisphere, since the dipole and quadrupole field lines have the same direction (see Fig. 5).

In this case, observations of large-scale magnetic structures should reveal a surface north–south asymmetry (anomaly)—three latitude zones of alternating magnetic polarity in the northern hemisphere and two such zones in the southern hemisphere, with the same polarity in both polar zones (Fig. 3). This "monopole" magnetic structure of the polar zones can account for the even symmetry of the polar magnetic fields with respect to the equator observed near the maxima of solar cycles.

Since the helicity of the turbulent convection is substantially inhibited by the global magnetism ($\Psi_\alpha \cong 0.4$), the calculated period of the dynamo wave's propagation from the middle latitudes to the equator is lengthened to about seven years, which agrees to order of magnitude with the observed mean duration of the sunspot cycle.

To compare our model calculations with observations, it is of interest to determine the surface structure of the poloidal field using the method of Yoshimura [28] and magnetic synoptic maps based on magnetographic observations. To this end, we divide the solar surface into 30 equal zones in latitude θ* and 36 sectors (of 10° each) in longitude (azimuth) φ, covering the entire solar disk with a grid of 1080 points. At each of these points, the observed field will be $\mathbf{B}(\theta^*, \varphi)$. The technique used to determine the surface poloidal field $\mathbf{B_P}(\theta^*)$ involves averaging the observed field $\mathbf{B}(\theta^*, \varphi)$ over longitude φ for a given latitude θ* according to the formula

$$B_P(\theta^*) = \frac{1}{2\pi}\int_0^{2\pi} B(\theta^*, \varphi)d\varphi \qquad (10)$$

(with the integration performed over all longitudes of the synoptic map). To reveal the asymmetry of the large-scale magnetism, the field observed during 1995–1999 should be averaged over many solar rotations (no fewer than 14 rotations, corresponding to a time span of about a year).

The appreciable time variations in the angular velocity (6–12 nHz) detected in recent helioseismological measurements over all latitudes near the base of the SCZ [8] are comparable with the angular-velocity decrease across the tachocline (Fig. 2), which opens new possibilities for the turbulent dynamo mechanism to explain variations in the magnetic asymmetry with the phase of the cycle. The coupled zonal flows deeply penetrating into the SCZ revealed by the same measurements [9] may be time-dependent phenomena related to the propagation of rotational disturbances from the interface between the radiation and convection zones to the solar surface and back, along magnetic field lines (torsional oscillations migrating inward in the Sun) [30].

Despite difficulties in the interpretation of magnetographic measurements, based on studies of oscillations of the overall magnetic field in time using the zero-resolution method, Severnyĭ [31] concluded that the spatial magnetic asymmetry of the Sun is a real phenomenon, and one of the most enigmatic problems in solar physics. It may be possible to resolve this problem if the regions with different angular velocities are magnetically isolated from one another [32, 33].

One of the leaders of the Kiev coronal-physics school V.I. Ivanchuk, who has studied relationships between the coronal structure and the N–S asymmetry of magnetic activity over the past 50 years based on observations of solar eclipses, suggested that two—a northern and southern—magnetic suns should be considered separately. Thus, from the standpoint of the generation of "northern and southern global magnetism," it would be interesting to derive the interior rotation of the Sun from helioseismological data separately for the northern and southern hemispheres.

ACKNOWLEDGMENTS

This work was partially supported by the State Foundation for Basic Research of the State Science Committee of Ukraine (project code 2.4/682). I am grateful to the graduate student P.G. Braiko (Astronomical observatory, Kiev National University) for assistance in processing the helioseismological measurements of the solar interior rotation using the *Mathcad 2000* software package, and also to V.I. Ivanchuk for useful discussions.

REFERENCES

1. H. D. Babcock, Astrophys. J. **130**, 364 (1959).
2. R. Howard, Sol. Phys. **38**, 283 (1974).
3. E. N. Parker, Astrophys. J. **164**, 491 (1971).
4. S. Tomczyk, J. Schou, and M. J. Thompson, Astrophys. J. Lett. **448** (1), L57 (1995).
5. M. J. Thompson, J. Toomre, E. R. Anderson, *et al.*, Science **272** (5266), 1300 (1996).
6. T. Sorbard, G. Berthomieu, P. Morel, *et al.*, Astron. Astrophys. **324**, 298 (1997).
7. E. A. Gavryuseva, V. G. Gavryusev, and M. P. Di Mauro, Pis'ma Astron. Zh. **26** (4), 313 (2000) [Astron. Lett. **26**, 261 (2000)].
8. R. Howe, J. Christensen-Dalsgaard, F. Hill, *et al.*, Science **287**, 2456 (2000).
9. R. Howe, J. Christensen-Dalsgaard, F. Hill, *et al.*, Astrophys. J. Lett. **533**, L163 (2000).
10. E. A. Spiegel and J.-P. Zahn, Astron. Astrophys. **265**, 106 (1992).
11. N. O. Weiss, in *Lecture on Solar and Planetary Dynamos*, Ed. by M. R. E. Proctor and A. D. Gilbert (Cambridge Univ. Press, Cambridge, 1994), p. 59.
12. G. Rüdiger and L. L. Kichatinov, Astron. Astrophys. **269**, 581 (1993).
13. V. N. Krivodubskiĭ, Astron. Zh. **61**, 540 (1984) [Sov. Astron. **28**, 316 (1984)].
14. V. N. Krivodubskiĭ, Astron. Zh. **61**, 354 (1984) [Sov. Astron. **28**, 205 (1984)].
15. S. I. Vaĭnshteĭn, Ya. B. Zel'dovich, and A. A. Ruzmaĭkin, *Turbulent Dynamo in Astrophysics* [in Russian] (Nauka, Moscow, 1980).
16. E. N. Parker, *Cosmical Magnetic Fields: Their Origin and Their Activity* (Clarendon Press, Oxford, 1979; Mir, Moscow, 1982).
17. F. Krause and K. Radler, *Mean Field Magnetohydrodynamics and Dynamo* (Akademie-Verlag, Berlin, 1980; Mir, Moscow, 1984).
18. P. S. McIntosh, in *Solar Activity Observations and Predictions*, Ed. by P. S. McIntosh and M. Dryer (Massachusetts Inst. of Technology, Cambridge, 1972; Mir, Moscow, 1976), p. 43.
19. M. D. Altschuler, D. E. Trotter, G. Newkirk, and R. Howard, Sol. Phys. **39**, 3 (1974).
20. V. I. Makarov and M. V. Kushnir, Soln. Dannye, No. 7, 64 (1987).
21. E. N. Parker, Astrophys. J. **122** (2), 293 (1955).
22. H. Yoshimura, Astrophys. J., Suppl. Ser. **29**, 467 (1975).
23. V. M. Galitsky and D. Sokoloff, Geophys. Astrophys. Fluid Dyn. **91**, 147 (1999).
24. K. M. Kuzanyan and D. Sokoloff, Astron. Astrophys. Trans. **18**, 129 (1999).
25. V. N. Kryvodubskyj, G. Rüdiger, and L. L. Kichatinov, Visn. Kiev. Univ., Ser. Astron., No. 33, 55 (1994).
26. V. N. Krivodubskiĭ, Astron. Zh. **75**, 139 (1998) [Astron. Rep. **42**, 122 (1998)].
27. M. Stix, *The Sun: An Introduction* (Springer-Verlag, Berlin, 1989), p. 200.
28. H. Yoshimura, Sol. Phys. **47**, 581 (1976).
29. L. L. Kichatinov and G. Rüdiger, Astron. Astrophys. **260**, 494 (1992).
30. A. E. Dudorov, V. N. Krivodubskiĭ, T. V. Ruzmaĭkina, and A. A. Ruzmaĭkin, Astron. Zh. **66**, 809 (1989) [Sov. Astron. **33**, 420 (1989)].
31. A. B. Severnyĭ, *Some Problems of Solar Physics* [in Russian] (Nauka, Moscow, 1988).
32. I. W. Roxburg, *Seismology of the Sun and the Distant Stars* (Reidel, Dordrecht, 1986), p. 249.
33. R. Rozner and N. O. Weiss, Nature **317**, 790 (1985).

Translated by A. Getling

Astronomy Reports, Vol. 45, No. 9, 2001, pp. 746–750. Translated from Astronomicheskiĭ Zhurnal, Vol. 78, No. 9, 2001, pp. 859–864.

The Increase in the Magnetic Flux from the Polar Regions of the Sun over the Last 120 Years

V. I. Makarov[1], V. N. Obridko[2], and A. G. Tlatov[1]

[1]*Main Astronomy Observatory, St. Petersburg, Russia*

[2]*Institute of Terrestrial Magnetism, the Ionosphere, and Radio Wave Propagation, Russian Academy of Sciences, Troitsk, Moscow oblast, 142092 Russia*

Received January 9, 2001

Abstract—The latitudes of the zonal boundaries of the global magnetic field of the Sun are determined from the magnetic neutral lines on synoptic Hα maps obtained during 1878–1999. The area of the polar zone occupied by magnetic field of a single polarity at solar minima has doubled over the last 120 years. This provides an explanation for the secular increase in heliospheric characteristics, which differs from the two-fold increase of the magnetic field strength predicted for this period. The temporal variations of the magnetic flux from the polar regions and their role in global changes of the Earth's climate are discussed in connection with secular variations in the structure of the internal magnetic field of the Sun. © *2001 MAIK "Nauka/Interperiodica".*

1. INTRODUCTION

A number of indirect pieces of evidence for the growth in the solar magnetic field with time have recently been published [1]. This is related to both changes of the internal structure of the Sun and to the global warming and growth of the surface temperature of oceans on the Earth [2]. Recently, warming was detected in both meteorological observations and dendrology measurements. As a rule, global warming is associated with human activity. An analysis of measurements of the radial component of the interplanetary magnetic field detected at the Earth's orbit during 1964–1996 was performed in [1]. This analysis shows that the magnetic field in the solar corona has grown by 40 per cent over the last 32 years. The behavior of the ⟨aa⟩ geomagnetic-activity index over the last 100 years suggests that the solar magnetic field has grown by a factor of 2.3 [1].

This conclusion is very important from a theoretical point of view, since it presents fundamental new problems and restrictions for dynamo theory. In addition, it is obvious that this effect could be significant for geophysical phenomena and long-term climatic variations. On the one hand, the magnetic field is the source of every activity on the Sun. On the other hand, there is a correlation between the Wolf number (as an index of local activity) and the total flux of the solar radiation. Consequently, we expect that the flux of solar radiation should change with time. Indeed, the solar radiation changes with a period of about 11 years. However, we are interested here in the long-term trend, namely, the growth of the solar radiation by 0.036 per cent each decade [3].

Note, however, that a direct comparison of the results of [1] and [3] is rather complicated. One usually associates variations in the solar radiation with local fields (numbers of sunspots and flocculi). At the same time, the heliospheric magnetic field is determined by open configurations, which, in turn, are determined by global and large-scale magnetic fields. The contribution of local magnetic fields is rather small. These fields exhibit an 11-year periodicity, while variations in the global magnetic field of the Sun lead those of the local magnetic field by 5–6 yrs [4, 5]. In addition, it is shown in [6, 7] that the global magnetic field, together with the local field, is responsible for variations in the solar radiation to an appreciate extent. The results presented in [1] agree with the previous results of [8], which showed that computations of the magnetic field near the Earth and in the heliosphere based on observations of the photospheric magnetic field are in agreement with direct measurements made by instruments on spacecraft.

The results of [1] and [8] were recently criticized in [9, 10], where it was pointed out that solar observations over the last 32 years do not indicate any "secular" or long-term variations in the magnetic field. Kotov and Kotova [9, 10] attribute the agreement between the computations and measurements of the magnetic field to the application of an artificial correction that depends on the latitude of the measurement point. However, we do not accept all the arguments presented in [9, 10]. For example, the observations of the Sun as a star interpreted in [9, 10] as observations of the total magnetic field of the Sun are not unambiguously related to the interplanetary magnetic field. In fact, the "magnetic field of the Sun as a star" reflects the imbalance between the magnetic fluxes of opposite polarities detected in the visible solar hemisphere. The magnetic fields of various structures contribute to this quantity, with weights proportional to the radiation intensity. The peripheral portions of the visible solar hemisphere make a small contribution. It is particularly important that the polar mag-

netic field, which dominates in the formation of the heliospheric magnetic field, also makes a small contribution. These magnetic fields of various structures contribute to the "magnetic field of the Sun as a star" and the heliospheric magnetic field with different weights, which is of fundamental importance.

Note that some of these remarks are also applicable to the Stanford measurements of the magnetic field used in [8]. It is well known that the solar polar magnetic fields indicated by magnetograph measurements are strongly underestimated. A correction taking into account the latitude dependence of the polar field is not unquestionable and, in part, was introduced precisely to provide agreement with measurements performed near the Earth. Therefore, we cannot consider an agreement between the computations and spacecraft measurements as an independent verification of the relation between them. Note also that the "coronal" magnetic field used in [1], in fact, is the magnetic field at the base of the heliosphere; i.e., at distances of $(2.5–3.5)R_0$ from the center of the Sun. As a rule, the coronal magnetic field is defined as the field at distances considerably smaller than $2.5R_0$.

2. OBSERVATIONAL DATA

We consider here data on the latitude-temporal distribution of unipolar regions of large-scale solar magnetic field accumulated over 120 years (1878–1999). These data were derived from synoptic Hα maps of the distribution of magnetic neutral lines constructed using the technique presented in [11, 12]. Although these data are based only on the polarity of the magnetic field, they provide reliable statistic information on long-term variations of the global field. Studies of magnetic Hα maps have led to detailed analyses of changes in the polarity of the solar magnetic field [13], the discovery of three-fold changes in the polarity of the polar magnetic field [14], the detection of the 55-year cycle of solar activity in torsional vibrations [15], and the conclusion that the large-scale magnetic field of the Sun is primary with regard to the local fields of active regions [5, 16]. The magnetic Hα maps were tested via comparisons with various solar and geophysical data: the number of polar faculae and the divergence of polar magnetic field lines indicated by eclipse data [17], and variations of Galactic cosmic rays [18, 19]. We can estimate the polar activity of the Sun at the photospheric level from the number of polar faculae observed at the Kislovodsk Mountain Station of the Main Astronomical Observatory in 1960–1999 [20]. There is a correlation between the number of polar faculae and the strength of the polar magnetic field [21].

3. VARIATIONS OF THE AREA OF POLAR REGIONS

The axially symmetric component of the solar magnetic field exhibits a zonal structure with a characteristic scale that is determined by either the mean latitude of the magnetic neutral lines or the boundaries of the zonal structure [13, 14]. As a rule, at solar minima, $l = 3$ for $m = 0$, where l and m are numbers of harmonics of the magnetic field expanded in spherical functions. During an activity minimum, the boundaries of the zonal structure are located near latitudes of 40° and 0°, but vary from cycle to cycle. At solar maxima, the magnetic-field structure is described by $l \sim 5–7$ for $m = 0$. During these periods, in addition to two high-latitude boundaries that drift toward the poles, there are two zonal boundaries at latitudes of about 20° in both hemispheres.

As is noted in [1], solar magnetic-field data for the last 100 years were derived from analyses of the geomagnetic index ⟨aa⟩. This planetary magnetospheric index has been determined since 1868 from three-hour measurements of the geomagnetic field at two antipodal stations [22]. The high correlation between ⟨aa⟩ and the velocity of the solar wind near the Earth reflects the fundamental relationship between solar and geomagnetic activities. It is known that the cycle of the geomagnetic index ⟨aa⟩ includes several components [23]. The component related to the poloidal magnetic field (polar coronal holes) is shifted with respect to the sunspot cycle by 5–6 yrs [23]. The heliospheric magnetic field is determined by collections of open magnetic lines associated with the solar polar regions.

We can estimate the secular variations of the heliospheric field by estimating long-term variations in the ratio of the areas occupied by local and global fields. The concept of a boundary separating regions of global (polar) and local magnetic fields was introduced in [24]. This boundary characterizes secular variations in the ratio of the areas occupied by local and global fields in the clearest manner at the minima of 11-year cycles. Table 1 and Fig. 5b of [24] present the locations of high-latitude boundaries of the zonal structure of the magnetic field at solar minima. These boundaries separate the high-latitude unipolar magnetic field of the Sun from the local magnetic fields of active regions of sunspots and faculae. Table 1 and Fig. 5b of [24] show that the high-latitude zonal boundary separating polar and sunspot activities moved toward the equator by on average 15° over the 12 solar cycles from 1878 to 1999 (Fig. 1). The northern zonal boundary shifted from 55° in 1878 to 36° in 1996. A similar phenomenon takes place in the southern hemisphere, where the zonal boundary shifted from 51° in 1878 to 39° in 1996. During this whole time, the behavior of the high-latitude boundary clearly exhibits the magnetic 22-year cycle as a pair of even and odd 11-year cycles. On average, the latitude of this high-latitude boundary is 4° higher in even cycles than in odd cycles. This means that the area of the solar polar zone occupied by magnetic field of a single polarity and, probably, the flux of the dipolar magnetic field change during the 22-year cycle. This behavior is less clearly visible for the low-latitude boundary. Nevertheless, a reversed law can be observed; i.e., a pair of odd and even cycles. Note that the northern hemisphere was more active than the

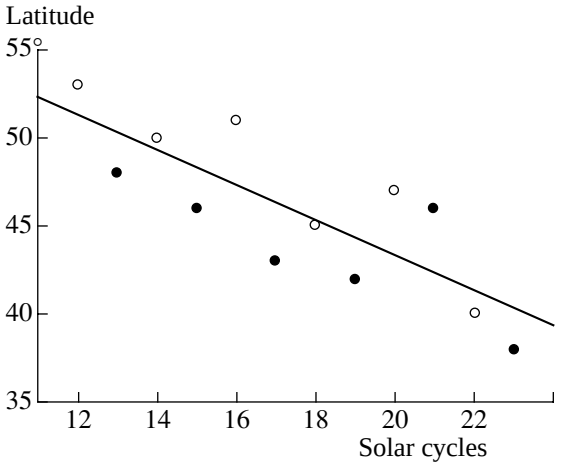

Fig. 1. The latitude of the zonal boundary of the large-scale magnetic field of the Sun at minima of 11-year cycles 12–23 from 1878 to 1996 from magnetic synoptic Hα maps (the filled and empty circles correspond to odd and even cycles).

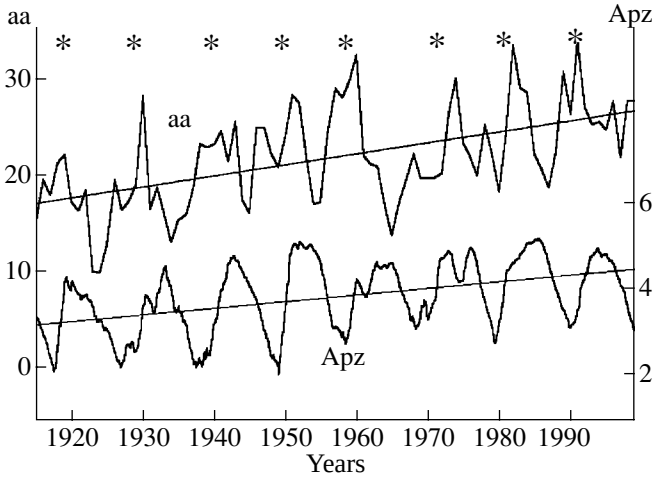

Fig. 2. The annual average geomagnetic index ⟨aa⟩ and area Apz of unipolar magnetic regions of the solar polar caps for latitudes above 40° and corresponding linear approximations. The asterisks mark epochs of polarity reversals of the polar magnetic field derived from Hα maps.

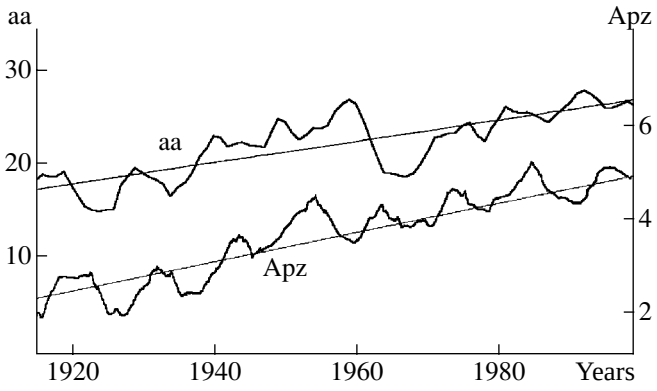

Fig. 3. The index ⟨aa⟩ and area Apz of polar caps smoothed with a window of six years during the period 1915–1999.

southern hemisphere over the last 120 years, since it displayed a shift of the zonal boundary toward the equator of 19°, while the southern shift was only 12°. Nevertheless, the total increase in the area of the solar polar zone occupied by magnetic field of a single polarity at solar minima is clearly observed.

Let us consider variations of the area of the polar zone of single polarity of the solar magnetic field during 1878–1999. A spherical segment with angle $\pi/2 - \varphi$, where φ is the latitude of the high-latitude boundary, occupies a relative area $S = (1 - \sin\varphi)/2$ in units of the total solar surface. Table 1 from [24] shows that, at solar minima, the polar region of magnetic field of a single polarity occupied a relative area of 0.202 in 1878 and 0.392 in 1996; i.e., this area increased by a factor of 1.9. This almost twofold increase in the area of the high-latitude zone of unipolar magnetic field over the last 120 years is in agreement with the increase in the geomagnetic index ⟨aa⟩ during the same period (Fig. 2). Therefore, we attribute the doubling of the solar magnetic field obtained in [1] to an increase in the magnetic flux from the polar regions of the Sun, associated with an increase in the area occupied by field of a single polarity. Obviously, this polar magnetic flux is determined by polar coronal holes and is directly related to the geomagnetic activity expressed by ⟨aa⟩. This result is connected with the problem of long-term changes in the internal structure of the Sun, which, in turn, is related to global variations of solar activity and the Earth's climate. The Maunder minimum of solar activity and corresponding "little ice age" on the Earth is a clear example of climatic changes due to the global changes in solar activity.

Let us introduce as an index of variations of the global magnetic field the area of the solar polar cap (with latitudes higher than 40°) occupied by magnetic field of a single polarity. We denote this area Apz. Figure 2 compares the temporal variations of ⟨aa⟩ and Apz in 1915–1999; it is clear that variations in ⟨aa⟩ and Apz are virtually identical. The asterisks in Fig. 2 mark epochs of polarity reversals for the polar magnetic field during this period (according to [20]). We can see an abrupt increase in ⟨aa⟩ immediately after polarity reversals. This is clearly associated with the formation of polar coronal holes, which enhance the solar wind and, accordingly, the geomagnetic index ⟨aa⟩. Figure 3 shows ⟨aa⟩ and Apz smoothed over six years. We can see that the behavior of the two indices is virtually the same over these 85 years.

We can obtain another estimate of this effect by calculating the sum of the magnetic moments of the solar dipole and octupole fields [5] using the coefficients of the expansion of the magnetic field into spherical functions for Hα maps for 1915–1999 [17]:

$$h_{10} = \mu\sin\varphi, \quad g_{11} = \mu\cos\varphi\cos\lambda,$$

$$h_{11} = \mu\cos\varphi\sin\lambda,$$

where μ is the dipole magnetic moment, φ and λ are the latitude and longitude of the north pole of the dipole in

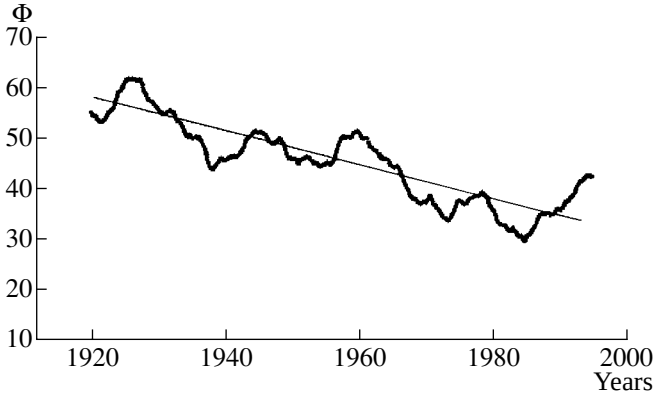

Fig. 4. The latitude of the solar magnetic dipole "equator."

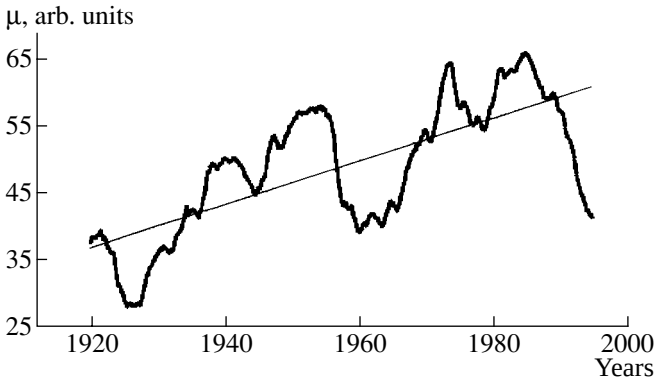

Fig. 5. The magnetic dipole moment of the Sun.

a Carrington coordinate frame, and g_{10}, g_{11}, and h_{11} are the expansion coefficients presented in [17]. Note that these coefficients do not include a polar correction. We can determine the dipole magnetic moment and the latitude of its "equator" $\Phi = 90° - \varphi$ using these relations for each Carrington rotation. We then smoothed these quantities with a ten-year window. Figure 4 presents the position of the solar dipole equator Φ. We can see a gradual trend of Φ to move toward lower latitudes. This means that the average (over 10 years) position of the solar dipole equator and the similar tilt of the heliospheric current sheet decrease with time. Figure 5 shows the magnetic dipole moment μ of the Sun. We can see that there is a clear trend, which can be interpreted as a growth in the magnetic dipole field. However, we should remember that our calculations use only neutral lines of the magnetic field derived from Hα maps. This means that the increase in μ actually describes the growth of the polar-cap area discussed above.

Therefore, this suggests that the area of the polar region occupied by magnetic field of a single polarity at solar minima has nearly doubled over the period 1878–1996. This is directly related to the conclusion drawn in [1] based on an analysis of the geomagnetic index ⟨aa⟩ that the magnetic field increased by a factor of two over the past 100 years [1]. Here, we show that the increase in ⟨aa⟩ is more likely due to an increase in the area of the solar polar cap and the corresponding increase in the magnetic flux from the Sun, which had been interpreted as an increase in the magnetic field strength. However, our result does not resolve the problem of global secular variations of the solar magnetic field, but only turns it in another direction. The nature of secular variations of the zonal structure of the solar magnetic field remains unclear.

4. POLAR MAGNETIC FIELD OF THE SUN

High-latitude and polar activity of the Sun is not displayed only by coronal holes. Polar faculae in white light accompanied by kilogauss magnetic fields, bright X-ray points, and transient active regions represent a special class of solar activity at latitudes above 40°. We have a uniform series of measurements of the number of polar faculae performed in Kislovodsk since 1964 and the dependence of the polar magnetic field on the number of polar faculae [21]. We can use these data to estimate changes in the polar magnetic field of the Sun from 1964 to the present and compare these with observations.

We will consider the 20th to 23rd cycles of solar polar activity (1965–1999) separately. According to [1], the total magnetic flux from the Sun has increased by a factor of 1.4 since 1964. Since a substantial fraction of the flux is associated with the solar polar region, we can use the available data on the area of the polar cap and the mean number of polar faculae per cycle [21]. Using these data, we can easily show that the area of the polar cap occupied by magnetic field of a single polarity (at solar minima) has increased by a factor of 1.5 over this period. This provides evidence that changes in the magnetic flux from the Sun are mainly associated with changes in the high-latitude region occupied by field of a single polarity.

According to [1], the annual average amplitude of the radial component of the interplanetary magnetic field near the Earth has increased by a factor 1.4 since 1964. It is well known that the mean number of polar faculae per cycle increased by a factor of three from 1965 to 1996. There is a relation between the number of polar faculae (NPF) observed at Kislovodsk and the polar magnetic field (in Gauss) measured at Kitt Peak. According to [21], we obtain

$$B\ (G) \sim 3/40\ NPF + 1.0.$$

Using the published data, we can easily see that the mean magnetic field of the Sun has increased by a factor of 1.5: from 2 G in 1965 to 3 G in 1996. Taking into account our estimates and the correlations presented in [1], we find that the solar polar magnetic field did, indeed, increase, but over a shorter time interval of about two–three 11-year cycles. Since the Mount Wilson polar-faculae observations do not indicate any

long-term increase in the number of polar faculae over 80 years [25], this suggests that the polar magnetic field did not change. Thus, we conclude that the long-term increase in the magnetic flux from the Sun and in the index ⟨aa⟩ is associated with a growth in the area of the solar polar cap during this period.

ACKNOWLEDGMENTS

This work was supported by the Russian Foundation for Basic Research (project codes 99-02-16200, 99-02-18346, and 00-02-16355), INTAS (07-1088), and NRA (98-OSS-08).

REFERENCES

1. M. Lokwood, R. Stamper, and M. N. Wild, Science **399**, 43 (1999).
2. E. V. Cliver, V. Boriakoff, and J. Feynman, Geophys. Res. Lett. **25**, 1035 (1998).
3. R. C. Willson, Science **277**, 1963 (1997).
4. V. I. Makarov and A. G. Tlatov, Astron. Zh. **77**, 1 (2000) [Astron. Rep. **44**, 759 (2000)].
5. V. I. Makarov, V. N. Obridko, A. G. Tlatov, and B. D. Shelting, Sol. Phys. (in press).
6. A. A. Anan'ev and V. N. Obridko, Astron. Zh. **76**, 942 (1999) [Astron. Rep. **43**, 831 (1999)].
7. E. V. Ivanov, V. N. Obridko, and A. A. Ananev, Sol. Phys. (in press).
8. Y.-M. Wang and N. R. Sheeley, Jr., Astrophys. J. Lett. **447**, L143 (1995).
9. V. A. Kotov and I. V. Kotova, private communication (2000).
10. V. A. Kotov and I. V. Kotova, Pis'ma Astron. Zh. **27**, 302 (2001) [Astron. Lett. **27**, 260 (2001)].
11. V. I. Makarov and M. P. Fat'yanov, Pis'ma Astron. Zh. **8**, 631 (1982) [Sov. Astron. Lett. **8**, 340 (1982)].
12. V. I. Makarov, Soln. Dannye, No. 6, 59 (1984).
13. V. I. Makarov and K. R. Sivaraman, Sol. Phys. **85**, 227 (1983).
14. V. I. Makarov and K. R. Sivaraman, Sol. Phys. **119**, 35 (1989).
15. V. I. Makarov and A. G. Tlatov, Astron. Zh. **74**, 474 (1997) [Astron. Rep. **41**, 416 (1997)].
16. V. I. Makarov and A. G. Tlatov, in *Proceedings of the 9th European Meeting on Solar Physics, 1999*, Ed. by A. Wilson, p. 125.
17. V. N. Obridko and B. D. Shelting, Sol. Phys. **184**, 187 (1999).
18. A. V. Belov, R. T. Gushchina, V. N. Obridko, *et al.*, Izv. Akad. Nauk, Ser. Fiz. (in press).
19. A. V. Belov, B. D. Shelting, R. T. Gushchina, *et al.*, submitted to J. Atmos. Sol.-Terr. Phys. (in press).
20. V. I. Makarov and V. V. Makarova, Sol. Phys. **163**, 267 (1996).
21. V. I. Makarov and V. V. Makarova, Astron. Soc. Pac. Conf. Ser. **140**, 347 (1998).
22. P. D. Mayaud, J. Geophys. Res. **72**, 6870 (1972).
23. P. S. Simon and J.-P. Legrand, Ann. Geophys. (France) **7**, 579 (1989).
24. V. I. Makarov, Sol. Phys. **150**, 359 (1994).
25. N. R. Sheeley, Jr., Astrophys. J. **374**, 386 (1991).

Translated by V. Badin